12-14-2001

A Transport Study of Sodium Phosphate Dodecahydrate Pipeline Plugging Mechanisms

Vijay Kumar Raju

A TRANSPORT STUDY OF SODIUM PHOSPHATE DODECAHYDRATE

PIPELINE PLUGGING MECHANISMS

By

Vijay Kumar Raju

A Thesis
Submitted to the Faculty of
Mississippi State University
in Partial Fulfillment of the Requirements
for the Degree of Master of Science
in Chemical Engineering
in the Dave C. Swalm School of Chemical Engineering

Mississippi State, Mississippi

December 2001

A TRANSPORT STUDY OF SODIUM PHOSPHATE DODECAHYDRATE

PIPELINE PLUGGING MECHANISMS

By

Vijay Kumar Raju

Approved:

Jeff S. Lindner Research Professor, DIAL (Director of Thesis)	Rebecca K. Toghiani Associate Professor and Graduate Coordinator of the Dave C. Swalm School of Chemical Engineering (Major Professor and Committee Member)
Priscilla J. Hill Assistant Professor of the Dave C. Swalm School of Chemical Engineering (Committee Member)	A.Wayne Bennett Dean of the College of Engineering

Name: Vijay Kumar Raju

Date of Degree: December 14, 2001

Institution: Mississippi State University

Major Field: Chemical Engineering

Director of Thesis: Dr. Jeff S. Lindner

Major Professor: Dr. Rebecca K. Toghiani

Title of Study: A TRANSPORT STUDY OF SODIUM PHOSPHATE DODECAHYDRATE PIPELINE PLUGGING MECHANISMS

Pages in Study: 116

Candidate for Degree of Master of Science

The thesis investigates pipeline plugging mechanisms that have occurred during interim stabilization transfers at Hanford. A laboratory-scale saltwell pumping test loop was designed to evaluate a surrogate of Hanford Tank 241-SX-104 supernate. The effect of surrogate flow rate, cooling water flow rate and phosphate concentrations on plugging mechanisms was investigated. Critical parameters like particle and agglomerate size, velocity and bed growth rate were determined. Theoretical models were used to compare the experimental pressure rise and temperature drop of the surrogate in the channel. An operating region in which a plug would not form was developed, based on the experimental results. Experiments are also reported on plug remediation. Unplugging experiments at varying pump pressure heads and residence time of plug in the line were performed.

DEDICATION

I would like to dedicate the work to my family and friends.

ACKNOWLEDGEMENTS

I would like to express my sincere appreciation to several individuals, without whom my thesis would not have been such a valuable experience. First and foremost I would like to thank the director of my thesis, Dr. Jeff Lindner, for his guidance, support and the long hours he spent on the thesis. I would like to offer special thanks to my major advisor and committee member, Dr. Rebecca Toghiani, for helping in my academic development and support throughout the thesis. I would also like to thank my committee member, Dr. Priscilla Hill, for her valuable suggestions. Furthermore, I would like to thank Dr. Hossein Toghiani and Dr. Hani Al Habbash for helpful discussions during the course of the work. In addition, I would like to thank Dr. Ping Ray Jang, Mr. John Andol and other DIAL shop personnel for their resources and help. I would also like to thank Sam Nicholson and Tushar Durve for their help and patience during the course of the work. Finally, I would like to acknowledge the support and love of my colleagues and friends at DIAL and MSU for making my graduate experience memorable.

TABLE OF CONTENTS

APPENDIX Page

LIST OF TABLES

TABLE Page

LIST OF FIGURES

FIGURE Page

FIGURE Page

LIST OF SYMBOLS

A_p	Particle area in the direction of motion
A_h	Heat exchanger cross sectional area
A	Pipe cross sectional area
a'	Internal pipe radii
b	Ratio of external to internal pipe radii
C_D	Drag coefficient
C_{pw}	Specific heat of cooling water
C_{ps}	Specific heat of surrogate
C	Product of Prandtl and Eckert number
D_{sh}	Shell inside diameter
D_p	Mean particle diameter
D_{exo}	Pipe outside diameter
D, D_{ex}	Pipe diameter
d	Particle diameter
E	Eckert number
Fr	Froude number
F_{dk}	Drag force between the phases in layer k
f_{yk}	Wall friction factor
f_{yi}	Layer friction factor

f	Coefficient of friction
g	Acceleration due to gravity
h_w	Water heat transfer coefficient
h_s	Surrogate heat transfer coefficient
h	Height of bed in the layer
K_c	Ratio of conductivities
$K^{'}$	Friction loss due to pipe fittings
K	Conductivity
k_d	Ratio of thermal diffusivities
k	Thermal Diffusivity
L_{tl}	Length of the test loop
L_p	Characteristic length of particle
L_{hex}	Length of heat exchanger
L	Pipeline length
m_w	Mass flow rate of water
m_s	Mass flow rate of surrogate
m_p	Particle mass
Nu_w	Nusselt number of water
Nu_w	Nusselt number of surrogate
P_k	Gas phase pressure in layer k
Pr	Prandtl number
P	Pressure in the test loop
ΔP	Pressure drop in the line

Q_{ex},Q	Flow rate
Re_w	Reynolds number of cooling water
Re	Reynolds number of surrogate
r_{yk}	Volume of phase y in layer k
r	Dimensionless radial distance
S_{my}	Mass transfer between layers of phase y
S_i	Cross sectional perimeter
T_{wo}	Outlet temperature of cooling water
T_{wi}	Inlet temperature of cooling water
T_{so}	Outlet temperature of surrogate
T_{si}	Inlet temperature of surrogate
ΔT_{lm}	Log-mean temperature difference
ΔT	Temperature drop
t	Time
U_{yk}	Velocity of the corresponding phase in the layer
U	Overall heat transfer coefficient
V_C	Critical velocity
V, V_{ex}	Axial velocity of the stream
x	Length in direction of flow
Z	Datum level
β	Angle of inclination of the pipe axis above horizontal
μ	Dynamic viscosity
ρ_{gk}	Density of gas phase in layer k

ρ_{sk}	Density of solid phase in layer k
ρ_p	Particle density
ρ	Fluid density
τ'	Dimensionless time
τ	Shear stress between phases
θ	Dimensionless temperature

CHAPTER I

INTRODUCTION

1.1. Background

The Hanford site, located in the state of Washington, contains one of the largest volumes (53 Mgal) of radioactive waste in the world [1]. High-level radioactive waste was generated starting in 1944 as part of the U.S. defense program. Fuel discharged from the nuclear reactors was processed to obtain uranium and plutonium and the resulting radioactive process waste was stored in 149 single shell tanks (SST) built between 1944 and 1964 [2].

The single shell tanks were made of carbon steel and were installed inside steel reinforced concrete enclosures. The tanks were buried in the earth to minimize radiation effects. After 1964, the waste was stored in double shell tanks (DST), each of which had a secondary steel shell and a better leak detection system. To minimize the construction of more waste storage tanks and better utilization of the existing tanks, the liquid waste was concentrated by evaporation until crystallization occurred [3]. The concentrated liquid waste was directed to DSTs while the precipitated salts were stored in SSTs.

The waste resulting from the enrichment of nuclear fuel was mostly acidic. Sodium hydroxide was added to the acidic waste to neutralize it and reduce corrosion. Thus, the tank wastes are alkaline in nature, with pH values of greater than or equal to 12. The waste is composed of inorganic compounds like sodium hydroxide, sodium nitrate

and sodium carbonate; radioactive species and their fission products; and chelating agents like EDTA and oxalate. The waste stored in the SSTs is comprised of sludge, saltcake and liquid waste. Sludge contains solids resulting from the neutralization of acid waste before being transferred to SSTs. Saltcake is made up of various salts that resulted from the evaporation of liquid waste. The liquid waste in the tanks is present either as pumpable liquid (supernate) or interstitial liquid [4]. After the liquid waste in a tank is removed, saltcake is retrieved from the tank to empty and finally close the tank. Water is added to the tank to dissolve the saltcake and the resulting saltwell liquor is pumped out of the tank.

Many of the SSTs have exceeded their design life times and gradual corrosion of the steel tank surface has occurred. Waste leakage from 67 of the single shell tanks is either assumed or confirmed. It is estimated that approximately 1Mgal of waste has leaked [1]. To reduce the risk of tank leakage, an "interim stabilization" or "saltwell pumping" process was developed [5]. A central screen well and a jet pump are installed in the tank. The supernate and interstitial liquid present in the saltcake and sludge collects in the central well due to seepage. The liquid level in the central well is maintained at a minimum volume to increase the rate of seepage from the adjacent layers of saltcake and sludge. This is attained by constant operation of a jet pump, which pumps the liquid waste that collects in the central well directly to transfer lines for routing to an existing DST. It is estimated that a gallon of saltcake contains 1/2 – 1/3 gallon of pumpable liquid while a gallon of sludge contains 1/10 – 1/4 gallon of pumpable liquid. Dilution water can be added to the screen well to prevent solid particles from "blinding" the screen. The pumping is stopped when the dilution water rate exceeds the inflow of liquid into the

well. The rate of seepage and thus, the total time to remove the liquid waste in the tanks, depends on waste properties like porosity, viscosity and surface tension.

The liquid waste from the SSTs is transferred to the DSTs through a complex network of carbon steel pipes interconnected using jumpers. The carbon steel pipes are heat-traced and buried underground, while the jumpers are not heat-traced. Problems have been encountered during interim stabilization activities. The transfer of supernate from Hanford tank 241-SX-104, without the addition of dilution water to the central well, resulted in a pipeline plug [1]. Later operations performed with the addition of dilution water also resulted in a plug. The plug was believed to have occurred in a jumper. Herting identified that the main constituent of the plug was sodium phosphate dodecahydrate ($Na_3PO_4 \cdot 0.25H_2O \cdot 12H_2O$) needles using PLM [6]. Tank samples were found to form a gel at a $Na_3PO_4 \cdot 0.25H_2O \cdot 12H_2O$ concentration of 0.044M and temperature of 23^oC [7].

Unit operations carried out on tank 241-U-103 also resulted in a plug in an unheated jumper section [1]. This blockage caused a six-week delay in operations. Costs associated with such plugs vary due to the specific circumstances including the position of plug, the nature of the plug, etc.; however, a rough estimate for the U-103 plug was an approximate cost impact of $800K. This accounted for increased operations and maintenance costs (opening valve pits, checking and removing jumpers, etc.) and an associated loss of production [8].

1.2 Literature Review

1.2.1 Trisodium Phosphate Dodecahydrate ($Na_3PO_4 \cdot 0.25H_2O \cdot 12H_2O$)

Trisodium phosphate is industrially manufactured by the addition of sodium hydroxide to disodium phosphate obtained from the reaction of phosphoric acid and soda ash [9]. The resulting solution is then dried to obtain trisodium phosphate crystals. The existence of sodium phosphate with different waters of hydration as $Na_3PO_4 \cdot 12H_2O$, $Na_3PO_4 \cdot 10H_2O$, $Na_3PO_4 \cdot 8H_2O$, $Na_3PO_4 \cdot 7H_2O$, $Na_3PO_4 \cdot 6H_2O$ and $Na_3PO_4 \cdot 0.5H_2O$ has been reported [10]. Recent Raman studies showed that $Na_3PO_4 \cdot 12H_2O$ loses water of hydration when heated from 30^oC to 200^oC and results in $Na_3PO_4 \cdot 0.5H_2O$ [11]. The transition from $Na_3PO_4 \cdot 12H_2O$ to $Na_3PO_4 \cdot 6H_2O$ was noted to occur below 84^oC, while the subsequent transition to $Na_3PO_4 \cdot 0.5H_2O$ could not be identified. The studies also indicated the possible existence of a new sodium phosphate hydrate, $Na_3PO_4 \cdot 4H_2O$, during dehydration, which had not been identified previously [11].

Stoichiometry studies of $Na_3PO_4 \cdot 12H_2O$ indicated the presence of excess sodium hydroxide in the compound [12,13]. Tillmans and Baur established the crystal structure of sodium phosphate dodecahydrate using X-ray diffraction [14].

The hydrogen molecules (tetrahedrons) are bounded by phosphate molecules (gray triangles) from different layers. The 12 water molecules contained in each layer are connected by hydrogen bonds. The top view of the crystal structure (not shown) indicates large voids between the water molecules, which are the only available positions for the NaOH molecules. The amount of NaOH present between the water molecules varies between 0 to 0.25, depending on the conditions under which the crystal formed. Sodium phosphate dodecahydrate is used in denture cleaner formulations, emulsifying salts and in

pH control for foods and detergent products [9]. Widespread use of sodium phosphate dodecahydrate in heat transfer media applications has also been reported [15,16].

1.2.2 Solid-Liquid two phase flow

Interim stabilization involves the transfer of supernate, which is initially a liquid. When a temperature drop occurs during transfers, solids start to form. This results in a transition of liquid flow to solid-liquid two-phase flow. Two-phase flow is commonly encountered in industrial applications and includes gas-solid, liquid-liquid, solid-liquid and gas-liquid flows. An example of solid-liquid flow is the transport of coal as a coal-water slurry. Much interest has been shown in this area of transport due to its relative low infrastructure cost and effective mode of transportation. In spite of this, the state of the knowledge is such that a full understanding of the basic phenomena is limited by the complexity of two-phase flow problems, and most of the definitions in practice today are governed by empirical observations.

Solid-liquid two-phase flow can be broadly classified into homogeneous flow, heterogeneous flow, moving bed flow and stationary bed flow [17]. While homogeneous flow involves flow in a single phase, heterogeneous flow contains solid particles dispersed in liquid. Moving bed flow is a heterogeneous flow with solids forming a bed and moving at the bottom of the pipe. In a stationary bed flow, the bed formed at the bottom of the pipe is stationary while there is heterogeneous flow above the bed. As the height of the bed increases more depositions occur, ultimately resulting in a plug. The deposition of solid particles from a heterogeneous stream, is termed settling and can be divided into discrete, flocculant, hindered and compression types [18]. Discrete settling

occurs when the concentration of solid particles in the heterogeneous flow is limited and there is no interaction between the particles. Hindered settling occurs when the concentration of solids in the stream is high and the motion of a particle is limited by the surrounding particles. Flocculant and compression settling occur in environments with very high solid loading environments.

The terminal settling velocity of a particle in heterogeneous flow is an important quantity for characterizing the settling behavior of the particle. The diameter of a particle, a key property for characterizing particle deposition, is dependent upon the settling velocity (critical velocity). A particle will reach its settling velocity when the sum of the drag force and buoyancy force are equal to the gravitational force on the particle. Several equations are available in the literature for the calculation of the settling velocity. Based on the concept of drag force the settling velocity over a wide range of Reynolds numbers is obtained [19].

$$V_c = \left[2 \cdot g \cdot m_p \cdot \frac{\left(\rho_p - \rho\right)}{\rho \cdot \rho_p \cdot A_p \cdot C_D} \right]^{0.5} \qquad (1\text{-}1)$$

where, g is the acceleration due to gravity, m_p is the particle mass, A_p is the projected particle area in the direction of motion, ρ_p is the particle density, ρ is the fluid density and C_D is the drag coefficient. The settling velocity at low Reynolds numbers can also be calculated from the Stokes' law [20].

$$V_c = \frac{g \cdot \left(\rho_p - \rho\right) \cdot d^2}{18 \cdot \mu} \qquad (1\text{-}2)$$

where, μ is the dynamic viscosity of the fluid. The particle Reynolds number (Re_p<1) for Stokes' law to be applied. Another expression for settling velocity for irregular shaped particles at low Reynolds numbers was proposed by Durand [21].

$$V_C = Fr \cdot \left[2 \cdot g \cdot D \cdot \frac{(\rho_p - \rho)}{\rho} \right]^{0.5} \qquad (1-3)$$

where Fr is the froude number obtained from charts or using $Fr=V^2/2gL_p$, D is pipe diameter, V is the axial velocity of the stream and L_p is the characteristic length of particle (generally taken as the dimension perpendicular to direction of motion). An expression for the settling velocity of particles in slurry transport, involving flocculation, compression and hindered settling, was obtained by Oroskar and Turian [22].

$$\frac{V_C}{\sqrt{g \cdot d \cdot (S-1)}} = a_0 \cdot C_v^{a_1} \cdot (1 - C_v)^{a_2} \cdot \left(\frac{D}{d} \right)^{a_3} \cdot \left[\frac{D \cdot \rho_l \cdot \sqrt{g \cdot d \cdot (S-1)}}{\mu} \right]^{a_4} \cdot x^{a_5} \quad (1\text{-}4)$$

where V_c is critical velocity, d is particle diameter, D is pipe diameter, C_v is solids concentration, ρ_l is stream density, S is specific gravity and constants a_i are determined by regression analysis of experimental data points. The settling velocity and the corresponding critical particle size obtained from these calculations enable the determination of flow patterns and characteristics.

1.2.3 Pressure drop correlations for two-phase flows

Pressure drop information is a critical component in the design of efficient heterogeneous fluid transport pipelines. The pressure drop is generally higher in a solid-

liquid two-phase system due to elevated frictional losses. Early correlations were developed by Lockhart and Martinelli for a gas-liquid two phase flow [23]. They developed a parameter, X, called the Lockhart-Martinelli parameter, which was the square root of the ratio of the pressure drop in a pipe for liquid flow to that of a gas in a pipeline. The parameter could be used to calculate the total pressure drop in the pipeline for a two-phase flow. Mao et al. later developed a correlation for three-phase flow of nuclear waste containing water, hydrogen and ammonia gases and gibbsite ($Al_2O_3 \cdot 3H_2O$) solid by adapting the Lockhart-Martinelli equation [24]. The three-phase system was treated as a two-phase system by considering the flow to be composed of gas (air) and liquid (water and gibbsite mixture).

Wilson considered suspended and contact loads to develop equations for solid-liquid pipeline flow [25]. A suspended load was a flow of particles in a liquid, while a contact load was particles sedimenting and forming a moving bed with a heterogeneous flow above. Transitional cases could be defined by a combination of the two loads. The total pressure drop in the channel was accounted for by summing the individual pressure gradients due to the two loads. Doron developed a simple model for solid-liquid flow in horizontal pipes by considering a three-layer flow [26]. The bottom layer was a stationary bed, with a moving bed layer above and finally a heterogeneous layer on the top. The model could be simplified for use with a two-layer flow (heterogeneous flow on top and moving bed at the bottom). Models developed by Wilson and Doron do not account for mass transfer between the layers comprising the flow. This implied that the bed height in each of the cases was constant and did not increase with time.

Mason and Levy later extended the model of Wilson and Doron by accounting for the mass transfer between the layers and developed a correlation for pressure profiles of a non-suspension gas-solids flow of fine powders [27]. The flow was assumed to consist of two layers: a dense gas-solid layer at the bottom, with high solids concentration and a dilute gas-solid layer on the top, with low solids concentration. Since the most important parameter in two-phase flow is the bed height, all the equations involving mass and momentum were expressed in terms of bed height. The pressure profiles were obtained by applying the conservation of mass and momentum equations to the gas and solid phases in each layer. The mass balance equations for gas and solid phases in each layer are given by:

$$\frac{d}{dx}\left(r_{g1} \cdot \rho_{g1} \cdot U_{g1} \cdot A_1 \right) = S_{mg} \tag{1-5}$$

$$\frac{d}{dx}\left(r_{s1} \cdot \rho_{s1} \cdot U_{s1} \cdot A_1 \right) = S_{ms} \tag{1-6}$$

where S_{my} is the mass transfer between layers of phase y, U_{yk} is the velocity of the corresponding phase in the layer, x is the length in direction of flow, ρ_{yk} is density of gas phase in layer k and ρ_s is density of solid phase in layer k. The momentum balance equations for gas and solid phases in each layer are given by:

$$\frac{d}{dx}\left(\rho_{g1} \cdot r_{g1} \cdot A_1 \cdot U_{g1}^2 \right) = S_{mg} \cdot U_{g1} - \tau_{g1} \cdot r_{g1} \cdot S_1 - r_{g1} \cdot A_1 \cdot \frac{dP_1}{dx} - \rho_{g1} \cdot r_{g1} \cdot A_{1g} \cdot \sin(\beta) - F_{d1} \tag{1-7}$$

$$\frac{d}{dx}\left(\rho_{s1} \cdot r_{s1} \cdot A_1 \cdot U_{s1}^2 \right) = S_{ms} \cdot U_{s1} - \tau_{s1} \cdot r_{s1} \cdot S_1 - r_{s1} \cdot A_1 \cdot \frac{dP_1}{dx} - \rho_s \cdot r_{s1} \cdot A_{1g} \cdot \sin(\beta) + F_{d1} + \left(r_{g2} \cdot \tau_{gsi} + r_{s2} \cdot \tau_{ssi} \right) \cdot r_{s1} \cdot S_i \tag{1-8}$$

where F_{dk} is the drag force between the phases in layer k, P_k is the gas phase pressure in layer k, β is the angle of inclination of the pipe axis above horizontal, τ is the shear stress between phases, S_i is cross sectional perimeter and r_{yk} is volume of phase y in layer k.

Mass transfer from each phase is calculated using:

$$S_{mg} = \frac{1}{2}\left(r_{g1} \cdot \rho_{g1} \cdot U_{g1} \cdot S_i \cdot \frac{dh}{dx} \right) \tag{1-9}$$

$$S_{ms} = \frac{1}{2}\left(r_{s1} \cdot \rho_{s1} \cdot U_{s1} \cdot S_i \cdot \frac{dh}{dx} \right) \tag{1-10}$$

where h is the height of bed in the layer. The shear stresses in the layers are calculated using:

$$\tau_{gsi} = \frac{1}{2} f_{gi} \cdot \rho_{g2} \cdot \left(U_{g2} - U_{s1} \right) \left| U_{g2} - U_{s1} \right| \tag{1-11}$$

$$\tau_{ssi} = \frac{1}{2} f_{si} \cdot \rho_{s} \cdot \left(U_{s2} - U_{s1} \right) \left| U_{s2} - U_{s1} \right| \tag{1-12}$$

$$\tau_{s1} = \frac{1}{2} f_{s1} \cdot \rho_{s} \cdot U_{s1}^2 \tag{1-13}$$

$$\tau_{g1} = \frac{1}{2} f_{g1} \cdot \rho_{g1} \cdot U_{g1}^2 \tag{1-14}$$

where f_{yk} is the wall friction factor and f_{yi} is the layer friction factor. The drag forces are obtained from:

$$F_{d1} = \frac{3 \cdot r_{s1} \cdot A_1}{4 \cdot D_p} C_{d1} \cdot \rho_{g1} \cdot \left(U_{g1} - U_{s1} \right) \cdot \left| U_{g1} - U_{s1} \right| \tag{1-15}$$

where C_{d1} is the drag coefficient and D_p is the mean particle diameter. Similar equations were developed for the temperature profiles in the two layers by the application of the conservation of energy. The resulting ordinary differential equations were solved to obtain the temperature and pressure profiles. Mason and Levy noted that this formalism can be used with two-phase solid-liquid flows.

1.2.4 Unsteady state heat transfer correlations for forced convection

Heat transfer models are important in the design of heat transfer equipment including heat exchangers, nuclear reactors and heat-traced pipelines. Though many models are available for steady state heat transfer in the literature, information and models available for unsteady state heat transfer are limited. Unsteady state heat transfer models give a better understanding of temperature changes taking place during flow immediately after cooling or heating is applied externally. A numerical solution for forced convection in a channel was developed by Seigel [28]. The model was developed by neglecting the temperature variation within the wall. The heat transfer equations for the fluid were combined with those for the wall and the resulting equations were solved by integrating along characteristic grid lines using the finite difference method.

Tan and Spinner developed solutions for transient heat transfer in a shell and tube heat exchanger [29]. The model used a quasi-steady state approach by assuming a finite wall heat capacity and a finite shell-side heat transfer resistance. Analytical solutions were obtained for step changes in shell-side and tube-side fluids of the exchanger by using Laplace transforms. The model primarily depends on the ratio of heat capacities of fluid and wall and is thus susceptible to appreciable error at high values of the ratio and

changes in velocity. Sucec obtained an analytical solution for the problem of unsteady state convective heat transfer in a fluid flowing in a pipe, when the temperature of the outside medium is suddenly changed [30]. The analytical solution obtained using Laplace transforms provided surface heat flux and fluid and wall temperatures. Wall conduction was not considered. Successive models developed by Schutte et al. [31] and Yan et al. [32] dealt with the problem of transient heat transfer by considering wall conduction. Schutte et al. solved the problem using the Simplest algorithm and Hybrid scheme defined by Patankar [33], while Yan et al. solved the problem by writing the system of equations in the form of a tridiagonal matrix, which was solved using the Thomas algorithm [33]. The models established the effect of thermal conductivity ratio, thermal diffusivity ratio, wall thickness ratio, Peclet number and wall conduction on convective heat transfer.

Krishan developed a simple model for unsteady heat transfer during fully developed flow in a pipe [34]. The model pertained to the transient change in the temperature profiles of the fluid in the pipe with a change in either heat flux or temperature at the outer surface. The conservation of energy equation was applied to both the wall and the fluid and combined by matching boundary equations. The equations were then reduced to the form of the Bessel equation and solved using Laplace transforms. The model was valid only for small time periods after the external heat flux was applied because of the presence of higher order terms in the expansion of Laplace transforms. The dimensionless energy equations used were:

$$\text{Liquid}: \qquad \frac{\partial \theta_1}{\partial \tau} = \frac{\partial^2_2 \theta_1}{dr^2} + \frac{1}{r}\frac{\partial \theta_1}{\partial r} + C \cdot r^2, \qquad 0 \le r \le 1 \qquad (1\text{-}16)$$

Solid : $$\frac{\partial \theta_2}{\partial \tau} = k \cdot \left(\frac{\partial_2^2 \theta_2}{dr^2} + \frac{1}{r} \frac{\partial \theta_2}{\partial r} \right), \qquad 1 \le r \le b \qquad (1\text{-}17)$$

where θ_1 and θ_2 denote the dimensionless temperatures, k_2,k_1 are thermal diffusivites , K_2, K_1 are conductivities of wall and fluid respectively, $\theta = (T-T_0)/T_0$, τ' is the dimensionless time = $k_1 t/a'^2$, t is time, a' is the internal pipe radii, b is the ratio of external to internal pipe radii, C = 16·Pr·E, E(Eckert number) = $V^2/c_p\Delta T$, Pr is the Prandtl number, K_c is the ratio of the thermal conductivities, K_2/K_1, k_d is the ratio of the thermal diffusivities, k_2/k_1 and r is the dimensionless radial distance, r'/a'. The initial and boundary conditions were given by:

$$\theta_1 = \theta_2 = 0 \quad \text{for } \tau \le 0, 0 \le r \le b \qquad (1\text{-}18a)$$

$$\theta_1 = \theta_2 \quad \text{for } \tau > 0, r = 1 \qquad (1\text{-}18b)$$

$$\frac{\partial \theta_1}{dr} = K_c \frac{\partial \theta_2}{dr} \quad \text{for } \tau > 0, r = 1 \qquad (1\text{-}18c)$$

$$\frac{\partial \theta_2}{\partial r} = S_1 \text{ (const)} \quad \text{for } \tau > 0, r = b \quad \text{(for constant outer heat flux)} \qquad (1\text{-}18d)$$

$$\theta_2 = S_2 \text{ (const)} \quad \text{for } \tau > 0, r = b \quad \text{(for constant outer temperature)} \qquad (1\text{-}18e)$$

The detailed solutions for temperature and pressure profiles of wall and fluid are presented in the original work of Krishan [34]. The resulting model was shown to result in good correlations for unsteady state heat transfer in a pipe. Sample calculations for the pressure rise and temperature drop models are given in Appendix D.

1.3 Motivation for the work

The risk of pipeline plugging exists for many transfers, so the development of sound technical recommendations on plugging mechanisms and operating envelopes for pipeline transfers could result in significant savings. The primary goal of this thesis is to develop a thorough understanding of plug formation mechanism(s) pertinent to interim stabilization transfers at Hanford. This includes identification of parameters such as the critical particle size as well as particle, agglomerate and bed growth rates. Conditions causing plug formation including surrogate flow rate, the rate at which a surrogate is cooled and variations in specific component concentration have been investigated. This information, in turn is expected to lead to the development of an operating envelope that can be used by site operators to prevent plugs. The secondary focus of the work deals with the unplugging of the pipeline once a plug has formed. A test loop for the study of solid-liquid two-phase flows was built to mimic the actual Hanford saltwell pumping system (Chapter 1.1). The test loop was equipped with thermocouple probes and pressure transducers to obtain temperature profiles of the supernate in the pipeline during flow and to monitor the increase in pressure in the event of a plug. An additional goal of the thesis includes comparison of experimental results to theoretical models.

A surrogate was developed based on $Na_3PO_4 \cdot 0.25H_2O \cdot 12H_2O$, as it was identified as the primary constituent of the pipeline plugs at Hanford. Based on the discussion in Chapter 1.2.1, the surrogate containing $Na_3PO_4 \cdot 0.25H_2O \cdot 12H_2O$ would be a liquid above 50^oC (the tank temperature of supernate in 241-SX-104) and solids were expected to form on cooling. The surrogate would flow purely as a liquid at or above a temperature of 50^oC. At lower temperatures, crystallization of the sodium phosphate

dodecahydrate would begin and then the principles of two-phase flow discussed in Chapter 1.2.2 would be applicable. The transformation of homogeneous flow to a plug proceeds according to the following sequence: homogeneous flow, heterogeneous flow, moving bed flow, stationary bed flow and. Increases in the rate of particle formation and particle concentrations characterize the transformation from homogeneous flow to a plug. The important parameter in two-phase flow, critical velocity, was calculated from the experimental data obtained during the test loop experiments.

The two-phase flow anticipated during saltwell test loop experiments resulted in a pressure drop in the channel. This is due to the higher frictional losses expected during two-phase flows. The pressure drop in the channel was modeled by using the pressure drop correlations discussed previously (Chapter 1.2.3). The temperature of the surrogate would generally decrease if it were cooled, though the temperature profiles would depend on the cooling rate. The models discussed in Chapter 1.2.4 can be used to predict the temperature profiles of the surrogate. Thus, with this research, an experimental test loop was developed which provides insight into the pipeline plugging process and the factors that affect the process. Furthermore, the experiments performed define operating regimes over which a plug would not form.

Chapter 2 of the thesis describes the surrogate development and scoping tests. The design and construction of the test loop along with the test loop experiments are discussed here. The equipment used for the experiments including those for imaging, instrumentation and analysis. The results of the pipeline plugging experiments at various flow rates of surrogate, cooling rates of water and concentrations of surrogate are described in Chapter 3. The critical parameters of two-phase flow, obtained from image

analysis, are given. The results from the unplugging experiments are also discussed. An initial operating envelope is presented. The conclusion of the research and description of goals achieved is given in Chapter 4. The future scope for the research is discussed.

CHAPTER II

SX-104 SURROGATE DEVELOPMENT AND EXPERIMENTAL SECTION

2.1 Introduction

The pipeline plugs that occurred during transfers from tanks 241-SX-104 and 241-U-103 at Hanford were attributed to the formation of $Na_3PO_4 \cdot 0.25H_2O \cdot 12H_2O$ crystals [35]. In view of this, a plug simulant was developed which predominantly contained $Na_3PO_4 \cdot 0.25H_2O \cdot 12H_2O$, some $NaNO_3$ and gelled at a temperature between 30^oC and 35^oC.

2.2 SX-104 Surrogate Development and Scoping Tests

2.2.1 Description of Software and Analysis Instrumentation Used

Potential surrogates for the supernate from SX-104 were modeled using ESP (Environmental Simulation Program) and compared to the experimental results. ESP is a simulation software package developed by OLI Sytems, that allows simulation of chemical processes. ESP Process, a unit within the ESP software, was mainly used to perform simulations on the potential surrogates. ESP Process can be divided into 4 sections: Chemistry Model, Process Build, Process Analysis and Summary. Chemistry Model contains different molecular species for which simulations can be performed.

Based on the species selected in the chemistry model, the software retrieves information corresponding to the different combinations of species possible, chemical reactions and thermodynamic data. Process Build contains various unit operations like mixing, heat exchange, absorption, etc. The unit operations and operating conditions at which simulations are to be performed were selected here. Process Analysis combines information from the Chemistry Model and Process Build sections and performs the simulations for the corresponding chemical system, unit operations and conditions. Process Summary directs the output from Process Analysis to various output devices as disk, printer etc.

ESP simulations were initially performed on a recipe developed by R.Hunt at Oak Ridge National Laboratory (ORNL) [36]. This formulation was evaluated and is described later in this chapter. The molecular species in the recipe were selected in the Chemistry Model, which then generated detailed speciation, reactions and thermodynamic data corresponding to the chemical system. The unit operations and conditions for which simulations were to be performed were selected in Process Build. Typically, a mixer was used to simulate the mixing of the recipe adiabiatically at 50^{o}C. The output stream from the mixer was sent to a heat exchanger. The output stream from the heat exchanger was set to different temperatures (25^{o}C-45^{o}C). Process Analysis was then used to couple the data from the Chemistry Model and Process Build and the simulations were directed to an excel file.

II. *Polarizing Light Microscope (PLM):* An Olympus model BX50 PLM was used to analyze samples from the saltwell experiments. Different objective lenses (10X, 20X, 40X) were used with an eyepiece of magnification 10. This provided final images with a

total magnification of 100X, 200X and 400X. The PLM was fitted with an Olympus color camera, model OLY-750. The camera was connected to a computer through a frame grabbing board. ImagePro software from Media Cybernatics was used to analyze the test samples and also to perform image analysis on the images from the DIAL/MSU imaging system.

III. *IC(Ion Chromatograph):* A Dionex 500 series IC (Figure 2.1) was used to perform quantitative analysis on diluted samples (Appendix A). The anions determined using the IC were $(PO_4)^{3-}$ and NO_3^-. The IC consisted of an eluent generator, a gradient pump, an electrochemical detector, a detector in suppressed mode, a guard column and a separator column. The eluent used for the mobile phase chromatography was KOH. Ion Chromatography is based upon ion exchange to accomplish separation of analyte ions, followed by chemical suppression of eluent conductivity and conductivity detection. A liquid sample was introduced at the top of the separator column. The ionic eluent (KOH) pumped through the column caused differential migration of the sample ions down the column as a result of the size and affinity of the ions to the active sites of the column. The column effluent with the anions was then passed through a suppressor system if higher sensitivity was required. The purpose of the suppressor system column, containing a strongly acidic cation exchange resin in hydrogen form, was to chemically reduce the background conductivity of the eluent before entering the conductivity cell, so that the anions could be easily detected. In the conductivity cell, the analyte ions were separated into discrete bands that were detected using a conductivity detector. The detector was connected to a computer with Dionex software. The instrument output was a plot of conductivity versus time (a chromatogram). Each ion appeared as a peak in the

chromatogram. Identification and quantification was performed by comparing the retention times (time from injection to peak maximum) and peak heights to the standards of the sample both of which are proportional to the concentration of the analyte over a particular range. Samples were prepared for IC analysis as described in Appendix A.

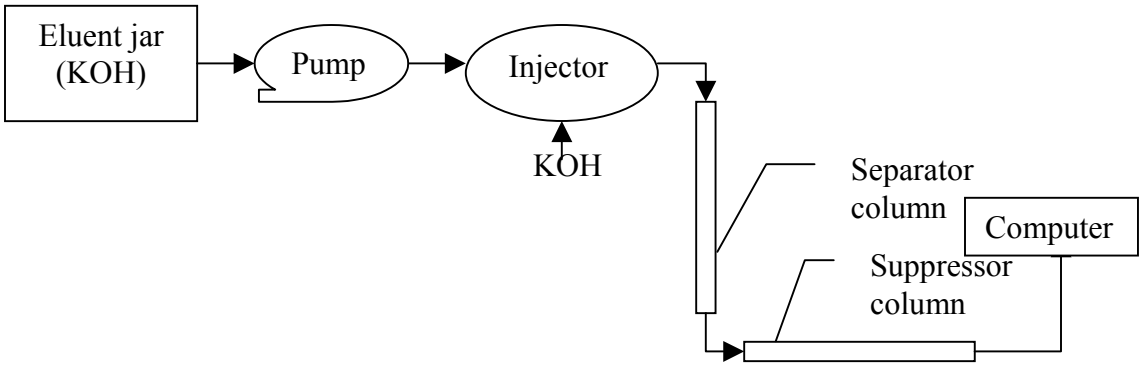

Figure 2.1: Basic components of an ion chromatograph.

IV. *DIAL/MSU imaging system:* The imaging system (Figure 2.2) was used to record the events leading to plug formation in the saltwell test loop [37]. The imaging system contained a camera with a resolution of 640 X 480 pixels and a lens with a focal length of 75mm. The total magnification provided by the camera was doubled to 150mm by the use of an extender lens. The camera was connected to a computer preloaded with IMAQ frame grabbing hardware. The frame grabbing software developed by DIAL was used with the camera. The camera was capable of collecting 12.5 frames/sec.

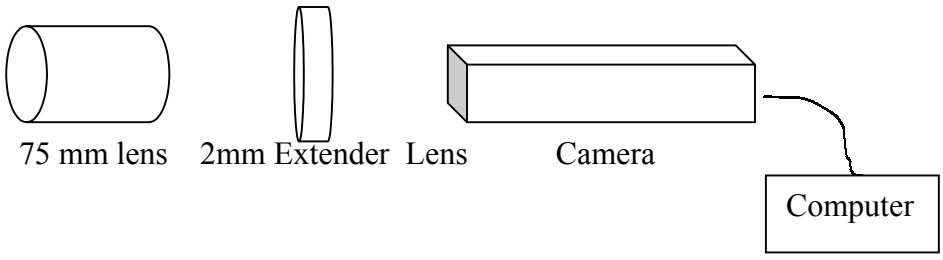

Figure 2.2: Block diagram of the DIAL/MSU imaging system.

2.2.2 Surrogate scoping tests

The initial recipe provided by R.Hunt at ORNL was modified to obtain the required levels of phosphate in the plug. The following table describes surrogate development leading to the final saltwell test loop recipe.

Table 2.1: Recipes used in the development of plug simulant for saltwell test loop.

	Concentration of species in M				
Recipe	$NaNO_3$	NaOH	$Na_3PO_4 \cdot 0.25H_2O \cdot 12H_2O$	$NaAlO_2$	Na_2CO_3
Rodney 2	7	2	0.2	1	0.4
Recipe 5b	7	2	0.3	1	0.4
Recipe 6	7	2	0.4	1	--
Recipe 7	7	2	0.3	1	--
Recipe 8	7	2	0.3	1	0.1

The recipe was prepared by determining the experimental quantity required (as set by the experimental needs) of recipe and adding the corresponding volume of distilled water to a beaker. The beaker was then heated to a temperature of 55^{o}-60^{o}C on a hot plate. The temperature of the solution was monitored using a thermometer or a thermocouple. The amount of NaOH corresponding to the final concentration was weighed and added to the beaker containing the distilled water. The contents were then stirred thoroughly using a magnetic stirrer. After the NaOH dissolved completely, $NaNO_3$ was added while stirring. The remaining constituents of the surrogate: $Na_3PO_4 \cdot 0.25H_2O \cdot 12H_2O$, $NaAlO_2$ and Na_2CO_3; were then added in order and stirred until all of the solids dissolved. The clear surrogate was then allowed to cool to 50^{o}C. Initial details of surrogate behavior are discussed below.

The recipe provided by ORNL was made up at 55^{o}C and cooled down to room temperature but the solution did not form a gel even though a lot of solids were observed. ESP simulations (Table 2.2) were done on a total mole basis. ESP predicted that, at room

temperature 39.24 gm of $NaNO_3$ and 53.11 gm of $Na_3PO_4 \cdot 0.25H_2O \cdot 12H_2O$ would be present (Figure 2.3). The solids were observed under the PLM and it was seen that the sample contained a large number of diamond shaped crystals of $NaNO_3$ and some rod shaped crystals of $Na_3PO_4 \cdot 0.25H_2O \cdot 12H_2O$ (Figure 2.4). In light of the large amount of $NaNO_3$ in the solid phase, it was decided to alter the recipe such that the primary solid constituent was $Na_3PO_4 \cdot 0.25H_2O \cdot 12H_2O$.

Table 2.2: ESP simulations for recipe Rodney2.

Temp (^oC)	25	30	35	40	45	50
Liquids:						
H_2O (gm)	977.78	988.34	1003	1007.21	1007.21	1007.2
Total wt (gm)	1763.97	1831.74	1865.31	1877.36	1877.36	1877.36
Volume in (L)	1.27	1.31	1.35	1.36	1.37	1.38
Enthalpy (cal)	-5.10E+06	-5.25E+06	-5.36E+06	-5.40E+06	-5.39E+06	-5.39E+06
Density (gm/L)	1387.80	1392.70	1386.40	1378.90	1374.20	1364.00
pH	15.02	14.84	14.63	14.45	14.34	14.12
EC (mho/cm)	0.18	0.19	0.24	0.27	0.29	0.33
Abs Visc (cP)	4.94	4.48	4.02	3.57	3.32	2.85
Ionic Strength	11.10	11.78	12.05	12.13	12.14	12.15
Solids:						
Weight (gm)	113.39	45.62	12.04	0	0	0
Volume (L)	0.026	0.005	0.002	0	0	0
Enthalpy (cal)	-3.18E+05	-1.63E+05	-43755.3	0	0	0
Density (gm/L)	1926.37	1768.38	1845.65	0	0	0
Total solution:						
Weight (gm)	1764.00	1877.36	1877.35	1877.36	1877.36	1877.36
Volume (L)	1.30	1.32	1.35	1.36	1.37	1.38
Solids wt%	6.04	2.43	0.64	0	0	0
Water wt%	55.43	52.65	53.43	53.65	53.65	53.65
Density(gm/L)	1398.60	1394.05	1387.02	1378.83	1374.20	1364.00

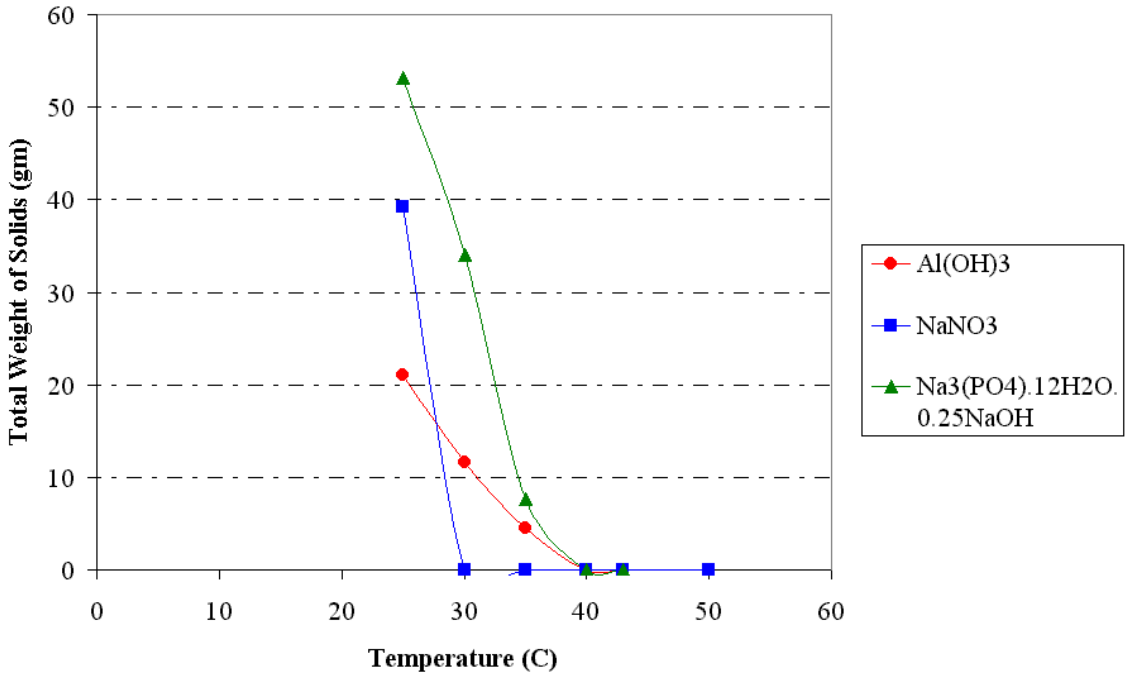

Figure 2.3: ESP prediction for amount of solids present in Rodney2 as a function of temperature.

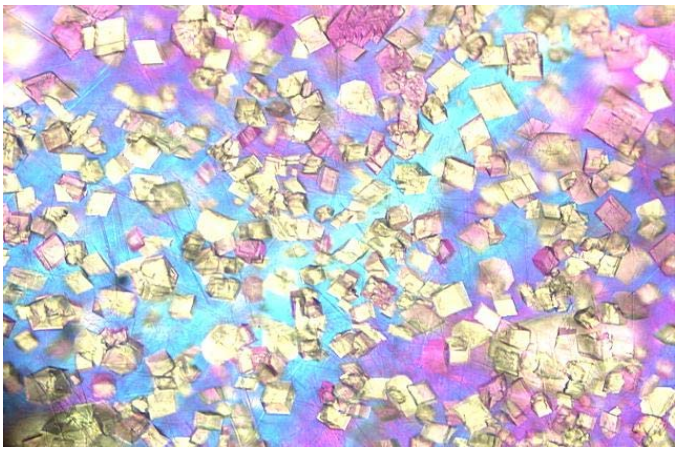

Figure 2.4: PLM image of recipe Rodney#2 at 25C using 20X objective

The recipe was further modified by reducing the carbonate concentration to 0.1M. This was based on the observation from other recipe attempts that illustrated that the amount of carbonate in the actual recipe had a direct effect on the amount of nitrate in the

gel. The solution was prepared at 60°C and allowed to cool down. The phosphates started to form in solution at 38°C and the solution gelled at 34°C, within the gel containing some nitrates. The ESP simulations (Table 2.3) for recipe 8 showed that the solid phase would contain 53.93 gms of $Na_3PO_4 \cdot 0.25H_2O \cdot 12H_2O$ and 0 gms of $NaNO_3$ at 34°C (Figure 2.5). The gel was observed under the PLM (Figure 2.6) and it was seen that the gel contained a large number of long rod-like $Na_3PO_4 \cdot 0.25H_2O \cdot 12H_2O$ and some diamond shaped $NaNO_3$ crystals. Based on the gelling temperature and the gel chemistry, it was decided to use recipe 8 as the plug simulant in the saltwell pumping test loop.

Table 2.3: ESP simulations for Recipe8.

Temp (°C)	25	30	35	40	43	50
Liquid:						
H20 (gm)	977.71	987.81	1002.20	1023.72	1028.71	1028.70
Total wt (gm)	1742.48	1796.21	1829.18	1875.79	1884.98	1884.98
Volume (L)	1.27	1.31	1.33	1.37	1.38	1.39
Enthalpy (cal)	-5.03E+06	-5.15E+06	-5.26E+06	-5.42E+06	-5.44E+06	-5.44E+06
Density (gm/L)	1374.40	1376.90	1371.60	1368.20	1364.7	1355.40
pH	15.00	14.82	14.61	14.41	14.31	14.08
EC, 1/ohm-cm	0.19	0.22	0.25	0.29	0.31	0.36
Abs Visc, cP	4.36	3.95	3.57	3.31	3.11	2.68
Ionic Strength	10.48	11.00	11.27	11.64	11.73	11.74
Solids:						
Weight (gm)	142.50	88.77	55.80	9.19	0	0
Volume (L)	0.022	0.006	0.003	0	0	0
Enthalpy (cal)	-4.45E+05	-3.13E+05	-1.96E+05	-31718.8	0	0
Density (gm/L)	1815.83	1715.48	1700.12	1630.65	0	0
Total solution:						
Weight (gm)	1742.50	1884.98	1884.98	1884.98	1884.98	1884.98
Volume (L)	1.29	1.31	1.34	1.37	1.38	1.39
Solids wt%	7.56	4.71	2.96	0.49	0	0
Water wt%	56.11	52.40	53.17	54.31	54.57	54.57
Density (gm/L)	1381.79	1378.48	1372.40	1368.21	1364.70	1355.40

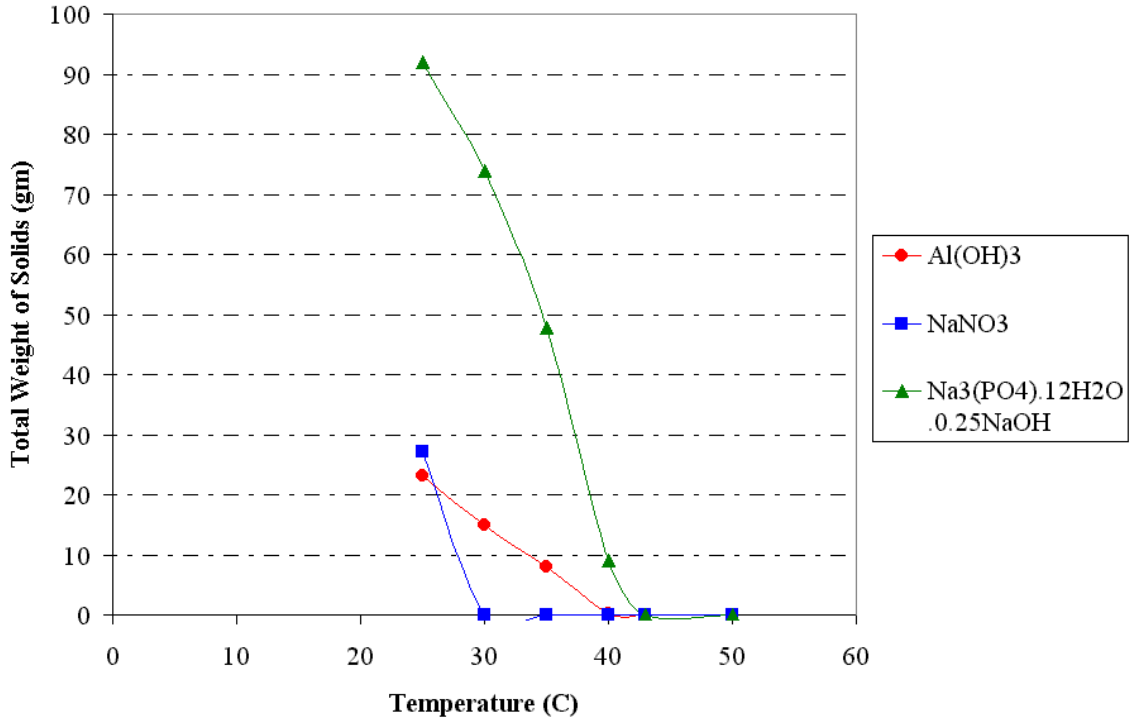

Figure 2.5: ESP prediction for amount of solids in Recipe 8 as a function of temperature.

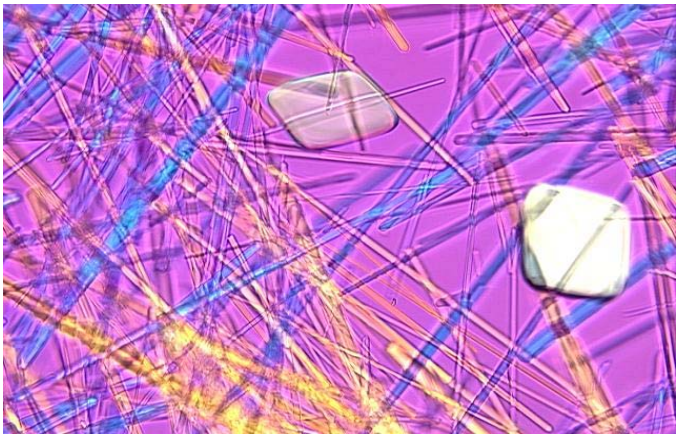

Figure 2.6: PLM image of Recipe 8 at 35^{o}C using 20X objective.

2.3. Design and construction of test loop

2.3.1 Flow characterization

The DIAL/MSU saltwell test loop was designed to obtain data on saltwell pumping, plug formation in the pipeline and other critical information during supernate

transfers at the Hanford facility. The test loop was designed using the Reynolds number, Re, from the Hanford facility as the critical parameter. This choice of parameter was made so that the flow characteristics at Hanford were represented in the test loop. The saltwell pumping information (Table 2.4) for the transfer of SX-104 supernate at Hanford are listed below [38]:

Table 2.4: Pumping information for the SX-104 supernate transfer at Hanford.

Parameter	**Value**
Pipe line Length (L)	varied (200-4000 ft)
Pipe Diameter (D)	varied (0.75-3 in)
L/D ratio	varied (3200-16000)
Pipeline cross sectional area (A)	varied (0.442-7.069 in^2)
Flow rate (Q)	varied (0.5-1.25 gal/min)
Flow velocity(V)	varied (0.908-0.023 ft/sec)
Density (ρ) [a]	1424 kg/m^3
Viscosity (μ) [b]	4.164 cp

a[Ref 38], b from ESP

The Reynolds number for the supernate transfer is given by:

$$Re = \frac{\rho \cdot V \cdot D}{\mu}, \qquad (2\text{-}1)$$

Using the above parameters:

$$180<Re<1800$$

The L/D ratio in the Hanford transfer line was larger than that possible in the laboratory, so the test loop was resized by reducing the diameter of the pipe while keeping the Reynolds number constant. For the saltwell test loop calculations, the density, viscosity and heat capacity were obtained from ESP (Table 2.3). Surrogate properties including density (1390 kg/m^3), viscosity (4 cP) and heat capacity (3020 J/kgK) were taken as constants in the calculations. The thermal conductivity of the surrogate was taken as that

of water. The water properties were taken as functions of temperature [39]. The Prandtl number, Pr, was calculated using:

$$\Pr = \frac{C_p \cdot \mu}{k} \qquad (2\text{-}2)$$

where C_P is the specific heat, μ is the viscosity and k is the thermal conductivity of the fluid. The pipe diameter (D_{ex}) of the saltwell test loop was set at ¼" ID. Based on this the required flow rate was calculated using the Reynolds number from the saltwell pumping operation at Hanford. The flow velocity (V_{ex}) was obtained as 8.2 cm/sec from equation 2-1. This corresponded to a flow rate (Q_{ex}) of 2.45 gal/hr.

2.3.2 Heat transfer

Heat transfer calculations were performed to determine the length of heat exchanger necessary to obtain the required cooling rate. The calculations were done for a single shell and tube, counter flow, heat exchanger. It was noticed during the scoping experiments that the surrogate gelled at a temperature of 38°C in a beaker agitated with a magnetic stirrer and at 35°C without stirring. Assuming a 4°C loss in the temperature of the surrogate between the tank and heat exchanger, the following calculations were performed. The inlet (T_{si}) and outlet (T_{so}) temperatures of the surrogate were fixed at 46°C and 38°C, respectively. The inlet temperature of the cooling water (T_{wi}) was fixed at 26°C and the outlet temperature, T_{wo} , was determined from:

$$q = m_S \cdot C_{ps} \cdot (T_{si} - T_{so}) = Q_{ex} \cdot \rho_S \cdot C_{ps} \cdot (T_{si} - T_{so}) = m_w \cdot C_{pw} \cdot (T_{wi} - T_{wo}) \qquad (2\text{-}3)$$

where m_w and C_{pw} are the mass flow rate and specific heat of cooling water, respectively.

The tube of the heat exchanger channel had an outer diameter (D_{exo}) of 0.5 in. Thus the shell of the exchanger was set at 1" to provide for efficient cooling and contact surface with the tube. The cooling water flow rate required to achieve the desired flow rate was calculated. The cooling water will exhibit good heat transfer characteristics if the flow is in the turbulent regime. This requires a Reynolds number (Re_w) greater than 2300 [40]. The required flow rate was then obtained by estimating a value and iterating to obtain the actual rate. The shell inside diameter (D_{sh}) was taken as 0.96 in. The Reynolds number for flow in annulus is defined as:

$$\mathrm{Re}(m_w) = \frac{4 \cdot m_w}{\pi \cdot (D_{exo} + D_{sh}) \cdot \mu_w(T_{wi})} \qquad (2-4)$$

where m_w is the mass flow rate of cooling water. Using the above function and an initial estimate for m_w of 0.1 kg/sec, the required cooling rate was obtained as 4.6 kg/min. The corresponding volumetric flow rate was then determined as $Q_w = m_w \rho_w(T_{wi}) = 0.2$ gal/min. Using the cooling water mass flow rate (m_w), the cooling water outlet temperature is calculated from equation (2-3) as:

$$T_{wo} = \frac{q}{m_w \cdot C_{pw}(T_{wi})} + T_{wi} \qquad (2-5)$$

An outlet temperature of 27.1^{o}C was obtained.

Using the logarithmic mean temperature difference (LMTD) method for counter flow heat exchangers, the necessary length of heat exchanger corresponding to the surrogate temperature drop was determined [41]. The total energy lost by the surrogate using the LMTD method is given by:

$$q = U \cdot A_h \cdot \Delta T_{lm} \tag{2-6}$$

where U is the overall heat transfer coefficient, A_h is the heat exchanger cross sectional area=$\pi D_{inside} L_{hex}$ and L_{hex} is the length of heat exchanger.

$$\Delta T_{lm} = \frac{(T_{so} - T_{wi}) - (T_{si} - T_{wo})}{\ln\left[\frac{T_{so} - T_{wi}}{T_{si} - T_{wo}}\right]} = 15.46^{o} C \tag{2-7}$$

Rearranging equation (2-6),

$$UA = \frac{q}{\Delta T_{lm}} = 5.59 \frac{W}{K}$$

The Nusselt number and friction factor for cooling water flowing in the shell with the range $0.5<Pr<2000$ and $2300<Re<5\cdot10^6$ are given by [42]:

$$f = (0.79 \cdot ln(Re_W) - 1.64)^{-2} \tag{2-8}$$

$$Nu_W = \frac{\left(\frac{f}{8}\right) \cdot (Re_W - 1000) \cdot Pr_W(T_{hi})}{1 + 12.7 \cdot \left(\frac{f}{8}\right)^{\frac{1}{2}} \cdot \left(Pr_W(T_{hi})^{\frac{2}{3}} - 1 \right)} \tag{2-9}$$

In this case since Re_w=2300:

Nu_w=14.58,

f=0.05

The cooling side heat transfer coefficient was obtained by:

$$h_W = \frac{Nu_W \cdot k_W(T_{hi})}{D_{sh}} \tag{2-10}$$

using the values of the Nusselt number from above, h_w=368.86 W/m^{2}K. The Nusselt number for fully developed laminar flow, uniform heat flux and Pr>0.6 was obtained from the literature as Nu_s=4.36 [43]. The heat transfer coefficient on the tube side was determined from the corresponding equation (2-10) as h_s=422.25 W/m^{2}K. The overall heat transfer coefficient is given by:

$$U = \frac{1}{\left(\frac{1}{h_S}\right)\cdot\frac{D_{exo}}{D_{ex}} + \left(\frac{1}{h_w}\right) + D_{exo}\cdot\frac{ln\left(\frac{D_{exo}}{D_{ex}}\right)}{2\cdot k}} \qquad (2\text{-}11)$$

where, k is thermal conductivity of steel, 15 W/mK. Using h_s and h_w in (2-11), the overall heat transfer coefficient was determined as 129.18 W/m^{2}K. The necessary length of heat exchanger was determined as 22.3 in.

2.3.3 Saltwell Test Loop Components and Instrumentation

The channel diameter for the saltwell test loop (Figure 2.7) was obtained from the calculations above by using the Reynolds number as the critical parameter. The calculated surrogate volumetric flow rate was used in selecting the size of the holding tank, pump and rotameter. Based on the total pump head, the pressure transducers were chosen. The rotameters for control of cooling water flow rate were selected based on the heat transfer calculations. The thermocouple probes to monitor temperature and immersion heaters were also selected based on the heat transfer calculations. Three holding tanks, two for the surrogate and one for water were used. The holding tanks were rectangular tanks with covers. The surrogate that was to be held in the holding tanks was highly basic with a pH value greater than 13-13.5. Initially, polypropylene holding tanks

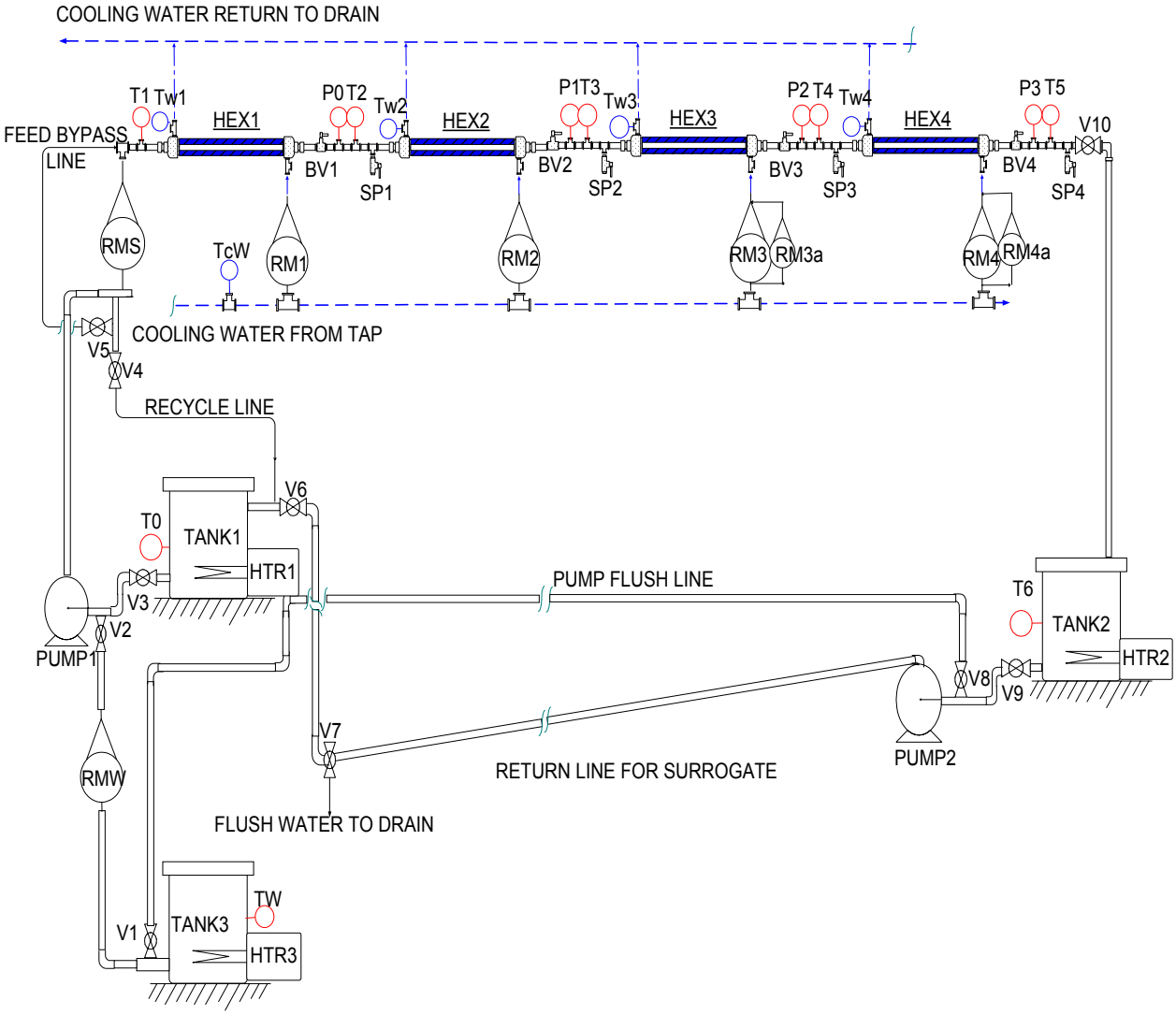

Figure 2.7: Image of saltwell pumping test loop. The designations are as follows: P, pressure transducer, T, thermocouple, RM, rotameter, HTR, immersion heater, Hex, heat exchanger, V, valve, BV, ball valve.

(corrosion resistant) were used; however, there was the possibility of a fire hazard with the immersion heaters. Therefore, stainless steel tanks were employed in later experiments. The stainless steel tanks were made from 10 gauge 316 SS plates. The tank dimensions were 12”(length), 12”(breadth) and 14”(height) providing a maximum volume of 7gal. The thickness of the stainless steel tank walls was 0.135 in. The surrogate holding tank (Tank1) was used to hold the surrogate used in the test loop. The surrogate return tank (Tank2) was used to hold the surrogate that was pumped from

Tank1 through the test loop. Both tanks were fitted with screw immersion heaters to maintain the surrogate temperature around 50^{o}C. The surrogate from Tank2 was constantly recycled to Tank1 to operate the saltwell test loop continuously. The third holding tank (Tank3) was incorporated to allow dilution of the surrogate stream or the future injection of agents for dissolution of a formed plug. Water from Tank3 was also used for preheating the line and regular cleanup of the saltwell test loop to ensure that the line was clear after each run.

Two magentic drive pumps with a rating of 1/15 hp were used in the saltwell pumping test loop. The primary pump (Pump1) was used to pump surrogate from the surrogate holding tank (Tank1) into the saltwell test loop. The return pump (Pump2) was used to pump surrogate from the return tank (Tank2) back to the main surrogate holding tank (Tank1). The pumps were capable of pumping surrogate at flow rates greater than 15 gallons per hour through the test loop. The total pressure at the pump head was 9.2 psig. Three screw plug immersion heaters were used in the saltwell test loop. The immersion heaters were used to maintain temperatures in Tank 1, 2 and 3 around 50^{o}C. The immersion heater screwed into a pipe-threaded opening in the tank wall. Immersion heaters with sheaths made of type 304 stainless steel were used. The heaters corresponding to the above Tanks were named H1, H2 and H3. The power rating on the heaters was 1000W at a supply voltage of 120V. The heaters had an integrated thermostat, which enabled the temperature to be set between 60^{o}F and 250^{o}F. The heating cycle was akin to a sinusoidal wave, so the tank temperature varied from 48-52^{o}C when the set point temperature was 50^{o}C.

Based on the calculations described in section 2.3.2, the shell and tube heat exchangers had a ½" SS 316 sch 80 inner tube while the outer shell was a 1" CPVC sch 80 pipe. The length of the exchanger was 22 in. The heat exchanger was designed such that it would be operated in a countercurrent fashion. Each heat exchanger shell had an inlet for cold/hot water and an outlet for drain water. The test loop was initially designed to have 4 heat exchangers (Hex1, Hex2, Hex3 and Hex4) but was later modified to consist of only 2 heat exchangers (Hex1 and Hex2) followed by a ¼" ID clear Acrylic pipe for plug formation observation purposes. Though the test loop required just one heat exchanger to lower the temperature of the surrogate to 38^{o}C, the other exchanger was also included in view of future experiments.

The saltwell pumping test loop contained different rotameters. One rotameter had a range of 0.8-20 gph and was fitted with a valve, which could be used to adjust the flow rate. The rotameter for use with surrogate (RMS) contained glass and kynar fittings, which offered good corrosion resistance. Acrylic rotameters were used for water. The rotameter (RMW) near Tank2 was used to determine the amount of flush water supplied to unplug the pipeline. The rotameter had a range of 0-12 gph and used a valve to adjust the flow rate at the required level. The acrylic rotameters were also used to provide the required cooling water flow rate on the shell side of the heat exchanger as determined by the heat transfer calculations. Initially the heat exchangers (Hex1, Hex2, Hex3 and Hex4) had rotameters (RM1, RM2, RM3, RM4 respectively) with a range of 0-5 gpm. Later, in order to obtain better heat transfer control in the heat exchangers, (Hex3 and Hex4) rotameters (RM3a, RM4a) with range of 0-1 gpm were used in parallel with the above rotameters. Though the heat transfer calculations determined a cooling rate of 0.2 gpm,

rotameters with higher capacities were chosen. A list of equipment and instrumentation used in the saltwell test loop facility are given in Appendix B, Table B-1.

Various fittings were used in the saltwell test loop to connect the components discussed above. SS 304/316 fittings were used for those in contact with the surrogate while brass fittings were used for those in contact with water. The fittings included valves, bushing reducers, enlargers, couplings, unions, adapters, plugs, tees, nipples, elbows and caps.

Process instrumentation consisted of chemically resistant pressure transducers and thermocouple probes. The pressure transducers were used in the test loop to monitor the pressure increase in the line due to plug formation. Transducers with a voltage output were employed. Initially four pressure transducers were used with the heat exchangers (Hex1, Hex2, Hex3 and Hex4). Later when the clear plastic section was used, pressure transducer P0 was located between Hex1, Hex2 and P1 was located downstream at the end of the clear acrylic pipe. P0 had a range 0-60 psig while P1 had a range of 0-15 psig. The transducers had stainless steel pressure ports for wide media compatibility and had voltage output of 1-5 volts.

The test loop contained two different kinds of thermocouple probes. PFA (Perfluoro Alcoxy) coated thermocouple probes were used with the surrogate. The probes were rated to 400^{o}F and had grounded junctions. The probe diameter was 1/16” and the thermocouple alloy was Iron-Constantan. Initially, 7 PFA coated thermocouple probes were used in the saltwell test loop. The location of thermocouples are given in Figure 2.7. Iron-Constantan thermocouples were used for monitoring heat exchangers and had a sheath diameter of 1/16”.

A Camile Data Acquisition and control system and associated Camile TG software were used to monitor the saltwell test loop experiments. The data acquisition system was used to monitor the temperatures and pressures associated with the flow loop experiments. The voltage output from the transducer was converted into pressure units in the data acquisition system. The transducers were calibrated using a Druck pressure calibrator model DPI6002P0. The calibrator was set at the minimum and maximum of the range for each pressure transducer and the corresponding voltage output set to 1 and 5 volts. Using these values, the linear calibration equation was obtained. The slope and intercept obtained from the equation were input to the Camile system. P0 was calibrated with a slope of 15.3229 and intercept of –14.6678, while P1 had slope of 3.7602 and intercept –3.7442. The temperature reading from the thermocouple probes could be directly interpreted by Camile in ^{o}F or ^{o}C. The data from Camile was initially saved in text format, which was later converted to an Excel worksheet.

Configuration and assembly details of the flow loop are presented in Appendix C.

2.3.4 Validation of Saltwell Test Loop

The saltwell test loop was validated, by performing water tests on the system. The calculated values were obtained from the modified Bernoulli equation [41,44]:

$$\frac{P_1}{\rho \cdot g}+\frac{V_1^2}{2 \cdot g}+Z_1=\frac{P_2}{\rho \cdot g}+\frac{V_2^2}{2 \cdot g}+Z_2+f \cdot \frac{L}{D_1} \cdot \frac{V_2^2}{2 \cdot g}+\frac{V_2^2 \cdot K}{2 \cdot g} \qquad (2\text{-}12)$$

where $P_1$and P_2 are the inlet and outlet pressures in the test loop, V_1 and V_2 are the inlet and outlet velocity of water, Z_1(pump level, 0 ft) and Z_2(test loop, 2 ft) are the inlet and outlet datumn(level), L_{tl}(15 ft) is the length of the test loop, f=(64/Re_w) is the friction loss

due to pipe and K' is the friction loss due to pipe fittings. The various fittings and corresponding friction loss coeffcients [41] are tabulated (Appendix B, Table B.2).

Using the friction factors, equation (2-9) is modified as:

$$\Delta P = \left[\left(Z_2 - Z_1\right) + f \cdot \frac{L}{D_{ex}} \cdot \frac{V_{ex}^2}{2 \cdot g} + \frac{V_{ex}^2 \cdot K'}{2 \cdot g} \right] \cdot \rho_W(297) \cdot g \qquad (2\text{-}13)$$

where ΔP was the pressure drop in the line. The total pressure drop in the line is measured as 1.001psi

The pressure drop in the individual section between the two pressure transducers could be calculated from the Bernoulli equation by modifying the following, $Z_1=Z_2$ (since the pressure transducers were at the same level), L=3.5 ft (distance between the two pressure transducers) and $K'=3\cdot K_{tee}+4\cdot K_{coupling}+K_{valve}$. Thus, the pressure drop in an individual section is obtained as ΔP=0.03psi. The pressure drop in the individual section is calculated similarly for different flow rates of water and are compared to experimental values in Table 2.5.

Table 2.5: Comparision of calculated pressure drop in individual section of test loop to experimental pressure drop.

Flow rate (gal/hr)	Calc. pressure drop(PSIG)	Exp. pressure drop(PSIG)
3.5	0.03	0.032
5	0.043	0.044
5.8	0.051	0.051
6.8	0.06	0.061
8	0.071	0.07
8.5	0.076	0.077

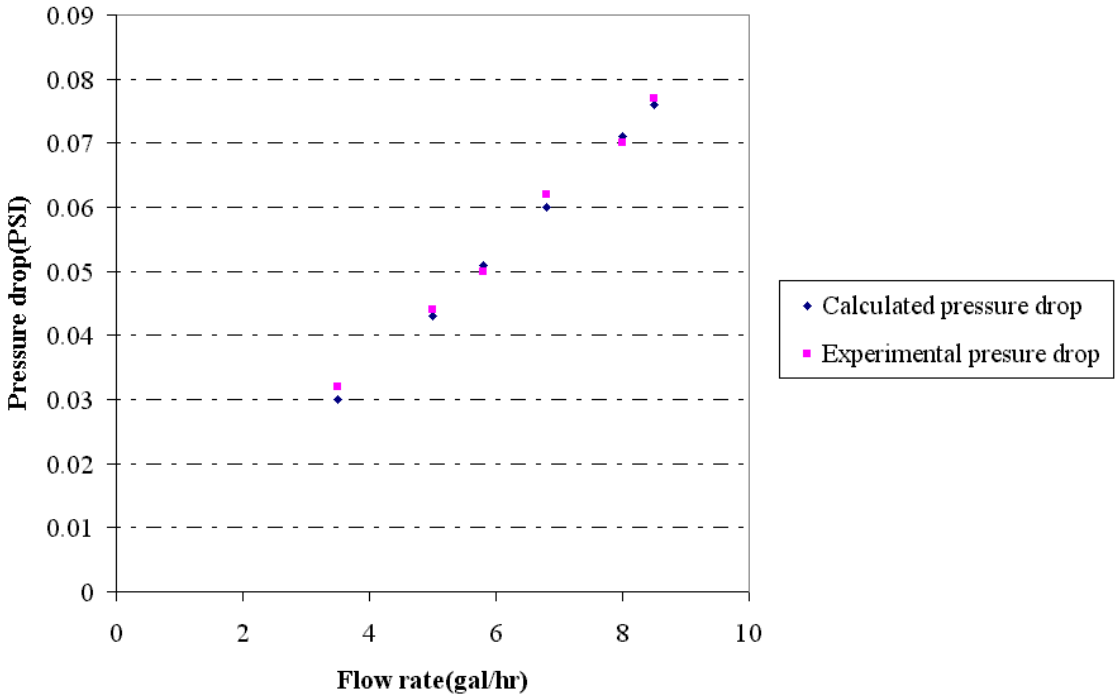

Figure 2.8: Comparision of calculated pressure drop in individual section of test loop to experimental pressure drop.

The comparison shows that the calculated pressure data is in agreement with the experimental pressure data and verifies the calibration.

2.4. Description of Experiments

2.4.1 Saltwell Test Loop Experiments

The general procedure followed in running the saltwell experiments is discussed in this section. Initially, Tank3 was filled with water and heater3 was turned on to raise the tank temperature to 50^{o}C. Clear flexible plastic tubing was fitted to the Valve5 and the other end was left in Tank3. This was done to recycle the water back to Tank3. After Tank3 reached the desired set temperature, Valve3 was opened and the surrogate pump (Pump1) turned on. Hot water from Tank3 was used to preheat the line. Water flushed the

line until the thermocouples in the line achieved temperatures greater than 50^{o}C. At this point, Pump1, Valve3 and Valve5 were turned off and the flexible PVC tubing disconnected from the line. Pump1 and Valve1 were then turned on and surrogate started flowing in the line. About 500 cc of liquid was collected from the line using the downstream Valve5 and the remaining surrogate directed to Tank2 through a flexible PVC tube. This was done to remove any water left in the line following preheating. The surrogate flow rate was initially set to a maximum (20 gph) and then reduced to the required level. The surrogate flow continued until T5 reached a temperature of 46^{o}C. This was an arbitrary temperature used at which the heat exchanger was turned on. The surrogate in Tank2 was periodically recycled back to Tank1 using Pump2.

In the experiments without the clear section, FM3 or FM4 was used at a specified flow rate of cooling water and correspondingly, Hex3 or Hex4 cooled the line and the surrogate temperature decreased. Based on the heat exchanger used, the temperature of the section downstream of the exchanger decreased. In this way, the surrogate temperatures fell to around 40^{o}C where solids formation and deposition were observed followed by eventual plug formation. The pressure and temperature profiles corresponding to the flow were monitored using the Camile system. Plug formation was preceded by an increase in pressure eventually attaining a maximum, which corresponded to the pump head. At this point all flow ceased. When the clear section was used, the cooling water flow meter was set at a predetermined flow rate and the section downstream of Hex2 cooled.

Plugging experiments were done at different surrogate flow rates, cooling water flow rates and varying phosphate concentrations in the recipe. Though most experiments

required the use of only one heat exchanger, some experiments at lower phosphate concentrations required two exchangers. For some experiments, particles and bed growth were observed using a color video camera. The images were then analyzed to provide a better understanding of the plug formation phenomena. Because of the resolution of this camera, the images were not clear. In later runs, the DIAL imaging system was used to provide better images. Before image analysis of each run, images were calibrated using the spatial selections in the imaging software. The time to plug varied from about 4 min to 8100 min based on the surrogate flow rate.

At the end of an experiment, the section upstream of the heat exchanger was cleared of the surrogate by turning the ball valve in front of the exchanger to the off position and the sample port on. The section of the plug downstream of the heat exchanger was then unplugged using hot water from Tank3. Unplugging was recorded using the video camera and typically ranged from 14 min to 2 hrs based on the time the plug was left in the test loop. The unplugging video was used to analyze the process in greater detail.

2.4.2 Test Matrix

The test matrices for plugging and unplugging experiments in the saltwell test loop are in Tables 2.6-9.

Table 2.6: Test matrix for saltwell plugging experiments at varying surrogate flow rates.

Surrogate Temperature ^{o}C	**Surrogate Flow Rate (Gal/hr)**	**Cooling Water Flow Rate (Gal/min)**
50	3.5	1.2
50	5	1.2
50	5.8	1.2

Table 2.6: Test matrix for saltwell plugging experiments at varying surrogate flow rates - continued.

50	6.8	1.2
50	8	1.2
50	8.5	1.2

Table 2.7: Test matrix for saltwell plugging experiments at varying cooling rates.

Surrogate Temperature ^{o}C	**Surrogate Flow Rate (Gal/hr)**	**Cooling Water Flow Rate (Gal/min)**
50	6.8	0.4
50	6.8	0.6
50	6.8	0.7
50	6.8	1.2

Table 2.8: Test matrix for saltwell plugging experiments at varying phosphate concentrations.

Surrogate Temperature (C)	**Phosphate Concentration (M)**	**Surrogate Flow Rate (Gal/hr)**	**Cooling Water Flow Rate (Gal/min)**
50	0.22	6.8	1.2
50	0.15	6.8	3
50	0.11	6.8	1.2, 3[a]

a Cooling rate of 1.2 gpm on Hex1 and 3 gpm on Hex2.

Table 2.9: Test matrix for saltwell unplugging experiments.

Temperature of Flush Water(C)	**Surrogate Flow Rate (Gal/hr)**	**Time for which plug is left in test loop(hrs)**
50	3.5	2
50	3.5	6
50	3.5	12
50	3.5	25
50	3.5	49
50	5	26
50	6.8	2
50	6.8	6
50	6.8	25

CHAPTER III

RESULTS

3.1 Introduction

Details of the saltwell pumping test loop experiments are discussed in this section. The design and construction of the saltwell test loop were discussed previously (Chapter 2.3). Experiments to understand the formation of pipeline plugs were performed as well as tests to examine the efficiency of unplugging with water. The pipeline plugging experiments were performed at different surrogate flow rates and cooling rates and different phosphate compositions. Results center on the experiments where the clear channel was installed and images of particles, agglomerates and plug formation were obtained.

3.2 Plugging Experiments

3.2.1 Experiments at Surrogate Flow Rate of 3.5 gph

Multiple experiments were done at a flow rate of 3.5 gph (Re=223) as discussed earlier (Chapter 2.4). Heat Exchanger (Hex2) was used with a cooling water flow rate of 1.2 gpm. The thermocouple T2 was located before Hex2 and T4 downstream after the section of clear piping as shown in Figure 2.7. Pressure transducers P0 and P2 were located adjacent to T2 and T4. The pressure and temperature profiles for a typical experiment with surrogate flow at 3.5 gph are given in Figure 3.1. Temperature profiles

from the thermocouples on the test loop and for the holding tanks are included. The profiles correspond to the time following activation of the heat exchanger.

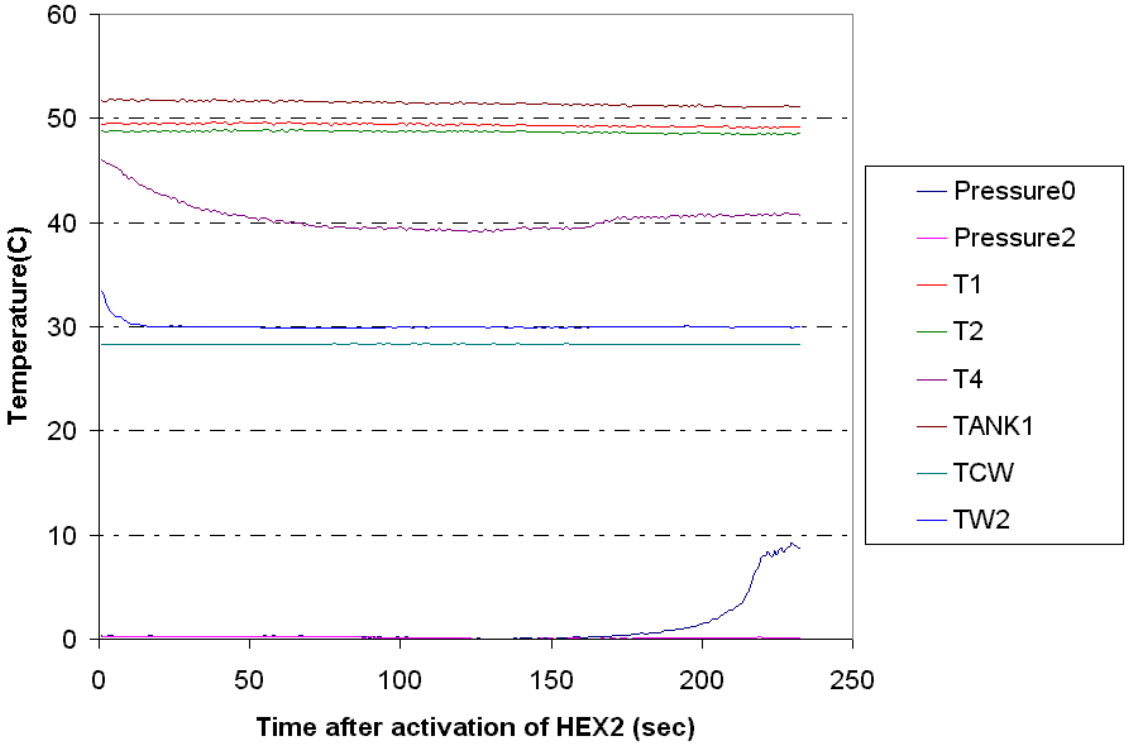

Figure 3.1: Temperature and pressure profiles in experiment with surrogate flow rate of 3.5 gph.

Variations in tank and channel temperatures were observed for longer duration runs due to the cycling of the immersion heater in the surrogate holding tank. Hex2 was turned on when the temperature of T4 reached ≈ 46^{o}C. The profile of T4 showed that the temperature decreased gradually and stabilized around 40^{o}C. The reason for the slight increase in temperature of T4 around 160 seconds is not known. The increase was not observed in any other runs under similar conditions, indicating a possible error in the thermocouple reading. The temperature profiles of T1, T2 and Tank1 remained stable and were not affected by the cycling of the immersion heater (short run duration). P0 remained constant until about 150 seconds after Hex2 was activated, then it started to

increase gradually. The increase in P0 became rapid around 190 seconds and continued until the test section finally plugged around 250 seconds. The maximum pressure reading on P0 was about 8.8psig, which corresponded to the total pump pressure. The pressure reading on P2 remained constant throughout the run, which indicated that the plug formed between P0 and P2, possibly in the clear section. The constant pressure reading of P2 could be attributed to the higher downstream temperature that prevented plug formation in that section. Based on the temperature and pressure profiles, the plug formation properties such as the time to plug, the temperature at plug, the total temperature drop and the total pressure increase were obtained (Table 3.1 & Table 3.2).

Table 3.1: Results of experiments at surrogate flow rate of 3.5 gph (Re=223)

Date	Surrogate Flow Rate(gph)	Hex2 Cooling Rate (gal/min)	Time to Plug (sec)	Pressure at Plug(PSIG)	T5 Rate of Temp Change (C/sec)	T5 at plug (C)
3/6/2001	3.5	1.2	254	8.81	0.06	38.77
3/11/2001	3.5	1.2	262	8.91	0.06	38.45
3/12/2001	3.5	1.2	255	8.87	0.05	38.91
3/17/2001	3.5	1.2	259	8.93	0.07	39.16
3/18/2001	3.5	1.2	261	8.83	0.05	39.01

Table 3.2: Average values of experiments at surrogate flow rate of 3.5 gph.

	Time to Plug (sec)	Pressure at Plug (PSIG)	T5 Rate of Temp Change (^{o}C/sec)	T5 at Plug (^{o}C)	Change in T5 (^{o}C)
Average	258.20	8.87	0.06	38.86	5.77
Std. Dev	3.56	0.05	0.01	0.27	0.16
Std. Err%	1.38	0.58	14.43	0.69	2.75

In Table 3.1, the time to plug was the time between activation of the heat exchanger and the formation of the plug. The rate of temperature change was the change in T4 temperature for the duration of the process. Based on the data in Table 3.2, it was observed that the plug formation process was reproducible.

To obtain a better understanding of the plug formation process, image analysis of the plugging process was performed by replacing a section of the test loop with a clear plastic pipe. Initial analysis was performed using a color video camera with an automatic zoom feature. The video from the camera was saved on the computer as a video file (Appendix E, Movie 1). The video file was then framed to obtain images corresponding to each frame. The video provided an insight into the plugging process; however, critical information like particle size and growth characteristics could not be ascertained from the images because of the limited spatial resolution of the camera. Further, the process was tedious although frame analysis could be performed. In view of this, the video camera was later replaced with the DIAL imaging system as discussed previously (Chapter 2.4.1). Images were collected in a 2" clear section located about 19" from Hex2 and at a frequency of 12.5 frames/sec. The surrogate flow rate required that the images be collected frequently, such that the particle and agglomerate growths could be viewed in greater detail. Bitmap images from the imaging system were converted to grayscale, which were enhanced and cropped prior to analysis.

Images were collected during the experiment with surrogate flow rate at 3.5gph. The corresponding temperature and pressure profiles are presented in Figure 3.1. Image collection started around 150 seconds after Hex2 was activated and continued until a plug formed. The resolution of the imaging system was 13.1 pixels/mm with an accuracy of +/- 1 pixel, which corresponded to a minimum particle resolution of 80 microns. The first "observable" particles were seen in the channel after 150 seconds, though smaller particles may have previously been in the line. The results of image analysis were divided into four sections, namely: single free particles, single sedimenting particles,

agglomerating particles and bed development. The particles are consistent with those shown in the PLM image (Figure 2.6) and are identified as $Na_3PO_4 \cdot 0.25\ NaOH \cdot 12H_2O$.

Single free particles were defined as the particles, which traversed the section of the channel without being deposited. Representative frames for 2 sets of single free particles are shown in Figures 3.2 and 3.3.

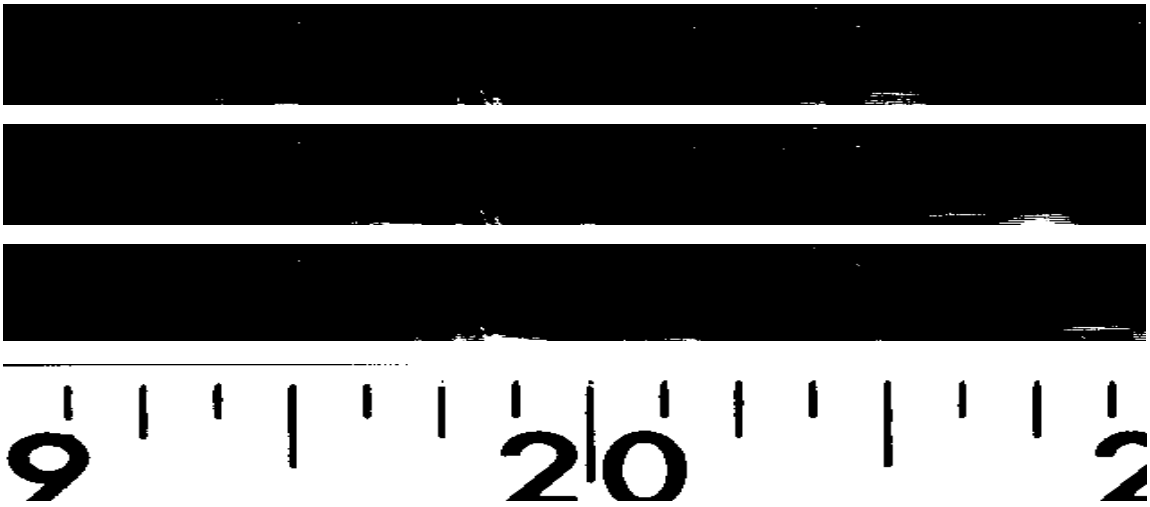

Figure 3.2: Representative frames for single free particles observed 208.72 seconds after Hex2 was activated.

Figure 3.3: Representative frames for single free particles observed 202.08 seconds after Hex2 was activated.

In Figure 3.2, the single free "rod-shaped" particle first appeared over the 19 7/8" mark. In the consecutive frame, the particle grew in size and appeared over the 20 ¼" mark. The particle continued to grow while traversing approximately the same distance in the subsequent frames. This implied that the velocity of the particle in the particular data set was approximately the same while it continued to grow in size. In Figure 3.3, the first particle appeared over the 20 ¼" mark and exhibited the same kind of behavior as in Figure 3.2.

Image analysis was performed to obtain the length and width of the particles in each of the images. The area of the particle was calculated by using the length and width, with the length being in the direction of flow and assuming an elliptical shape. The axial ratio was obtained as a ratio of length to width of the particles. The velocity of the particle in the direction of the flow was calculated by taking the ratio of the distance traversed by the particle over the time difference between the frames. Consolidated data for all the single particles observed are given in Table 3.3. Dimensions correspond to those measured in the last image and thus, represent the largest size attained by the particle before it moved out of the 2" observation region. Similar comments apply to the velocity. The time corresponding to the observation of the first and last image of the single particle in each data set is given.

Table 3.3: Image analysis results for free single particles.

Start (sec)	End (sec)	Length (mm)	Width (mm)	Avg. L/W	Std. L/W	Area (mm^2)	V_x (cm/sec)	Std. V_x (cm/sec)
196.24	196.56	2.21	0.47	4.86	0.69	0.82	7.96	0.18
202.08	203.32	2.77	0.51	5.44	1.64	1.10	7.92	0.26
208.72	208.96	2.10	0.58	4.94	1.13	0.95	7.42	0.33
209.60	209.92	1.92	0.31	4.59	1.83	0.47	6.77	0.38
212.56	212.80	2.22	0.56	3.63	1.04	0.98	6.96	0.22

Table 3.3: Image analysis results for free single particles - continued.

214.96	215.28	2.15	0.62	3.45	0.24	1.05	6.48	0.38
217.92	218.40	3.46	0.56	5.81	1.10	1.53	6.27	0.31
218.96	219.28	3.30	0.45	6.71	0.59	1.16	6.21	0.24

The first single free particle was observed 196.24 seconds after Hex2 was activated while the last one was observed after 218.96 seconds. The final length to which the particle grew varied between 1.92 to 3.46mm while the final width of the particle varied between 0.31 to 0.62mm. This was indicative of the varying growth rates and position where the particles started to grow in the channel. The axial ratios varied from 3.45 to 6.71 validating the assumption of an elliptical shape in the calculation of area. The area of the single particles varied from 0.82 to 1.53 mm^2 based on the length and width of the particle. The stream velocity decreased as particles formed and resulted in a decrease in particle velocity. The standard deviation values of the axial ratio and velocity of the particles indicate the variation within each data set. Within a set, the length of a single particle generally increases more than the width resulting in increases in the axial ratio. The velocity changes result from the variation in length of particles in successive frames.

Single sedimenting particles have been defined as those particles that deposited in the channel and are shown in Figure 3.4.

Figure 3.4: Representative frames for single sedimenting particles observed 194.72 seconds after Hex2 was activated.

A single particle was observed over the 19 1/2" mark. The particle grew in the consecutive frame before it deposited in the channel at the 20 ¼" mark. The consolidated data for all the single sedimenting particles observed are given in Table 3.4.

Table 3.4: Image analysis results for single sedimenting particles.

Start (sec)	End (sec)	Length (mm)	Width (mm)	Avg. L/W	Std. L/W	Area (mm^2)	V_x (cm/sec)	Std. V_x (cm/sec)
194.72	195.12	3.14	0.71	4.83	0.15	1.76	7.89	0.26
217.52	217.84	3.98	1.09	4.55	1.21	3.41	5.45	0.68

The length and width of each particle calculated using the imaging software were used to obtain the axial ratio, area and velocity as before. The lengths and widths of the sedimenting single particles were greater, as expected, than that of the free single particles. This implied that the dimensions of the sedimenting particles exceeded the critical dimensions (see below).

Agglomerates were defined as clusters of single particles that occurred in the channel due to inter-particle interaction. Because of the presence of multiple particles, the agglomerates were much bigger than the single or sedimenting particles. The representative frames for two sets of agglomerates are presented in Figure 3.5 and Figure 3.6.

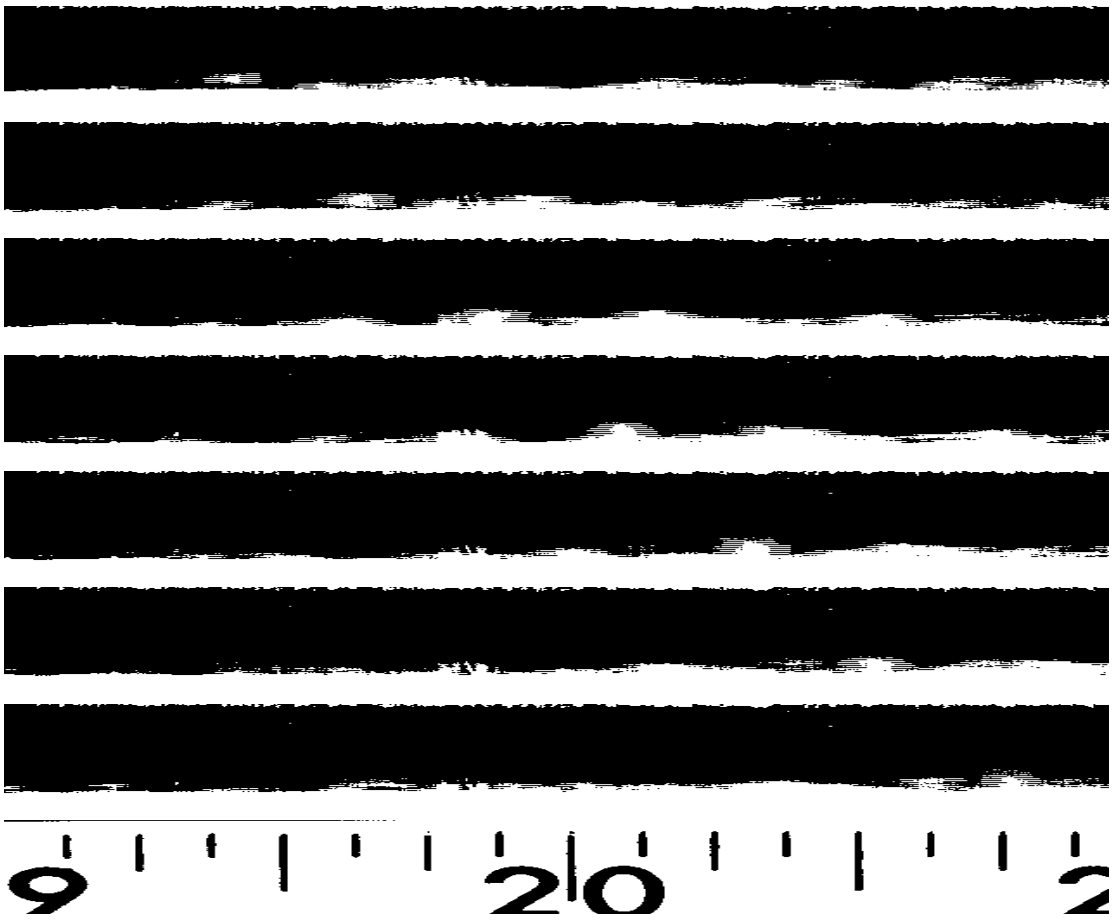

Figure 3.5: Representative frames for agglomerating particles observed 207.84 seconds after Hex2 was activated.

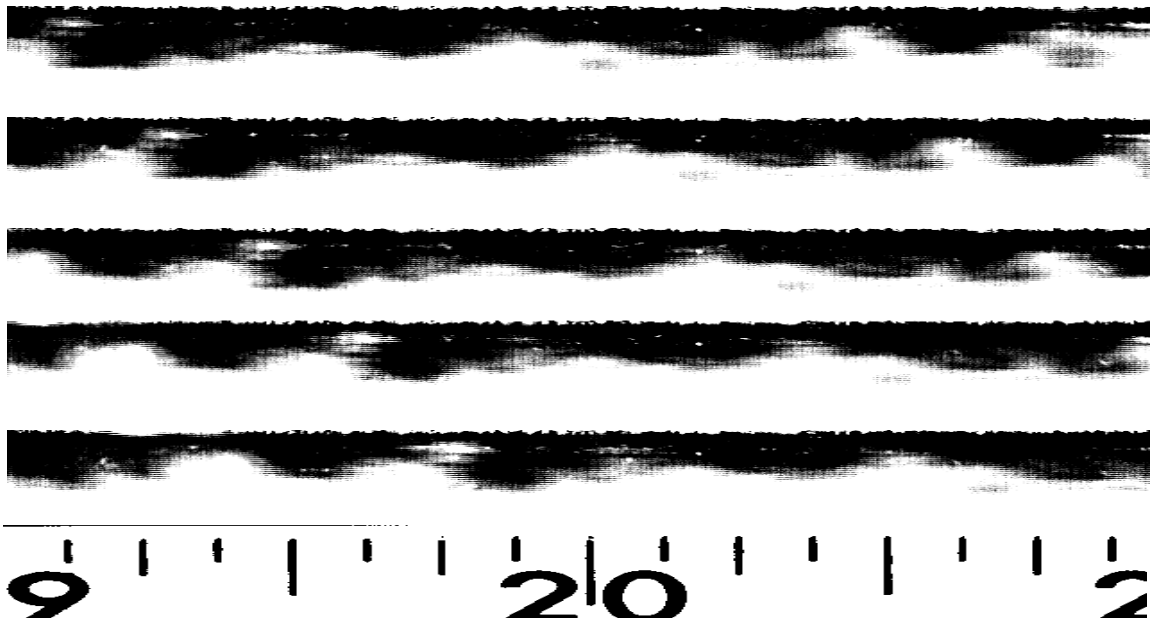

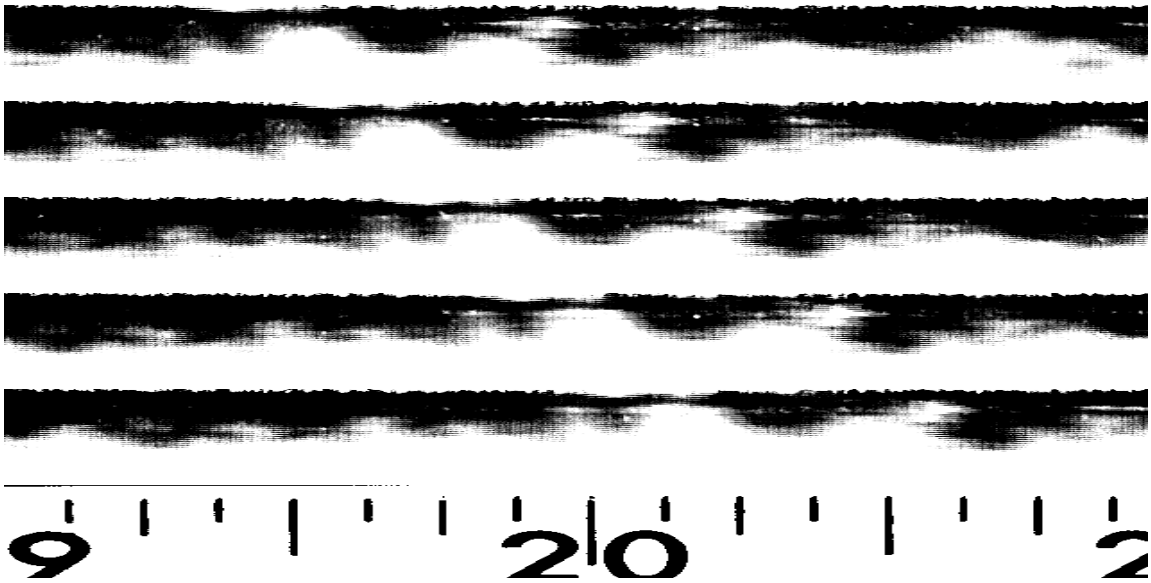

Figure 3.6: Representative frames for agglomerating particles observed 215.92 seconds after Hex2 was activated.

The agglomerate was first observed, in Figure 3.5, over the 19 ¼" mark. The agglomerate continued to grow and deposited at the bottom of the channel at the 19 7/8" mark. The particles and agglomerates, which deposited at the bottom of the channel, continued to move along with the flow and constituted a "moving" bed. The bed continued to grow with time as more deposits occurred. The first set of images in Figure 3.5 was in the early part of the deposition when the bed area was negligible while the second set in Figure 3.6 was during the later part of the run when the bed area was increasing. Based on the images in Figures 3.5 and 3.6, bed area did not appear to affect the formation and deposition of the agglomerates. Results from image analysis of the agglomerates are collected in Table 3.5.

Table 3.5: Image analysis results for agglomerating particles.

Start (sec)	End (sec)	Length (mm)	Width (mm)	Avg. L/W	Std. L/W	V_x (cm/sec)	Std. V_x (cm/sec)
204.08	204.40	3.48	1.38	4.67	2.03	7.85	0.23
206.00	206.48	4.54	1.69	2.60	0.28	7.51	0.57
206.40	206.64	3.18	1.10	4.19	1.52	6.14	0.48

Table 3.5: Image analysis results for agglomerating particles - continued.

206.72	207.04	4.37	1.25	3.55	0.66	7.42	0.38
207.44	207.60	2.87	1.30	3.50	1.15	6.32	1.13
207.84	208.40	3.36	1.63	2.69	0.44	7.23	0.35
208.48	208.72	3.61	1.25	3.40	0.45	6.14	0.37
213.44	213.68	5.15	1.39	3.00	1.27	5.47	0.73
213.84	214.32	3.54	1.48	2.78	0.73	5.52	0.15
215.28	215.60	4.01	2.15	2.20	0.66	5.42	0.09
215.92	216.56	4.37	1.84	2.47	0.87	5.13	0.29
216.72	217.04	2.92	1.90	2.12	0.88	5.08	0.13
217.04	217.52	3.88	1.16	3.59	0.66	4.75	0.58
217.52	217.84	4.02	1.33	4.00	1.74	5.09	0.37
217.92	218.16	3.86	2.14	1.63	0.21	4.75	0.5
217.92	218.32	5.95	1.54	4.27	0.90	4.61	0.15
220.08	220.48	4.02	1.91	3.92	2.14	4.62	0.64
220.16	220.32	4.37	2.06	2.29	0.22	4.61	0.22
221.84	222.08	4.61	2.48	2.30	0.45	4.01	0.56
222.08	222.40	5.18	2.14	2.32	0.44	3.8	0.15

From Table 3.5, it is evident that the agglomerates were much larger in size compared to the single particles in Table 3.3. The calculated axial ratios of the agglomerates were less than that of the single particles suggesting that the agglomerates grew more in their width than length when compared to the single particles. The velocity of the agglomerates gradually decreased over the course of the run suggesting that the stream velocity reduced with the formation of agglomerates and increased bed area.

The image analysis data from Tables 3.3 and 3.5 were regressed against time to obtain the growth rates of the single particles and agglomerates. This also enabled a better understanding of the occurrence of higher axial ratios of agglomerates when compared to single particles. The regression data for the growth in area of single particles and agglomerates are given in Tables 3.6 and 3.7.

Table 3.6: Regression data for area growth of single particles.

Start (sec)	End (sec)	Slope (mm^2/sec)	Intercept (mm)	Correlation Coefficient
196.24	196.56	2.4	-467	0.91
202.08	203.32	1.5	-292	0.73
208.72	208.96	2.8	-573	0.98
209.60	209.92	1.7	-360	0.85
212.56	212.80	2.0	-474	0.98
214.96	215.28	1.8	-383	0.84
217.92	218.40	2.4	-516	0.84
218.96	219.28	1.9	-409	0.96
	Average	2.1		
	Std. Dev	0.4		

Table 3.7: Regression data for area growth of agglomerates.

Start (sec)	End (sec)	Slope (mm^2/sec)	Intercept (mm)	Correlation Coefficient
206.00	206.48	7.7	-1540	0.91
206.40	206.64	4.9	-1603	0.90
207.44	207.60	10.2	-2117	0.99
207.84	208.40	4.2	-860	0.78
208.48	208.72	10.7	-2249	0.94
213.44	213.68	21.6	-4612	0.78
213.84	214.32	6.9	-1470	0.97
215.28	215.60	19.5	-4165	0.93
215.92	216.56	9.3	-2002	0.83
216.72	217.04	11.9	-2584	0.91
217.92	218.16	17.6	-3822	0.63
217.92	218.32	15.4	3400	0.99
220.08	220.48	10.0	-2189	0.90
220.16	220.32	13.5	-2965	0.97
221.84	222.08	21.6	-6124	0.98
222.08	222.40	24.8	-5525	0.91
	Average	13.1		
	Std. Dev	6.3		

From the regression data of the single particles in Table 3.6, it is seen that the growth of area was 2.0±0.4 mm^2/sec while the agglomerates in Table 3.7 had a growth rate of 13.1±6.3 mm^2/sec. It was also noted that the growth rate of single particles was almost

the same for all the data sets collected while the agglomerates grew as a function of time. A linear fit was used for regression of data in the absence of a better fit. As the correlation coefficients were reasonable for both the single particles and agglomerates, the linear fit was assumed to be adequate.

To further investigate the cause of higher area growth rates in agglomerates than single particles, regressions were performed on the length and width data from the image analysis. The growth in length of the single particles was determined as 2.9±1.7 mm/sec while that of agglomerates was 5.9±4.7 mm/sec. Similarly, the growth in width of single particles was determined as 0.6±0.9 mm/sec and that of agglomerates was 3.1±1.5 mm/sec. From the regression data, it was observed that though the growth in width of agglomerates was about 5 times that of single particles, the growth in the length of the agglomerates was just 2 times that of the single particles. This indicated that the agglomerates grew more in their width compared to length resulting in smaller axial ratios.

As the agglomerates were defined as clusters of single particles, the growth rate of agglomerate was a function of growth of the single particles and the number of particles comprising the agglomerate. The growth rate of single particles was observed to be constant from the regression data (Table 3.6). This observation suggests that the increasing growth rate of agglomerates with time may have been due to the greater number of single particles comprising the agglomerates. In order to investigate the observation, the agglomerate growth rate was divided by the average single particle growth rate to obtain a calculated number of single particles comprising the agglomerate. The calculated value was then compared with the number of particles from visual

observation. The values are plotted in Figure 3.7. The calculated and observed number of particles comprising the agglomerate increase with time, thus resulting in an increase of agglomerate growth with time.

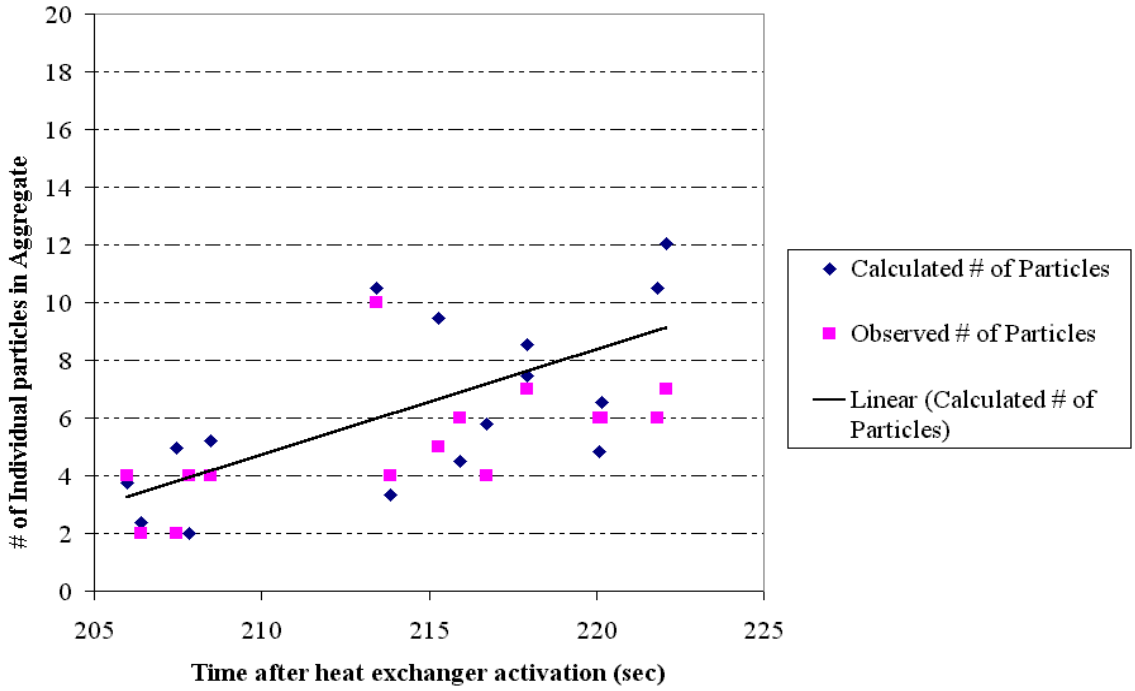

Figure 3.7: Calculated and observed # of particles comprising agglomerate.

The area growth rates of the single particles and the agglomerates along with the pressure and temperature profiles are plotted against time in Figure 3.8. This enabled an understanding of the transition from single particle growth to agglomerate formation prior to bed development. Further the particle growth and agglomerate formation could be related to the pressure increase in the channel. The pressure data in the plot are from the transducer located before the heat exchanger, Hex2. The transducer showed a pressure reading of about 1psig even before the first particle was observed. This indicated the existence of particles in the line before 190 seconds, either smaller than the set resolution of the camera or up or downstream of the 2" section used for image analysis. It

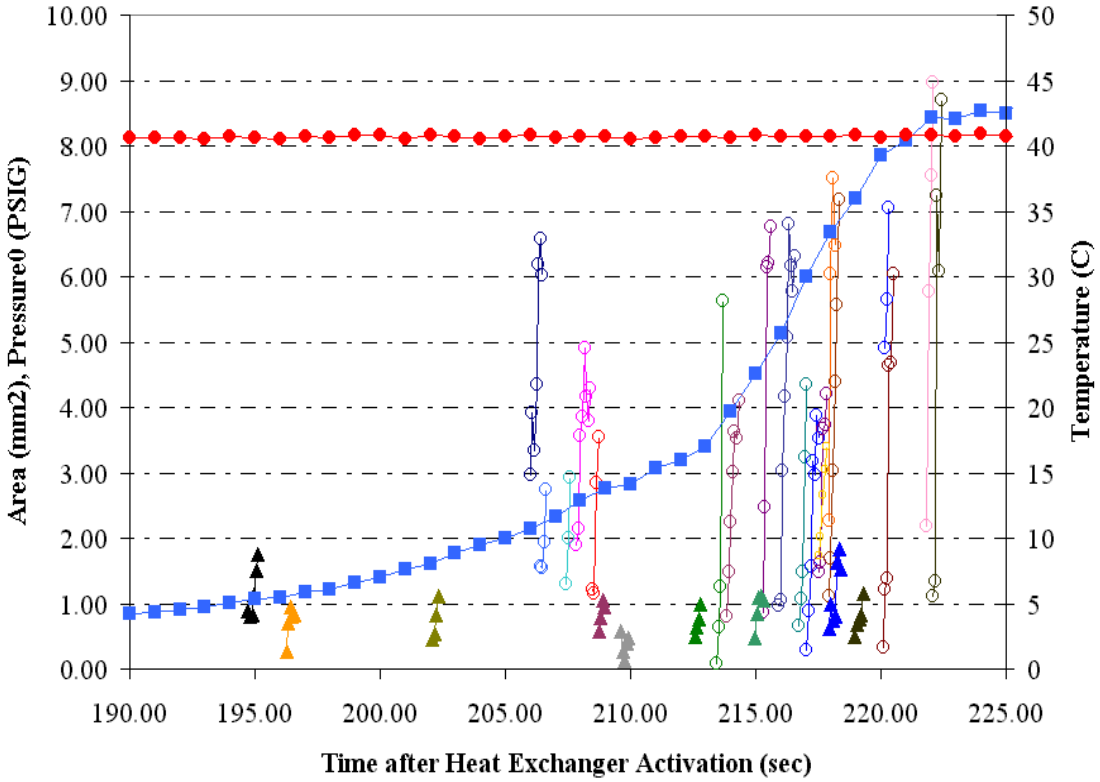

Figure 3.8: Plot of particle, agglomerate area and Pressure0 as function of time after activation of Hex2. The triangles in the plot represent the single particles while the circles represent the agglomerates. The blue solid line with squares represents Pressure0 and red solid line with circles represents T4.

appears likely that the initial deposition of the particles occurred downstream of the plug location. If particle sedimentation and agglomeration had occurred upstream of the probe volume, particles and agglomerates would be observed at earlier run times. Some movement of the agglomerates along the bottom of the channel would have also been observed in the initial images. The surrogate stream mainly consisted of single particles until about 206 seconds when the agglomerates started to form. Following this time, the single particles were still observed although agglomerate formation became predominant. The single particle growth was uniform throughout, while the agglomerate growth increased with time. The stream velocity gradually reduced with time causing the agglomerates to increase in size or “pile-up” over the existing agglomerates forming

bigger agglomerates as shown in Figure 3.5 and Table 3.5. This supports the observation that the agglomerates grew more in width than in length.

The pressure rise in the transducer was gradual until about 213 seconds and then increased rapidly as observed from the two distinct slopes in Pressure0 before and after 213 seconds. Prior to 213 seconds, the stream mainly contained single particles and the obstruction to flow was less and the corresponding pressure rise was gradual. Later, when the agglomerates became predominant, the rate of bed formation also increased resulting in flow obstruction and a rapid increase in pressure. It was observed from the plot that when the last agglomerate was seen in the channel (223 seconds after Hex2 activation), the pressure reading was close to the maximum value. At this point, the moving bed was fully developed and a decrease in the velocity was observed followed by plug formation. The line plugged about 230 seconds after activation of Hex2 when the maximum pressure was observed. This indicated that the pressure drop in the channel was directly proportional to the particles in the line. Thus the pressure drop, because of frictional effects, increased with increasing particle concentration. The temperature in the channel remained fairly constant throughout the duration of image analysis. Hex2 was turned on at T4 temperature of 46^{o}C and the temperature stabilized around 40^{o}C after 150 seconds and even slightly increased towards the end of the runs. The depositing single particles and agglomerates formed a bed, which continued to move along with the flow. Bed areas obtained at regular run times are analyzed using the image analysis software. The bed fraction (ratio of bed area to total channel area) was plotted against time to understand the effect on pressure rise and is shown in Figure 3.9. An increase in the pressure is observed with increasing bed fraction. The bed started to form around 200 seconds due to the

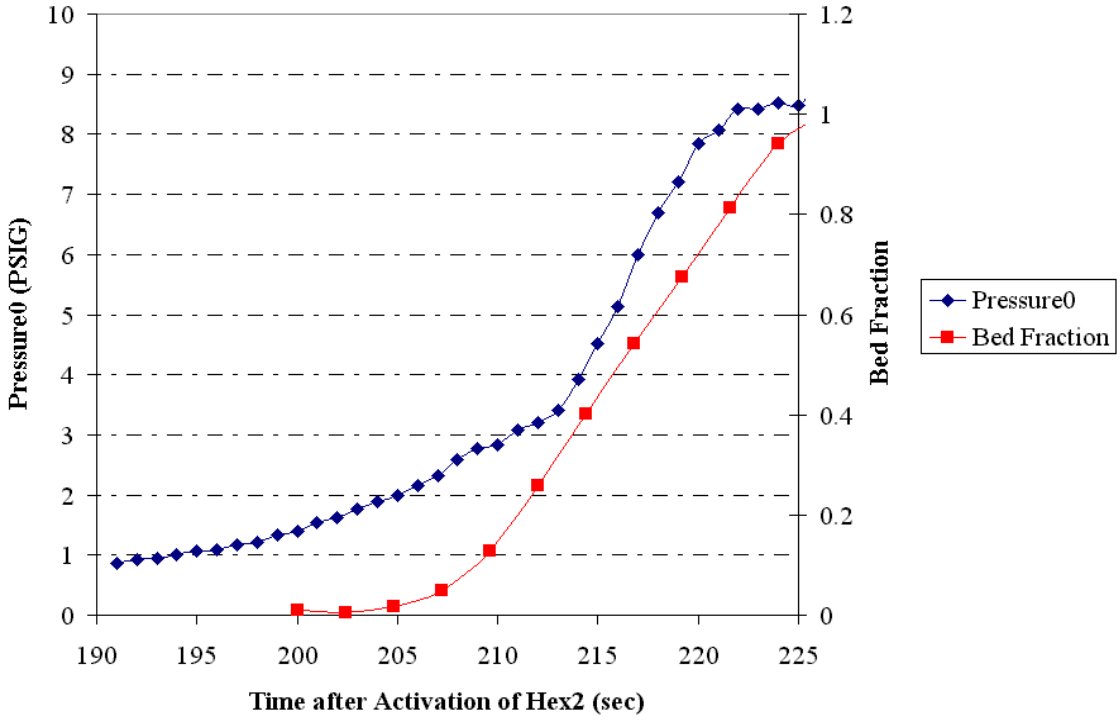

Figure 3.9: Plot of bed fraction and Pressure0 as function of time.

depositing single particles in the channel. The bed growth was gradual until about 208 seconds, when it started to increase rapidly. This was attributed to the agglomerates, which were clusters of single particles that deposited in the channel causing the bed to grow rapidly. The bed fraction reached the maximum value of 1 around 225 seconds indicating that the bed had fully developed in the channel. The bed movement gradually slowed down because of the frictional effects before finally ceasing around 240 seconds and resulted in a plug.

3.2.2 Experiments at Surrogate Flow Rate of 6.8gph

In view of the short plugging time in experiments at 3.5 gph, further experiments were done at a higher flow rate of 6.8 gph(Re=436). The main idea was to investigate the effect of higher flow rates on the plugging process. The experiments were done in a

similar fashion as before while varying the surrogate flow rate. The temperature and pressure profiles from a typical experiment are shown in Figure 3.10. As before, the heat exchanger (Hex2) was turned on at 1.2 gpm when the exit temperature of surrogate at T5 reached about 46°C. The surrogate temperature at T5 stabilized around 42°C and the channel finally plugged around a temperature of 41.6°C. The pressure profile remained constant until a time of approximately 2000 seconds and then started to increase. This could be compared to 150 seconds in the 3.5 gph run when the pressure remained constant. The pressure rise in P0 was gradual between 2000 seconds and 2800 seconds and then increased rapidly. The channel plugged at a run time of 2940 seconds after Hex2 was activated. The variation of the tank temperature and the temperature measured at T1

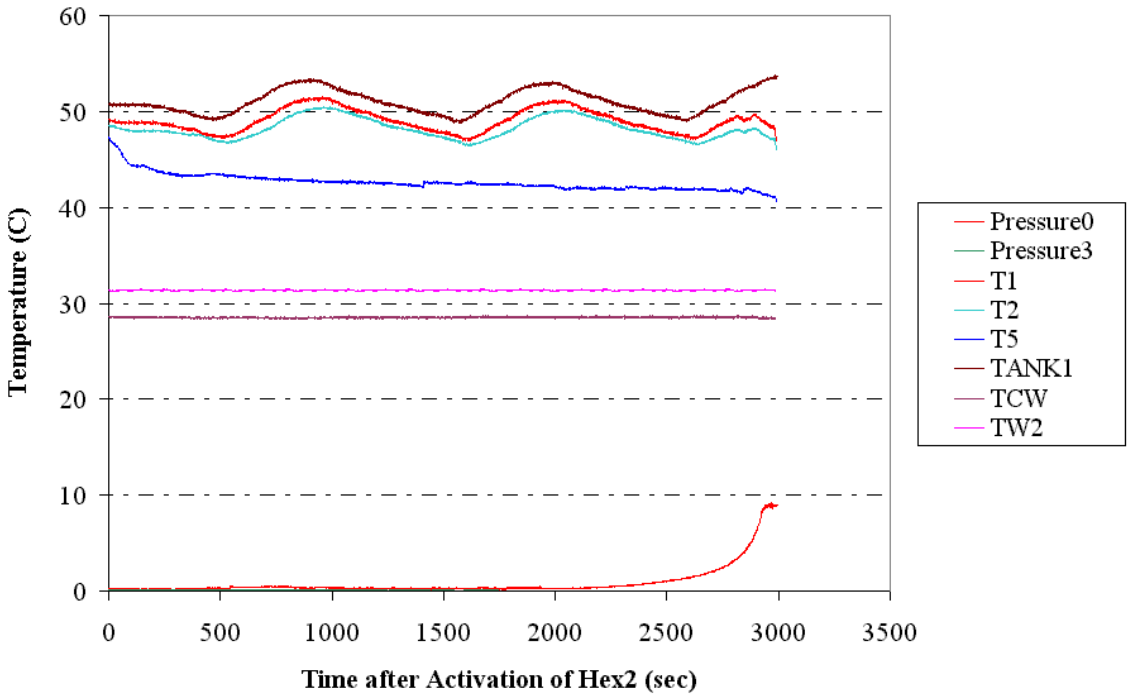

Figure 3.10: Temperature and pressure profiles in experiment with surrogate flow rate of 6.8 gph.

and T2 was due to the cycling of the immersion heater in the surrogate tank. The variation appeared more prominent when compared to the 3.5 gph run because of the longer experimental time. The constant profiles of inlet and outlet heat exchanger temperatures (TCW and TW2) indicated that the cooling heat flux supplied by Hex2 was constant. The pressure reading of P2 remained constant throughout the run indicating that the plug occurred upstream of P2, in the clear section. The temperature and pressure profiles were used to obtain the time to plug, the plugging temperature and other information pertinent to plug formation and are presented in Table 3.8 and Table 3.9.

Table 3.8: Results of experiments at surrogate flow rate of 6.8 gph (Re=436)

Date	Surrogate flow rate (gph)	Hex2 cooling rate (gpm)	Time to Plug (sec)	Pressure at Plug (PSIG)	T5 Rate of Temp Change (^oC/sec)	T5 at plug (^oC)
2/22/2001	6.8	1.2	3478	8.94	0.06	42.22
3/10/2001	6.8	1.2	3371	8.86	0.07	41.87
5/22/2001	6.8	1.2	2930	8.98	0.06	41.72

Table 3.9: Average values of experiments at surrogate flow rate of 6.8 gph.

	Time to Plug (sec)	Pressure at Plug (PSIG)	T5 Rate of Temp Change (^oC/sec)	T5 at Plug (^oC)	Change in T5 (^oC)
Average	3260	8.93	0.06	41.94	5.45
Std. Dev	290.47	0.06	0.01	0.26	0.32
Std. Err%	8.91	0.68	7.98	0.61	5.85

From Tables 3.8 and 3.9, it is observed that the average plugging time in the 6.8 gph run was 3260 seconds and the average temperature at plug was 41.94^{o}C. These results can be compared to the average plugging time of 258.2 seconds and plugging temperature of 38.86^{o}C in the 3.5 gph run. This indicated that the plugging temperature was directly related to the surrogate flow rate. Further, it could also be noted that the experiments were reproducible.

Image analysis was performed on the plugging process with a surrogate flow rate of 6.8 gph. Particles were first observed in the line around 2500 seconds. The image analysis has been divided into free particles, agglomerates and bed development. The representative images for free single particles observed in the channel have been given in Figure 3.11.

Figure 3.11: Representative frames for single particles observed 2681.8 seconds after Hex2 was activated.

The single particle was first observed above the 19 3/8" mark. It continued to grow in the subsequent frames and was last observed over the 20.5" mark. The particle approximately moved the same distance in each of the frames indicating that the velocity of the single particles was approximately the same. As before, particle lengths, widths, velocities and axial ratios were obtained. In view of the large number of images, typical results are given below.

Table 3.10: Image analysis results for free single particles.

Start (sec)	End (sec)	Length (mm)	Width (mm)	Avg. L/W	Std. L/W	Area (mm^2)	V_x (cm/sec)	Std. V_x (cm/sec)
2549.56	2549.8	2.19	0.59	4.41	0.95	1.01	15.21	0.22

Table 3.10: Image analysis results for free single particles - continued.

2564.6	2564.84	2.58	0.50	4.53	0.60	1.02	14.89	0.70
2600.2	2600.44	2.40	0.62	4.39	0.54	1.16	14.13	0.68
2624.44	2624.68	2.19	0.71	4.13	1.27	1.23	13.81	0.17
2648.52	2648.76	2.20	0.61	4.84	1.92	1.06	13.87	0.64
2692.36	2692.6	2.43	0.34	5.51	1.24	0.65	12.46	0.49
2739.08	2739.32	2.75	0.70	4.53	0.60	1.50	12.33	0.02
2784.52	2784.76	2.11	0.71	3.54	0.96	1.17	10.99	0.61
2833.48	2833.8	2.82	0.57	5.31	0.63	1.26	10.39	0.39

The length of the single particles varied between 2.11 and 2.82 mm, while the width varied between 0.34 and 0.71 mm. The single particle dimensions in Table 3.10 are comparable to the single particle dimensions in Table 3.3. This indicated that the single particle size did not vary appreciably with the surrogate flow rate. The single particle velocity reduced from 15.21 cm/sec at 2550 seconds to 10.39 cm/sec at 2833 seconds owing to particle formation in channel.

Sedimenting particles were not observed in the 2” imaging length during the experiment. Particle dimensions were smaller than those required for settling (see below) and thus were carried away by the stream.

Agglomerates were observed in the channel and form the starting point for plug formation. Representative frames obtained from image analysis are shown in Figure 3.12.

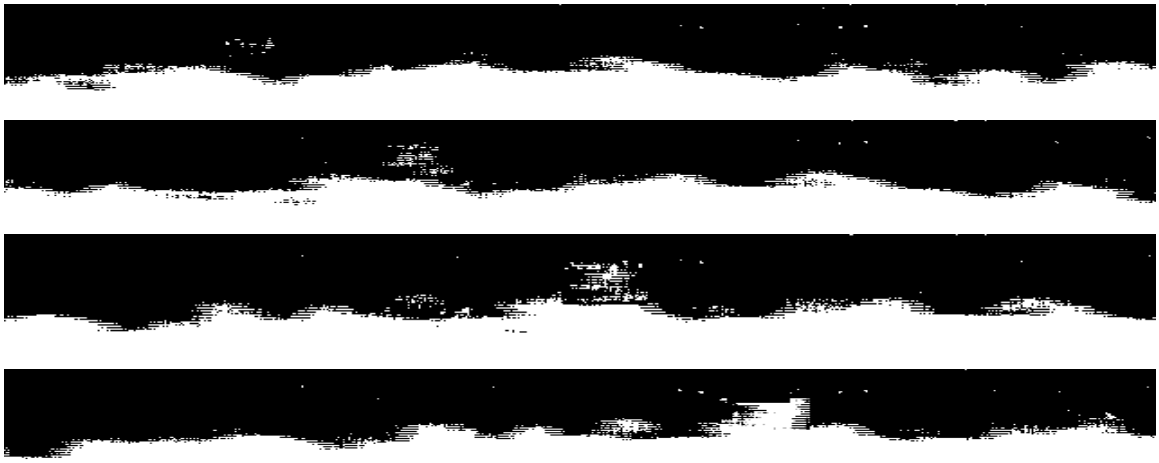

Figure 3.12: Representative frames for agglomerates observed 2818.68 seconds after Hex2 was activated.

A typical agglomerate was first observed over the 19 3/8" mark. The agglomerate grew over the successive frames and deposited close to the 20 3/8" mark. A second agglomerate was observed in the 3rd frame in Figure 3.11 above the 19 ¾" mark. The bed at the bottom of the channel, consisting of the deposited particles and agglomerates, was observed in the images. Results of some of the typical image sets are given in Table 3.11.

Table 3.11: Image analysis results for agglomerates.

Start (sec)	End (sec)	Length (mm)	Width (mm)	Avg. L/W	Std. L/W	Area (mm^2)	V_x (cm/sec)	Std. V_x (cm/sec)
2615.56	2615.8	2.93	0.88	3.35	0.41	2.02	12.84	0.68
2693.24	2693.48	2.77	1.15	2.42	0.30	2.51	12.50	0.73
2739.08	2739.24	2.99	1.42	2.80	1.15	3.34	11.69	0.17
2768.92	2769.16	4.41	2.29	1.59	0.45	7.95	11.14	0.27
2784.44	2784.68	3.95	1.82	2.68	0.50	5.65	9.49	0.91
2805.72	2805.88	3.29	1.93	2.19	0.87	4.98	9.71	0.08
2818.68	2818.84	3.40	2.53	1.68	0.41	6.75	9.53	1.10
2839.32	2839.48	4.57	1.61	2.41	0.63	5.78	8.75	0.40
2867.88	2868.04	2.90	1.75	2.16	0.87	3.97	7.96	0.35
2900.28	2900.44	3.84	1.84	2.45	0.67	5.55	7.27	0.24

The agglomerate velocities reduced from 12.84 to 7.27 cm/sec indicating that particle and agglomerate deposition in the channel affected the stream velocity. From Tables 3.10 and 3.11, it is observed that the agglomerates grew to a bigger size than the single particles, because agglomerates were comprised of multiple single particles. The axial ratios of the agglomerates were smaller than the single particles indicating that the agglomerates grew more in width than length when compared to the single particles. To investigate this

effect, the growth rates of the single particles and agglomerates were determined as in the 3.5 gph run. The area, length and width of single particles and agglomerates were plotted against time and regressed to obtain the corresponding growth rates. Area growth rate of single particles was found to be 2.1±0.8 mm^2/sec while that of agglomerates was 20.8±12.6 mm^2/sec. The length growth rate of single particles was 3±1.7 mm/sec while that of agglomerates was 8.3±5.2 mm/sec. The width growth rate of single particles was 0.6±0.8 mm/sec and it was 5.5± 3.4 mm/sec in agglomerates. The growth rates of single particles and agglomerates from the 3.5 gph and 6.8 gph runs are compared in Table 3.12.

Table 3.12: Comparison of single particle and agglomerate growth rates for 3.5 gph and 6.8 gph runs.

Surrogate Flow rate (gph)	Single Particle Growth Rate			Agglomerate Growth Rate		
	Area (mm^2/sec)	Length (mm/sec)	Width (mm/sec)	Area (mm^2/sec)	Length (mm/sec)	Width (mm/sec)
3.5	2.04±0.4	2.90±1.7	0.64±0.9	13.10±6.3	5.94±4.7	3.06±1.5
6.8	2.08±0.8	2.97±1.7	0.62±0.8	20.82±12.6	8.27±5.2	5.47±3.4

The single particle growth rates from the 3.5 gph and 6.8 gph runs are the same. This suggests that the particle growth rate does not depend on the surrogate flow rate. The agglomerate growth rate was greater in the 6.8 gph run when compared to the 3.5 gph run. This was because the stream velocity was higher in the 6.8 gph run causing the agglomerates to grow to a larger size prior to deposition. From Table 3.12, the growth in the length of agglomerate was 2.8 times that of single particle, while growth in width was 8.8 times. This could be compared to agglomerate length growth of 2 times over single particle and width growth of 5 times from the 3.5 gph run. In view of this, a similar approach was adopted as in the 3.5 gph run to obtain the calculated number of particles in the agglomerate. These are shown in Figure 3.13.

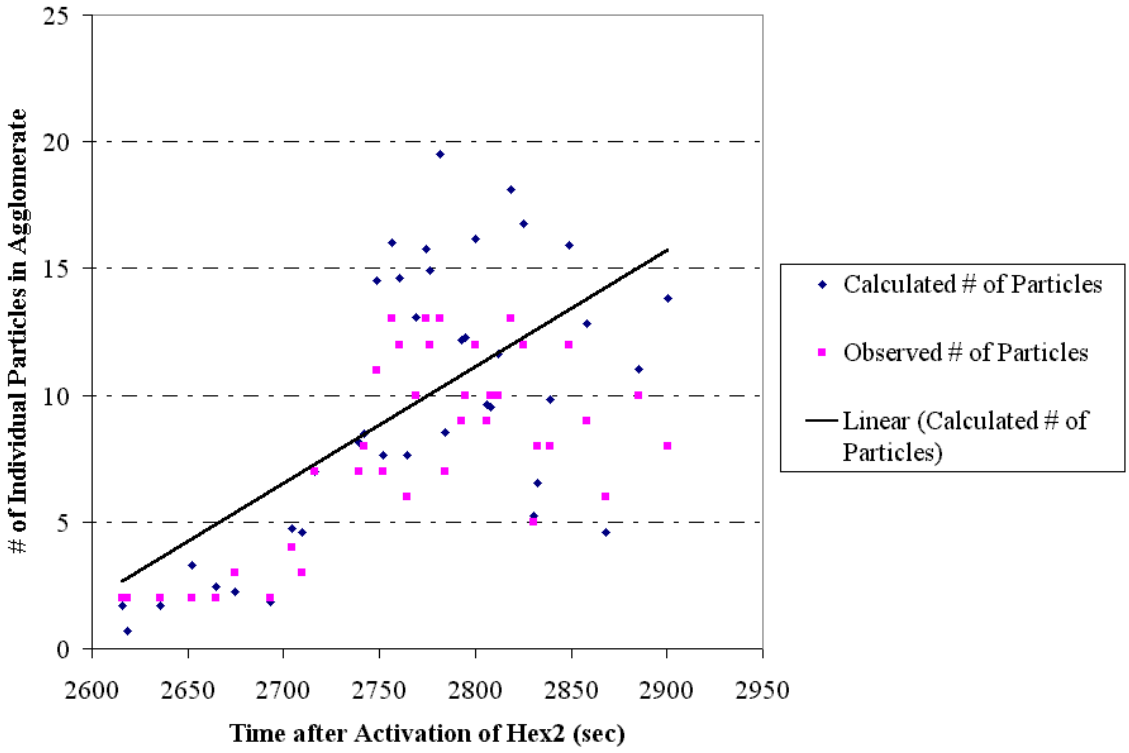

Figure 3.13: Calculated and observed # of particles comprising agglomerate.

The calculated and observed number of particles comprising the agglomerate compare well. The number of particles forming the agglomerate was less initially, so the agglomerate size and growth rate were less. The agglomerate size increased rapidly with time because the number of particles comprising the agglomerate increased. This was because the velocity of the stream decreased with time causing the agglomerate to increase in size or "pile-up" resulting in an increase in number of particles in an agglomerate.

The single particle and agglomerate growth along the pressure profile from the data acquisition system are plotted against time in Figure 3.14. The pressure reading of

transducer Pressure0 was about 1 PSIG even before 2500 seconds indicating the existence of particles, smaller than the resolution of the camera, or up or downstream,

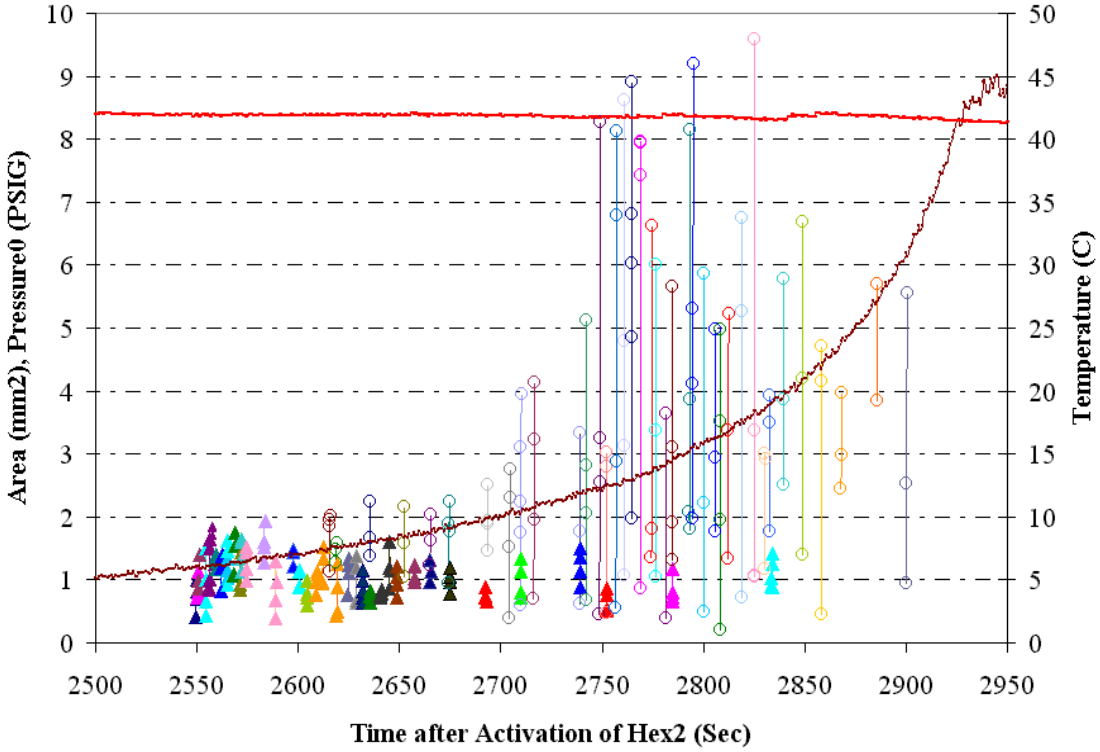

Figure 3.14: Plot of particle, agglomerate area and Pressure0 as function of time after activation of Hex2. The triangles in the plot represent the single particles while the circles represent the agglomerates. The solid brown line represents Pressure0 and solid red line represents T5.

from the measurement location. The pressure rise appeared to be gradual until about 2750 seconds, when it started to increase rapidly. This coincided with the time when agglomerate formation became predominant. The formation of the agglomerates and subsequent bed formation caused obstruction to flow resulting in the pressure rise. Single particles were first observed in the line after 2550 seconds while agglomerates started to appear after about 2680 seconds. The single particle growth was constant while the agglomerate growth rate increased with time. The last set of agglomerates was observed in the channel around 2900 seconds, when the pressure reading was about 6 psig. No

further agglomerates were observed after that time as the bed developed. Bed movement continued for about 40 seconds and then stopped. The pressure reading at that instant was a maximum of 8.9 psig, which was the pressure at the pump head. The temperature of the surrogate had reduced to about 42°C from 46°C by the time the image analysis was started. The temperature of the surrogate remained constant while the image analysis was performed indicating that the formation of particles and agglomerates did not affect the temperature. The bed fraction and pressure profiles are plotted against time to observe the effects of bed fraction on pressure rise and are shown in Figure 3.15.

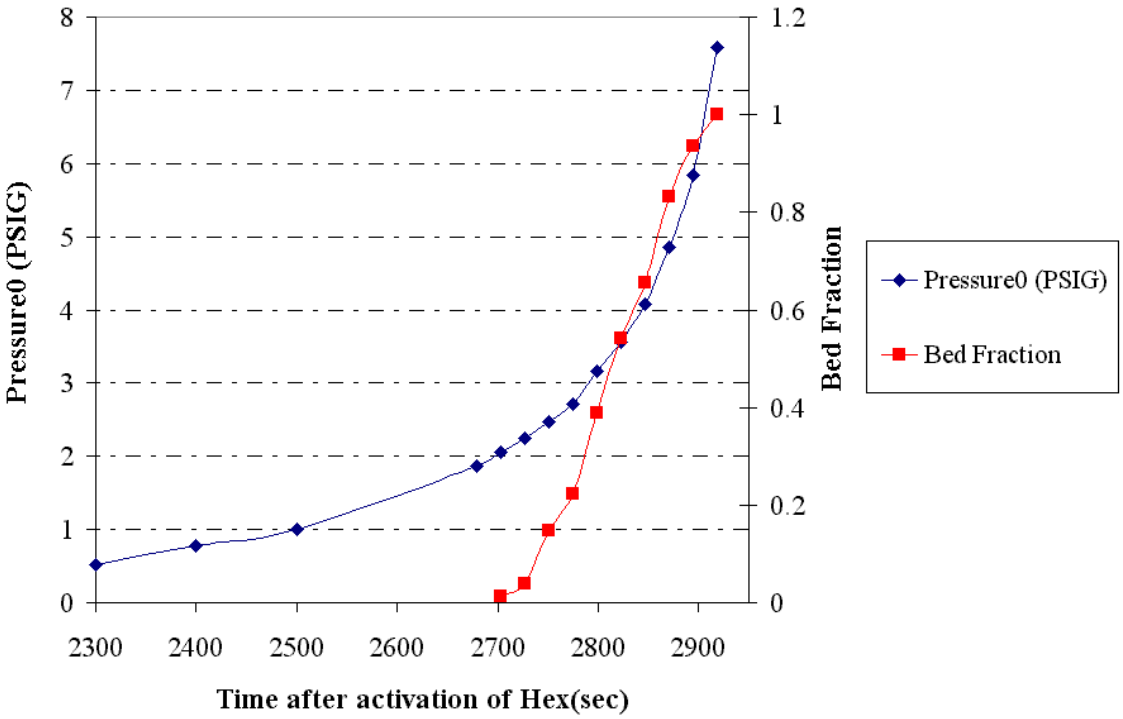

Figure 3.15: Plot of bed fraction and Pressure0 as function of time.

The bed started to form around 2700 seconds, when the pressure reading in the transducer was about 2 psig. The pressure rise was gradual until about 2750 seconds, when the bed fraction reached about 0.2. After 2750 seconds, agglomeration became prominent and the bed fraction increased rapidly resulting in a quick pressure rise. The

bed became fully developed in the channel around 2905 seconds and moved for about 35 seconds before movement ceased and plugged the line.

3.2.3 Experiments at Different Flow Rates

The results of the image analysis of 3.5 gph and 6.8 gph runs were compared to observe the effect of flow rate on plugging. The order of events leading to the plug formation started with the growth of free single particles, followed by sedimentation of single particles and agglomerates and ended with bed formation. The events were comparable in both the runs with the exception of the absence of sedimenting single particles in the 6.8 gph run. In the 6.8 gph run, the single particles were carried away by the stream and did not deposit. The single particle growth rate was about the same in both cases indicating that the particle size was unaffected by the surrogate flow rate. The single particles grew to a comparable final size in both the runs suggesting that the final size may be governed by the concentration of phosphate in the surrogate and additional experiments to investigate the effect are discussed below. The agglomerate growth rate increased with time for both the flow rates and the pressure reading was about 1 psig before the first particle was observed in the channel. The pressure profile had two distinct slopes to it in both runs, with the first gradual slope attributed to the single particles and the second steep slope attributed to the agglomerates and bed formation. In both cases, there was an initial induction time before which the particles started to form in the channel. The induction time was longer in the second case due to the slower growth rates. Based on the similarities observed in the two runs, it was concluded that the mechanism

of plug formation was the same for the two runs at different Reynolds numbers but with the same cooling rate.

From the image analysis, it was concluded that the plug formation mechanism did not vary with the flow rate though the time to plug was different. In order to investigate the time to plug in greater detail, multiple experiments were carried out at higher flow rates. Experiments were carried out at 5 gph, 5.8 gph, 8 gph and 8.5 gph apart from the 3.5 gph and 6.8 gph experiments done before. The Reynolds numbers corresponding to the above flow rates are 223, 319, 370, 436, 510 and 542 respectively. The experiments were carried out as before and Hex2 was turned on at 1.2gpm when the temperature of surrogate at T5 reached about 46^{o}C. The pressure profiles from the different runs were plotted together against time and are shown in Figure 3.16.

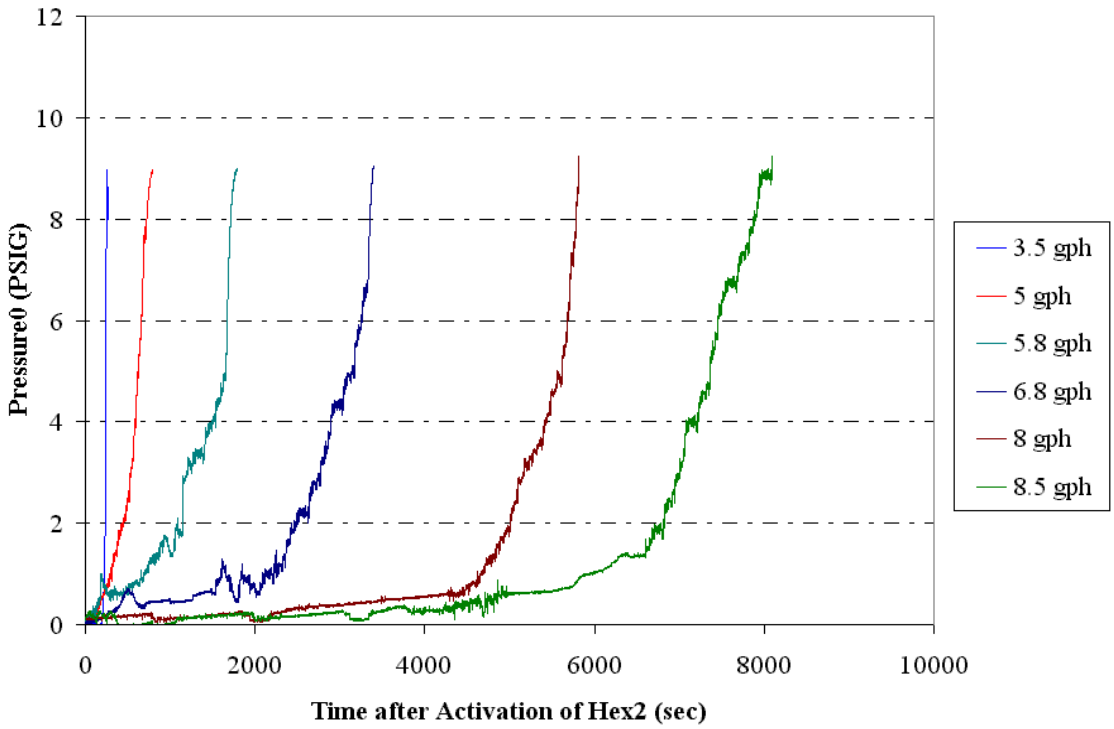

Figure 3.16: Pressure profiles from experiments at varying flow rates plotted against time.

It is observed from the plots that the experiment at 3.5 gph plugged in the shortest time of about 258 seconds. The run at 8.5 gph took the longest time, about 8000 seconds, to plug. The characteristics of the above runs are collected in Table 3.13.

Table 3.13: Characteristics of experiments at varying Reynolds numbers.

Surrogate Flow Rate (gph)	Reynolds Number (Re)	Time to Plug (sec)
3.5	223	258
5	319	760
5.8	370	1786
6.8	436	3397
8	510	5810
8.5	542	8102

The pressure profiles from the different experiments exhibited the same behavior. All of them illustrated an exponential rise in pressure after an initial "induction" period. This observation was comparable with the image analysis results presented above (Chapter 3.2.1 and 3.2.2). Here, the formation of single particle was a function of the surrogate flow rate. At higher flow rates, single particle and agglomerate formation were delayed resulting in a delayed pressure rise and a longer time to plug.

Each of the pressure profiles had two distinct slopes, the initial gradual slope corresponding to the induction period during which the particles began to form in the line and a steep slope which corresponded to the agglomerate formation and bed growth. In order to obtain an estimate of the time taken for the line to plug at higher flow rates, the data from the different runs were regressed and extrapolated. Surrogate flow rates were plotted against the time to plug from Table 3.14 in Figure 3.17. The time to plug increased exponentially with the surrogate flow rate (or the initial surrogate velocity).

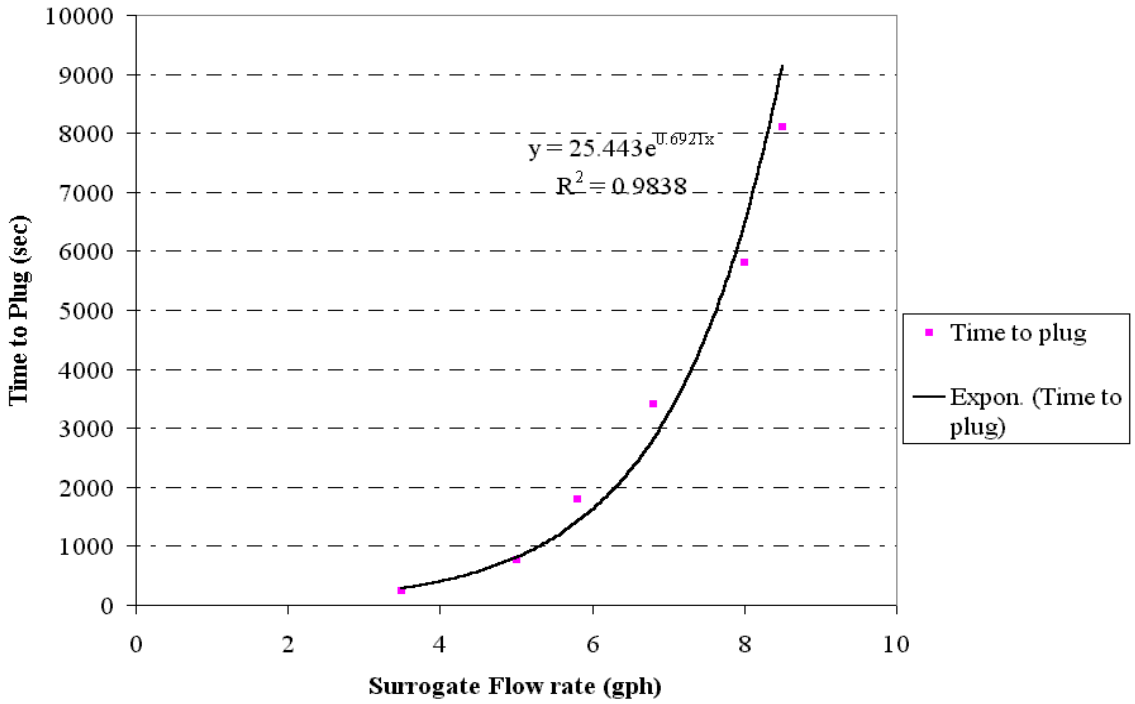

Figure 3.17: Plot showing time to plug against surrogate flow rate.

3.2.4 Experiments at Different Cooling Rates

In order to investigate the effects of cooling rate on plugging, experiments were carried out at the surrogate flow rate of 6.8 gph and cooling rates of 0.7 gpm, 0.6 gpm and 0.4 gpm apart from the 1.2 gpm experiments done previously. The imaging system was used in an experiment with a cooling water flow rate of 0.4 gpm to observe the effect of cooling rate on growth rates. The results are given in Table 3.14 and plotted along with the pressure and temperature profiles in Figure 3.18.

Table 3.14: Characteristics of experiments at varying cooling water rates.

Cooling Water Flow Rate (gpm)	Temperature at Plug (^{o}C)	Time to plug (sec)
1.2	41.62	2950
0.7	41.58	3359
0.6	41.97	3613
0.4	42.6	4207

The results indicated that the plugging temperature increased with decreasing cooling rate. At the higher cooling rates, the cooling fluid extracted more energy out of the surrogate and thus, resulted in a lower temperature of the surrogate. There was an increasing trend in plugging temperature with the exception of the experimental run at a

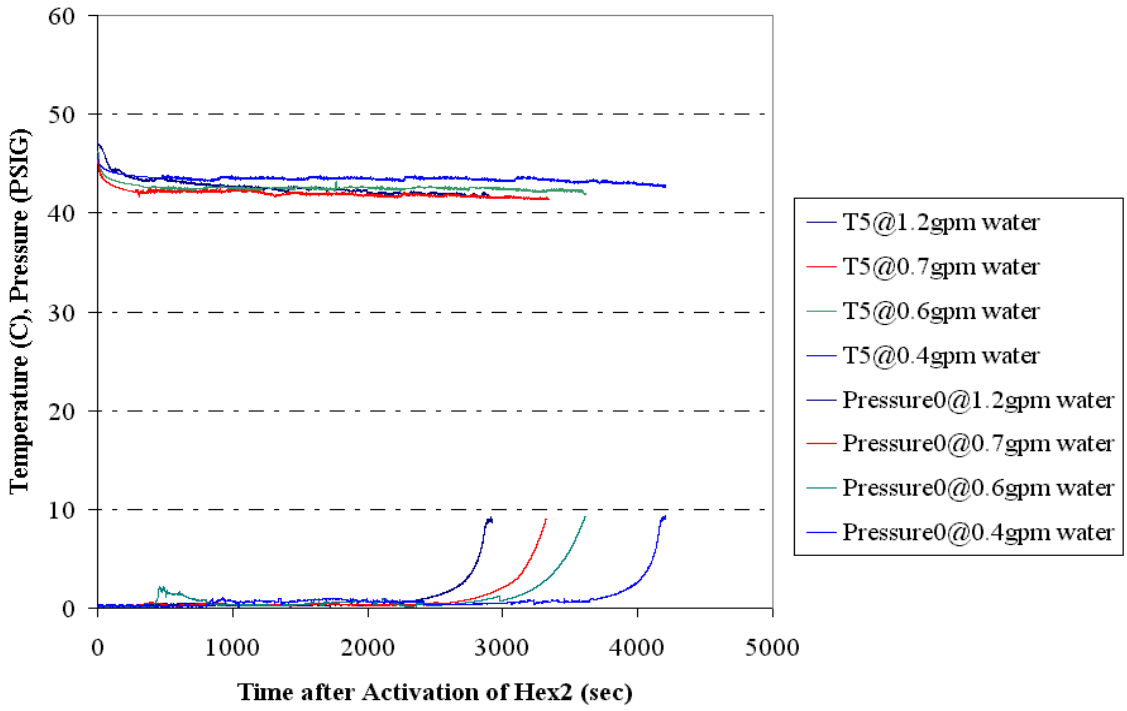

Figure 3.18: Temperature and pressure profiles from plugging experiments at different cooling rates.

cooling rate of 1.2gpm. The deviation was due to the slightly higher temperature (47.1^{o}C) at which Hex2 was turned on. The plugging time also increased with decreasing cooling rate. This was expected since, upon reducing the cooling rate, more time was required to attain a given temperature. A longer induction time, which increased the time to plug, was the practical result. The cooling rates are plotted against time in Figure 3.19. From the data in Figures 3.18 and 3.19, the time to plug increased with decreasing flow rate. The best fit for the experimental data was obtained using a logarithmic fit. This result was

complimentary to the plot of surrogate flow rate against time to plug in Figure 3.17, which gave an exponential curve fit.

The experiment with the imaging system showed that the overall plugging mechanism did not vary with the cooling rate. The area growth rate of the single particles was obtained as 1.5±0.7 mm^2/sec, while the length growth rate was 1.5±0.8 mm/sec and

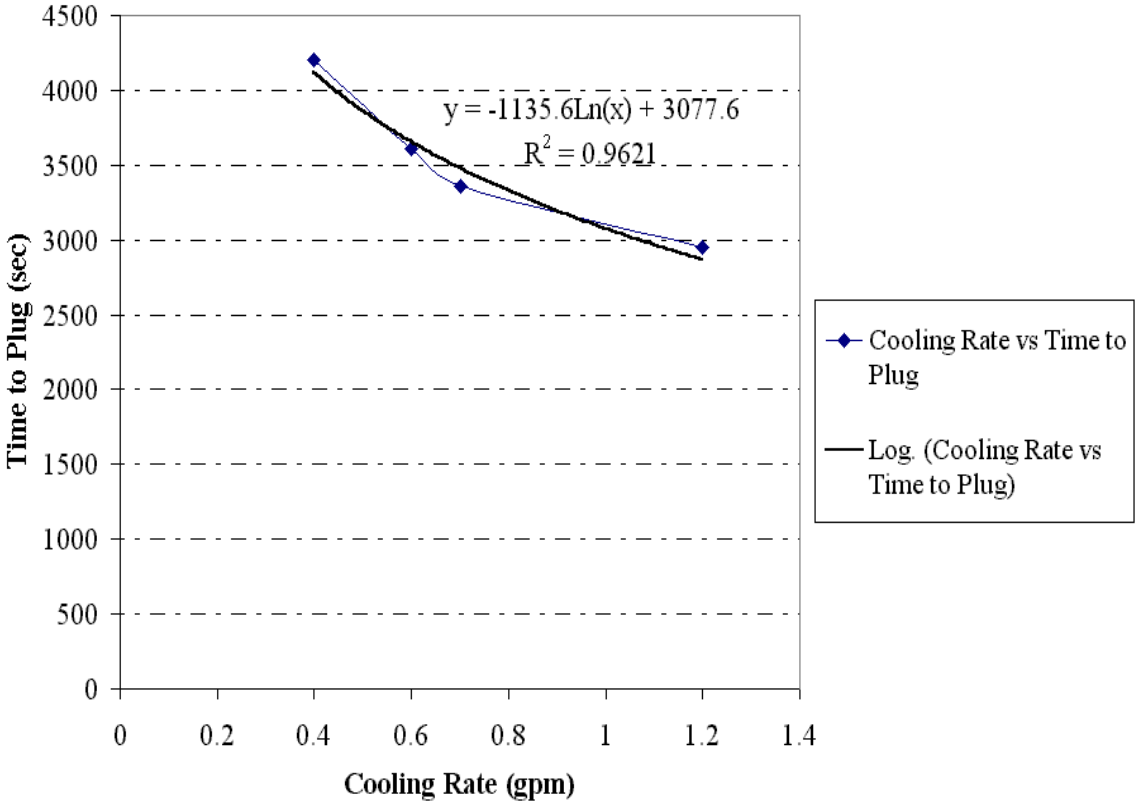

Figure 3.19: Plot of cooling rate against time to plug.

width growth rate was 0.5±0.3 mm/sec. The area growth rate of agglomerates was 18.6±9.4 mm^2/sec, length growth rate was 6.7±3.7 mm/sec and width growth rate was 5.3±2.6 mm/sec. This indicated that the growth rates decreased with cooling rates. The lower cooling rates caused the surrogate to cool slowly, resulting in lower growth rates.

3.2.5 Experiments at Different $Na_3PO_4 \cdot 12H_2O \cdot 0.25NaOH$ Concentrations

Experiments were done with the surrogate obtained by reducing the $Na_3PO_4 \cdot 0.25NaOH \cdot 12H_2O$ concentration to 0.2 moles and 0.15 moles in the actual recipe, while leaving the other constituents unaltered. The purpose of the experiments was to determine the effect of phosphate concentration on the time to form a plug and particle and agglomerate growth rates. In the experiment with 0.2 moles concentration of $Na_3PO_4 \cdot 0.25NaOH \cdot 12H_2O$, Hex2 was used with cooling water flow rate of 3 gpm. The time to plug was 3715 seconds and the temperature at plug was 35.9^oC. At lower phosphate concentrations, the phosphate crystals form at a lower temperature resulting in a lower plugging temperature. The images from the imaging system showed that the plugging mechanism was the same as before. The area growth of single particle was calculated as 1.4±0.6 mm^2/sec, length growth was 1.4± 0.8 mm/sec and width growth was 0.5± 0.3 mm/sec. The growth rate in area of agglomerate was 15.4± 7.2 mm^2/sec, length was 6.2± 2.6 mm/sec and width was 5± 2.6 mm/sec. The reduced availability of phosphate in the surrogate at lower phosphate concentrations causes the particles to grow slower.

Heat exchangers Hex1 and Hex2 were used in the experiment with 0.15 moles $Na_3PO_4 \cdot 0.25NaOH \cdot 12H_2O$ to reduce the temperature of the surrogate. The channel plugged after 2530 seconds and the temperature at the plug was 33.4^oC. As two heat exchangers were used in the experiment, the plug formed inside Hex2 and as a result image analysis could not be performed.

3.3 Unplugging Experiments

3.3.1 Experiments to Determine Time to Unplug the Line

Unplugging experiments (Chapter 2.4) were carried out using water after each experimental run to unplug the line of the $Na_3PO_4 \cdot 0.25NaOH \cdot 12H_2O$ plug. Temperature and pressure profiles from a typical unplugging experiment are shown in Figure 3.20.

The experiment under consideration was carried out after the line plugged from an experiment at 6.8 gph. The 6ft plug was left in the line for ≈ 24 hours before being unplugged. The water used in unplugging was stored in Tank3 at a temperature of 50°C. The water flow rate used for unplugging was set at 10gph, which corresponded to the

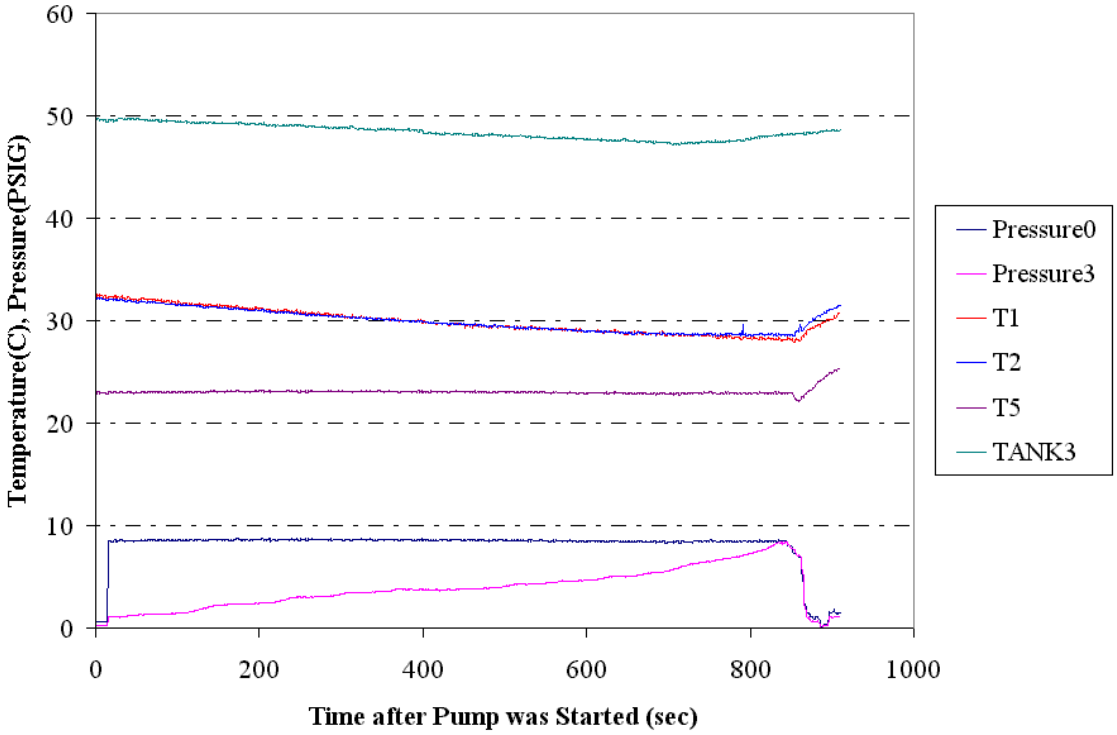

Figure 3.20: Temperature and pressure profiles from unplugging experiment.

available pump head. Thermocouples T1 and T2 were located upstream, while T5 was located downstream of the plug section. Initially, when the pump was started, the transducer upstream of the plug showed a maximum, corresponding to the pump head,

while the downstream transducer showed a reading of 0 PSIG because of the plug in the line. Later, as time progressed, the downstream pressure began to rise indicating that water was percolating through the plug. At the start of the experiment, water that had percolated through the plug section slowly dripped out at the end of the test loop. The slow drip gradually transformed into a flow at the end of the experiment when the line was unplugged. This compared well to the pressure profiles obtained from the acquisition system that indicated a gradual pressure rise until about 600 seconds and a quick rise towards the end of the experiment. The line was unplugged about 900 seconds after the pump was started. Though water was stored in the tank at 50^{o}C, the temperature upstream of the plug gradually decreased to about 28^{o}C before the line was unplugged. This was due to conduction losses in the absence of any significant flow. The temperature of the section downstream of the plug remained around 22.5^{o}C (room temperature) until the line was unplugged. After the line was unplugged, the temperatures of T1, T2 and T5 rose to the temperatures they would exhibit if hot water from Tank1 flowed in the channel. The variation in Tank3 was due to the cycling of the immersion heater in the tank.

In order to observe the unplugging experiments in greater detail, the color video camera was used. A video of the process is given in Appendix E (Figure E.2). Initial experiments were done with water, while later experiments were done with water mixed with green food dye. The purpose of the food dye was to provide a better color contrast to help identify the exact location to which the water had percolated. A tape measure was placed on top of the clear plastic section to obtain the rate at which water percolated through the plug. Images from the video camera are shown in Figure 3.21.

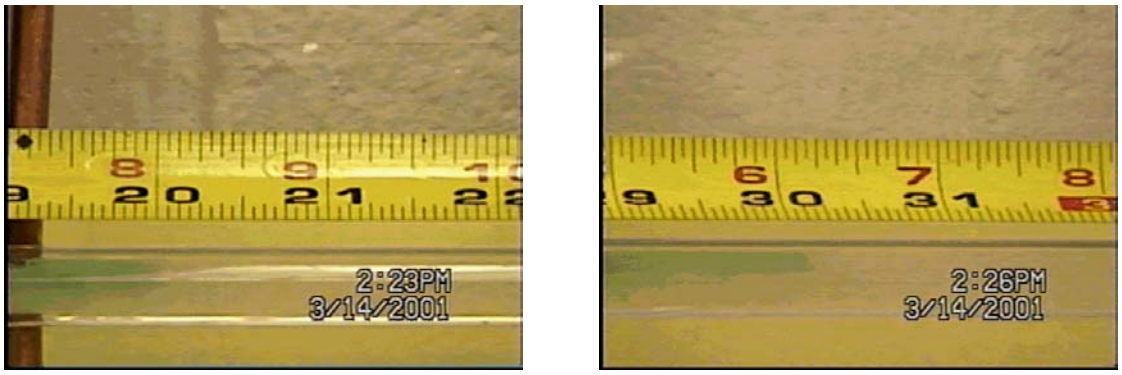

Figure 3.21: Images of unplugging experiments from video camera using water mixed with food dye.

Images from Figure 3.21 indicate that water percolated from the 20” section to 30” section in 3 minutes. From the video, it is observed that unplugging occurred in different phases. Initially, water percolated through the plug section and dripped at the end of the clear section. The location to which water percolated could be identified using the tape measure. Due to water percolation, the plug material gradually weakened into a soggy gel. The soggy gel then began to dissolve, in some parts, due to continued percolation. This led to a gradual increase in the rate of water percolation, which carried away the dissolved material. Finally, the whole structure broke up and was carried away by water. The line was then unplugged, which corresponded to the transformation of water drip into flow. The rate of water percolation was obtained from the experiments and is shown in Figure 3.22.

The distance to which water percolated increased exponentially with time. This indicated that water percolated faster at the end of the plug section than at the beginning. This is attributed to the fact that the plug partially dissolved as water percolated. The less dense gel was then more amenable to percolation. An unplugging experiment was done in which the pump was turned off after water mixed with food dye had percolated to the end

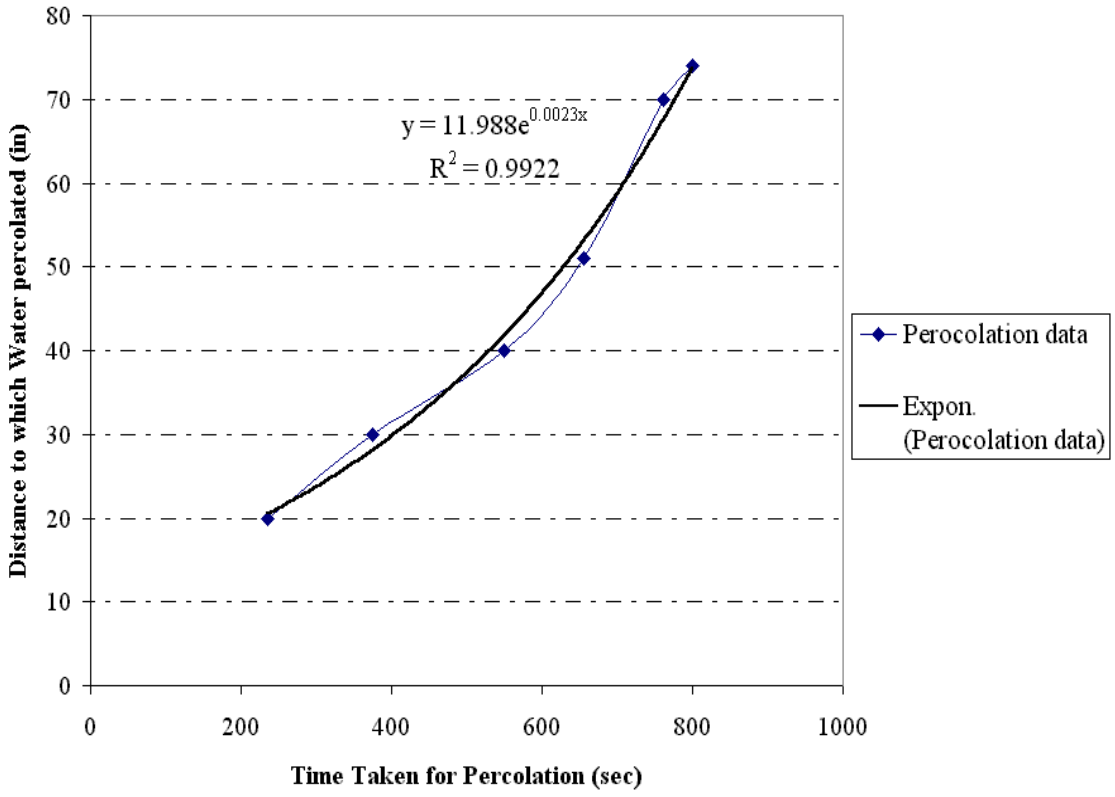

Figure 3.22: Rate of water percolation from unplugging experiments.

of the plug section and before the plug material began to dissolve. The plug material was then extruded and sectioned. The sections were green colored, indicating that water had percolated through the plug.

Unplugging experiments were done after the lines were plugged at different flow rates. The time to unplug did not vary with the plugging flow rate. This was attributed to the plugging mechanisms, which were identical to those discussed previously. Further experiments were done to observe the effect of pressure at the pump head and the plug residence time.

3.3.2 Experiments at Varying Pressure Heads at Pump

The experiments were done by adjusting the surrogate flow meter (RMS) to different water flow rates, which corresponded to different pump pressure heads. The results from the experiments are presented in Figure 3.23.

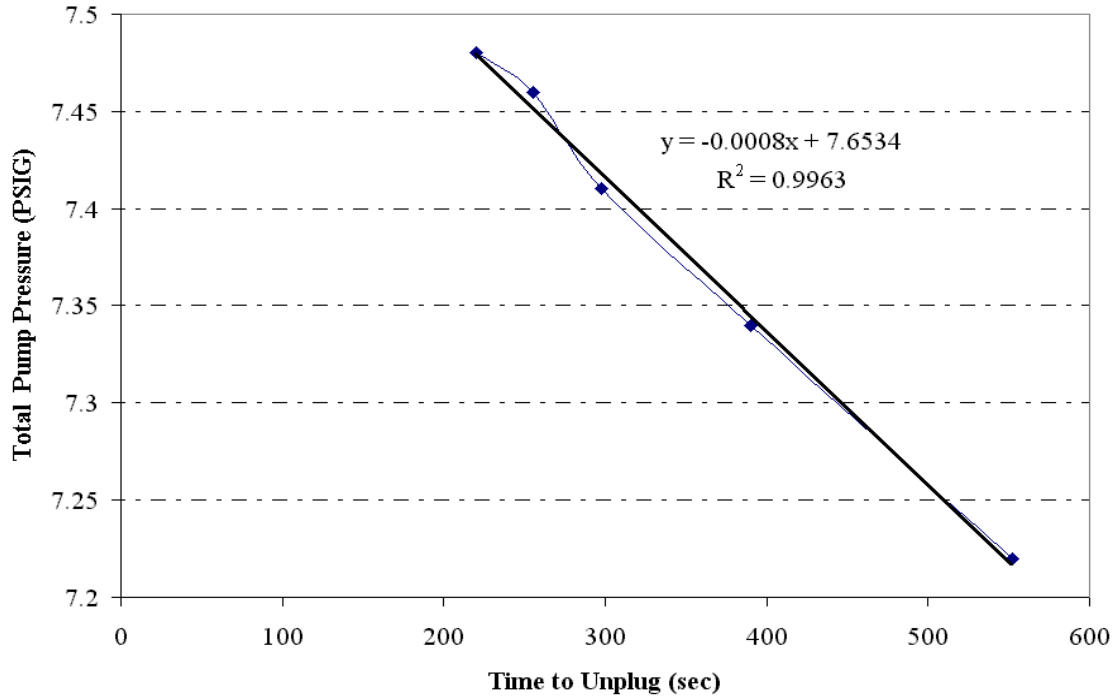

Figure 3.23: Time to unplug plotted against total pump pressure exerted.

The time to unplug decreased with increasing pump pressures. Higher pump pressures would exert more pressure on the plug material resulting in more rapid percolation.

3.3.3 Experiments at Varying Residence Times of Plug in Line

Unplugging experiments were done by varying the residence time of the plug in the line. The experiments were done at residence times 2, 6, 12, 24 and 48 hrs of after formation of the initial plug. The results from the experiments are shown in Figure 3.24.

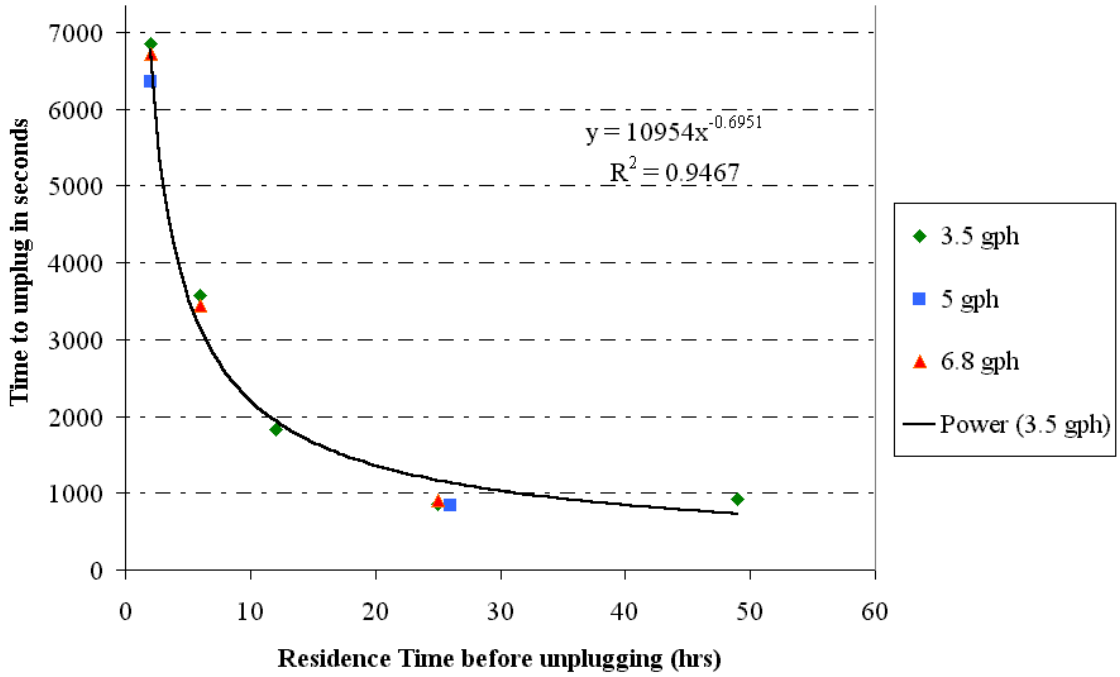

Figure 3.24: Time to unplug plotted against residence time before unplugging.

It was observed, from the experimental results, that the time to unplug decreased with an increase in plug residence time until 24 hrs and then remained constant. Experiments were performed after plugging the line at flow rates of 3.5, 5 and 6.8 gph. The time to unplug decreased with the residence time of the plug in the channel. This behavior is expected to be due to Ostwald ripening of the plug material, which is characterized by the growth of the larger crystals at the expense of the smaller crystals. As the phosphate crystals grow larger with time, the interstitial spaces between the crystals increase. This allows easier access of water to the plug material causing the channel to unplug faster. Future experiments to investigate the effect of residence time on unplugging are planned.

CHAPTER IV

DISCUSSION

4.1 Introduction

The image analysis results discussed previously (Chapter 3.2) indicated that the pipeline plugging was characterized by the events discussed below. The decrease in temperature of the surrogate caused particles to form in the channel. The particles grew to a particular size and deposited. Finally the single particles and agglomerates formed a bed, which gradually increased causing a pressure rise and plugged the line. Models for these events were developed and are discussed in this section.

4.2 Models for Critical Parameters

4.2.1 Model for Critical Velocity

Several models are available in the literature to determine the critical velocity of particles in solid-liquid two-phase flow as discussed previously (Chapter 1.2.2). Most of the models required particle size distribution while others required the evaluation of constants to obtain the critical settling velocity. A model developed by Durand was used to obtain critical velocity owing to the ease in its usage and data requirements. The model enabled the calculation of the critical particle size corresponding to a set stream velocity, which could be compared to the experimental value. Particles with sizes greater than the critical particle size would deposit in the channel, while the particles with lower sizes are carried away by the flow.

The stream velocity was taken as the free single particle velocity, while the characteristic length was taken as the width of the particle (since it was normal to the direction of flow). The density of solid particles was taken as that of $Na_3PO_4 \cdot 0.25NaOH \cdot 12H_2O$ and surrogate density was obtained from ESP calculations (Chapter 2.3.1).

The image analysis of the 3.5 gph surrogate run discussed previously (Chapter 3.2) was used to obtain the critical sizes. The critical sizes calculated from the Durand equation are compared to experimental particle sizes in Table 4.1. The other entries in the table include the start and end time for image analysis of each set, area and velocity of the single particle observed in the last frame in each set.

Table 4.1: Comparison of experimental and calculated critical particle sizes.

Set Number	Start Time (sec)	End Time (sec)	Area (mm^2)	Vx (cm/sec)	Width=L_{exp} (mm)	Width=L_{cal} (mm)
1	196.24	196.56	0.82	7.96	0.47	0.58
2	202.08	203.32	1.10	7.92	0.51	0.58
3	208.72	208.96	0.95	7.42	0.58	0.54
4	209.60	209.92	0.47	6.77	0.31	0.50
5	212.56	212.80	0.98	6.96	0.56	0.51
6	214.96	215.28	1.05	6.48	0.62	0.47
7	217.92	218.40	1.53	6.27	0.56	0.46
8	218.96	219.28	1.16	6.21	0.45	0.45

The calculated critical sizes are comparable to the experimental critical sizes in most cases. Some exceptions in sets 5, 6 and 7 were when the bed formation was predominant. In these cases, because the bed velocity was lower than the stream velocity, the particle sizes increased before they deposited. The calculated critical velocities indicated that particles with larger dimensions that formed in the channel would deposit in the channel. This compared well to the agglomerates (Chapter 3.2), which were much bigger in size than the critical dimensions and thus deposited in the channel.

A single sedimenting particle was observed during image analysis, which had exceeded the critical particle size and thus deposited. The particle had a width of 0.47 mm when first observed and grew to a final width of 0.64 mm. The velocity of the particle correspondingly decreased from 8.11 cm/sec to 7.42 cm/sec. The particle was observed about 195 seconds after the activation of Hex2, when the bed did not form. The calculated critical particle size at that time was 0.58 mm, which was smaller than the actual particle size resulting in particle deposition. It should be noted that the particle sizes were relative to the location where image analysis was performed and that all the particles would eventually exceed the critical particle and deposit.

Similar calculations were performed to determine critical particle sizes in the 6.8 gph run and typical results are shown in Table 4.2.

Table 4.2: Comparison of experimental and calculated critical particle sizes.

Set Number	Start Time (sec)	End Time (sec)	Area (mm^2)	Vx (cm/sec)	Width=L_{exp} (mm)	Width=L_{cal} (mm)
1	2549.56	2549.80	1.01	0.59	15.21	1.11
2	2557.40	2557.64	1.83	0.72	14.85	1.09
3	2571.56	2571.80	1.64	0.76	14.79	1.08
4	2611.88	2612.12	1.51	0.72	13.90	1.02
5	2644.92	2645.16	1.16	0.50	13.68	1.00
6	2709.72	2709.96	1.14	0.49	12.45	0.91
7	2739.08	2739.32	1.50	0.70	12.33	0.90
8	2751.96	2752.20	0.87	0.51	11.68	0.86
9	2784.52	2784.76	1.17	0.71	10.99	0.81
10	2833.48	2833.80	1.26	0.57	10.39	0.76

The calculated single particle sizes were greater than the experimental sizes in the 6.8gph run indicating that none of the single particles would sediment. This compared well to the image analysis results, during which no sedimenting single particles were observed. The agglomerates observed during image analysis had greater dimensions than the critical

sizes and thus deposited. The calculated critical particle sizes and experimental critical particle sizes from Tables 4.1 and 4.2 were plotted against the stream velocities and are shown in Figure 4.1.

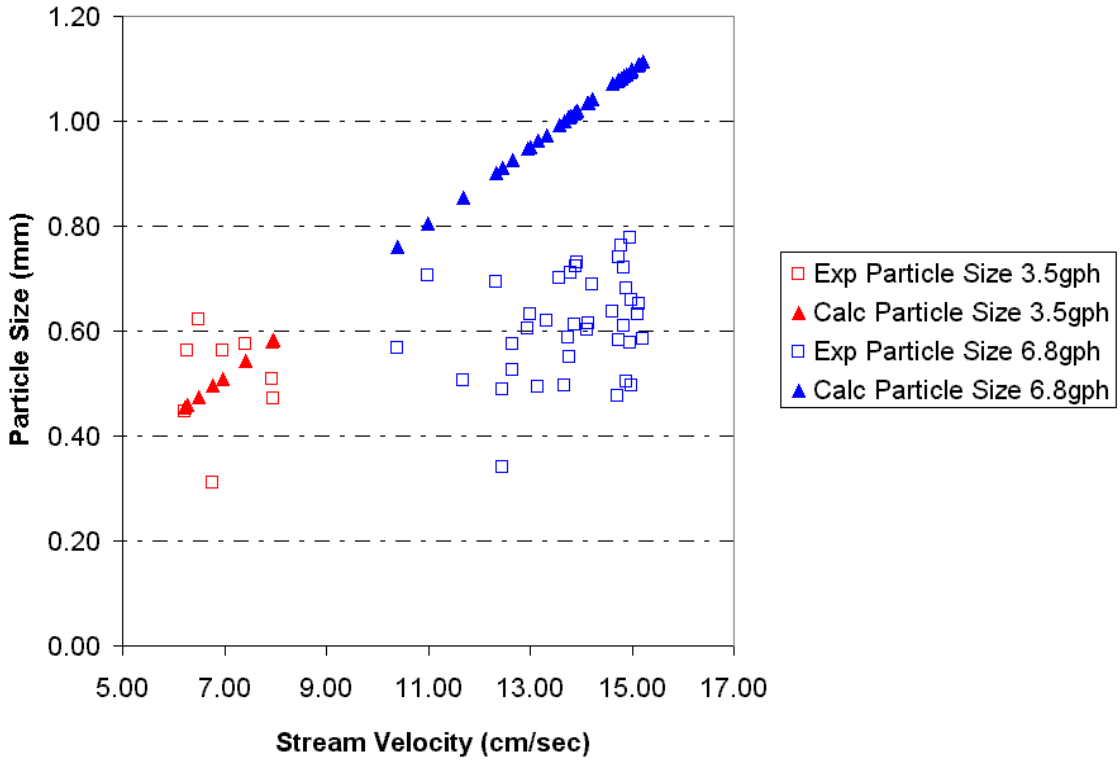

Figure 4.1: Comparison of calculated and experimental critical particle sizes from 3.5gph and 6.8gph image analysis experiments.

The calculated single particle sizes were greater than the experimental sizes in the 6.8 gph run indicating that none of the single particles would deposit. This compared well to the image analysis results, during which no sedimenting single particles were observed. The agglomerates observed during image analysis had greater dimensions than the critical sizes and thus deposited. The calculated critical particle sizes and experimental critical particle sizes from Tables 4.1 and 4.2 were plotted against the stream velocities and are shown in Figure 4.1.

4.2.2 Model for Temperature Drop of Surrogate

The temperature profiles of surrogate from Figures 3.1 and 3.10 indicated that the downstream temperatures decreased rapidly after the activation of the heat exchanger. A gradual temperature drop then followed before a constant temperature was attained that varied with the surrogate flow rate. At a higher flow rate, the cooling water extracted less energy out of the system resulting in a higher final temperature. Similarly at a lower surrogate flow rate, a lower surrogate temperature resulted from the same cooling rate as before.

The effect of particle formation on temperature drop of the surrogate was examined to obtain the right model. During the image analysis of surrogate at 3.5 gph, the first particle was observed in the channel about 190 seconds after the activation of Hex2. At 6.8gph, the first particle was observed about 2550 seconds after the activation of Hex2. The plug occurred in the 3.5 gph run after 230 seconds, while it occurred after 2930 seconds in the 6.8 gph run. To analyze both the experiments on the same scale, normalized time (ratio of actual time to time to plug) was used. On the normalized scale, Hex2 was turned on when time was 0 and final temperature reached when time was 1. The first particle formed in the 3.5 gph run when the normalized time was 0.85. Similarly, in the 6.8 gph run the first particle formed at a normalized time of 0.87. This indicated that the heat transfer was convection driven until about 85% of the total run time after Hex2 was activated. Further, the temperature of the surrogate did not exhibit any significant variations after the particles started to form in the channel. The single particles and agglomerates, which deposited in the channel, formed a bed that was in motion until the line eventually plugged. This implied that the plugging process was

mainly convection driven, with negligible conduction effect due to particle formation. The analogy reduces the temperature drop of the surrogate during the plugging process to that of an unsteady state convection problem.

Several models are available in the literature for the unsteady state convection problems as discussed previously (Chapter 1.2.4). The model developed by Krishan was used to compare with the experimental temperature profiles. The model deals with unsteady heat transfer to a fully developed flow in a heat-conducting pipe of finite thickness when the outer periphery of pipe undergoes a step change in heat flux or surface temperature. Since the cooling water temperature profiles from Figures 3.1 and 3.10 remained constant after Hex2 was activated, the solution of Krishan for step change in heat flux was used to obtain the calculated temperature profiles.

Temperature distribution equations were applied to the surrogate and pipe wall and using boundary conditions at the surrogate-pipe interface, the equations were combined. The equations were solved by the use of Laplace transforms, which were later inverted to obtain series solutions for the temperature distributions. The resulting distributions were applicable only for small periods of time because of the series solution. The temperature distributions were obtained for different surrogate and cooling water flow rates. The model failed in some cases when the time to plug was greater than 2000 seconds. In such cases, the temperature distributions were extrapolated over the remaining time. The experimental and calculated temperature profiles for the experiments are shown in Figure 4.2.

The calculated temperature profiles were best described by an equation of the form $y=a\cdot\ln(x)+b$, where y is the temperature, x is the normalized time and a, b are

constants. The experimental profiles were then fitted using a logarithmic equation and compared to the calculated values. The experimental and calculated values for slope, intercept and r^2, are given in Table 4.3 and 4.4.

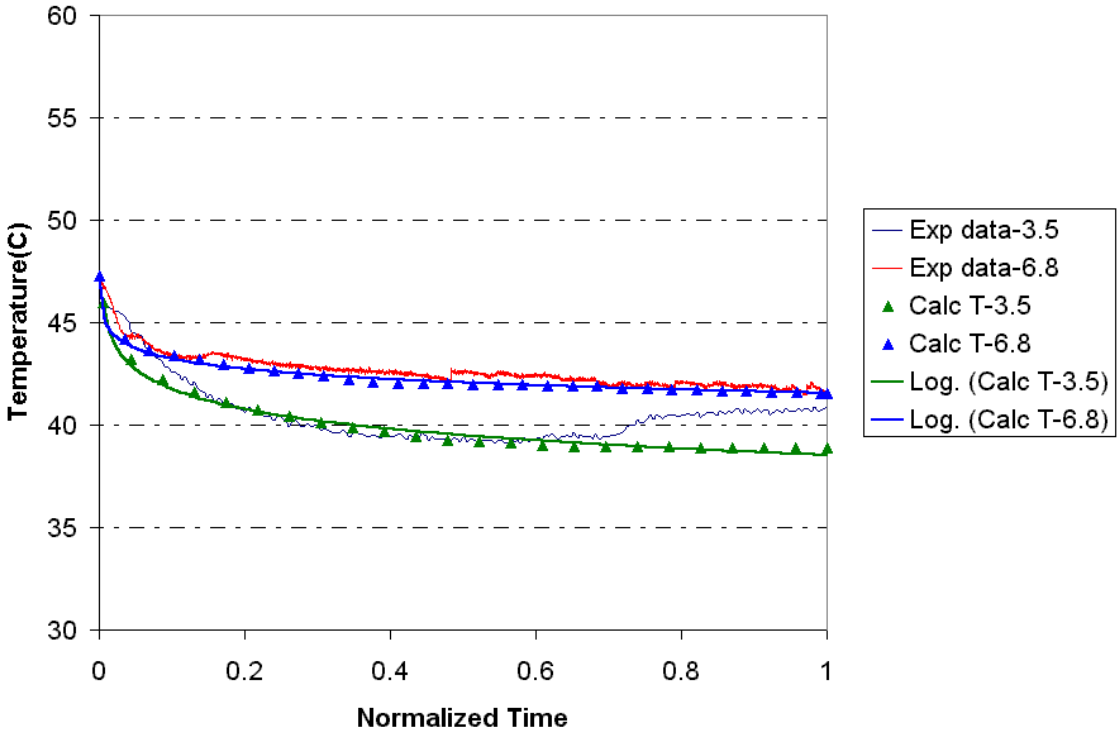

Figure 4.2: Comparison of experimental and calculated downstream temperatures for surrogate experiments at 3.5 gph and 6.8 gph.

Table 4.3: Comparison of experimental and calculated values for experiments at varying surrogate flow rates.

	Experimental			Calculated		
Flow rate(gph)	Slope	Intercept	R^2	Slope	Intercept	R^2
3.5	-1.27	39.29	0.64	-1.41	39.53	0.99
5	-1.16	40.43	0.92	-0.83	40.90	0.98
6.8	-0.85	41.80	0.96	-0.74	41.56	0.99

Table 4.4: Comparison of experimental and calculated values for experiments at varying cooling water flow rates.

	Experimental			Calculated		
Flow rate(gph)	Slope	Intercept	R^2	Slope	Intercept	R^2

Table 4.4: Comparison of experimental and calculated values for experiments at varying cooling water flow rates - continued.

1.2	-0.85	41.80	0.96	-0.74	41.56	0.99
0.7	-0.37	41.61	0.83	-0.46	41.32	0.94
0.6	-0.28	42.28	0.65	-0.38	42.06	0.98
0.4	-0.24	43.21	0.65	-0.26	43.03	0.94

The intercept or the plugging temperature increased with the surrogate flow rate. This was attributed to better heat transfer at higher flow rates. Similarly, the slope decreased with cooling rate because higher cooling rates extracted more energy out of the surrogate and vice-versa. The low correlation value in the 3.5 gph was attributed to the slight increase in temperature at the end of the experiment, which was uncommon, as discussed previously (Chapter 3.2). Similarly, the low correlation values in the experiments at varying cooling rates are attributed to the variation in tank temperature, which became prominent due to the longer plugging time. Overall, the slope and intercept of the experimental and calculated profiles compare well indicating that the model of Krishan adequately describes the observed temperature distributions and analogy of unsteady state convection.

4.2.3 Model for Pressure Rise in Channel

The pressure profiles in Figures 3.1 and 3.10 showed that the pressure upstream of the heat exchanger began to increase with the occurrence of particles in the channel. This indicated that the pressure rise was dependent on the amount of solids precipitating out of the surrogate. Further, Figures 3.9 and 3.15 showed that the rapid pressure rise of the transducer corresponded to the bed formation and development. Based on the

experimental observations, a two-layer model developed by Wilson was used to compare with experimental results (Chapter 1.2.3).

The model assumed the flow to be characterized by a bed, comprised of dense solids, flowing at the bottom and liquid at the top. Conservation equation for mass and momentum were applied to each layer and solved to obtain the pressure profile. It was assumed that the solid and liquid layers shared a common pressure. Though the model provided equations for mass and momentum transfer between the layers, their scope was limited to modeling the experimental pressure rise in the channel.

The critical parameters required by the model were obtained from image analysis. The average bed height was obtained by dividing the bed area with bed length obtained from image analysis. The bed and stream velocities were also obtained from image analysis. The increase in bed area caused a corresponding rise in pressure. The calculated and experimental pressure profiles are shown in Figure 4.3.

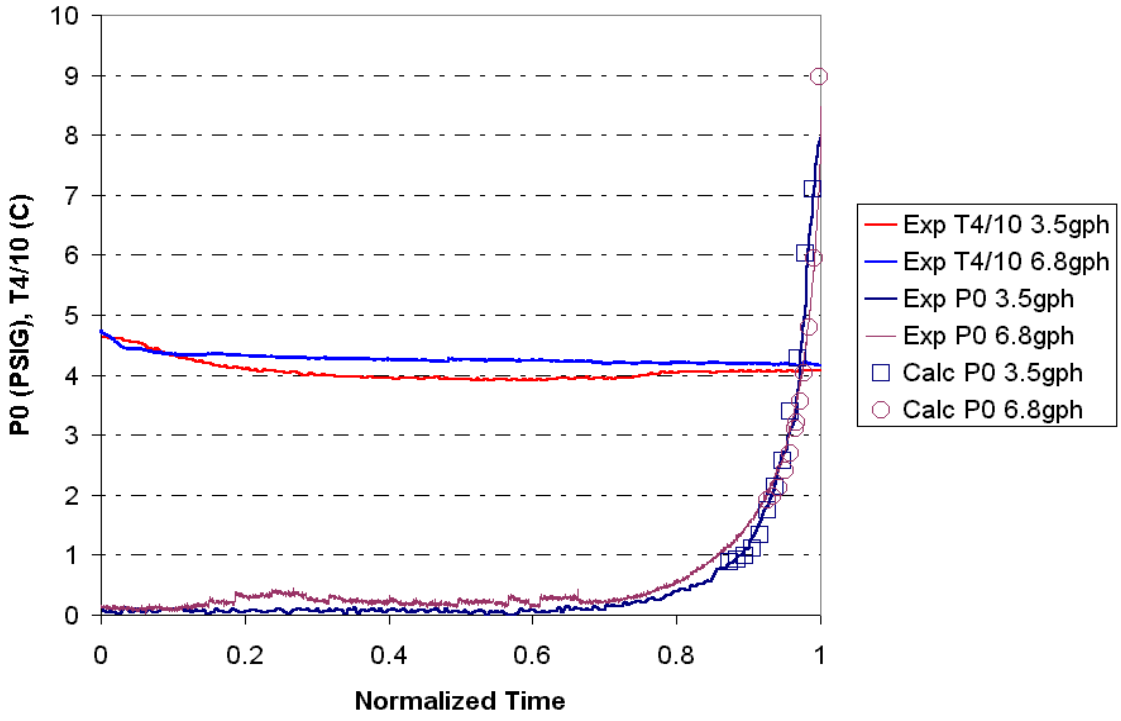

Figure 4.3: Comparison of experimental and calculated pressure profiles for experiments at 3.5 gph and 6.8 gph. Corresponding temperature profiles are also shown.

The mass and momentum transfer equations used by the model compared well to the experimental observations such as the liquid (stream) velocity decreasing with the solids (bed) formation and vice-versa. The pressure profiles from the model showed good (bed) with the experimental data.

4.3. Development of Operating Envelope for Saltwell Pumping Experiments

Saltwell pumping experiments were carried out at varying surrogate flow rates, cooling rates and at different surrogate concentrations. The purpose of the experiments was to identify the effect of the variables on the plugging mechanism, temperature and time. The results from the individual experiments are consolidated to develop an operating envelope for saltwell pumping operations.

The plugging temperature is the primary parameter in developing the operating envelope, which is plotted against the experimental variables. To develop a simple two-dimensional plot, the different experimental variables are combined into a single variable, which is plotted against plugging temperature. The surrogate flow rate is combined with the $Na_3PO_4 \cdot 0.25NaOH \cdot 12H_2O$ molar concentration to obtain molar flow rate of $Na_3PO_4 \cdot 0.25NaOH \cdot 12H_2O$. Different cooling rates were applied to the surrogate causing a variation in the plugging temperature. By neglecting the heat losses, the energy gained by cooling water is approximated as energy lost by the surrogate. Thus, the heat flux is used to account for the variation in cooling rates and was calculated using:

$$q = m_S \cdot C_{ps} \cdot (T_{si} - T_{sp}) = Q_S \cdot \rho_S \cdot C_{ps} \cdot (T_{si} - T_{sp}) \qquad (4\text{-}1)$$

where m_s is the mass flow rate of surrogate, C_{ps} is the specific heat of surrogate, T_{si} is the temperature of surrogate when heat exchanger is activated, T_{sp} is surrogate plugging temperature, Q_s is volumetric flow rate of surrogate and ρ_s is density of surrogate.

Finally, the heat flux is divided by the molar flow rate of surrogate to combine them into a single variable, encompassing all the experimental variables. The resulting ratio has the units of W·hr/mole and is the product of specific heat of the surrogate, average molecular weight of surrogate and temperature drop of surrogate resulting in a plug. Thus the plot of ratio of heat flux and molar flow rate against temperature at plug is expected to be a straight line as shown in Figure 4.4.

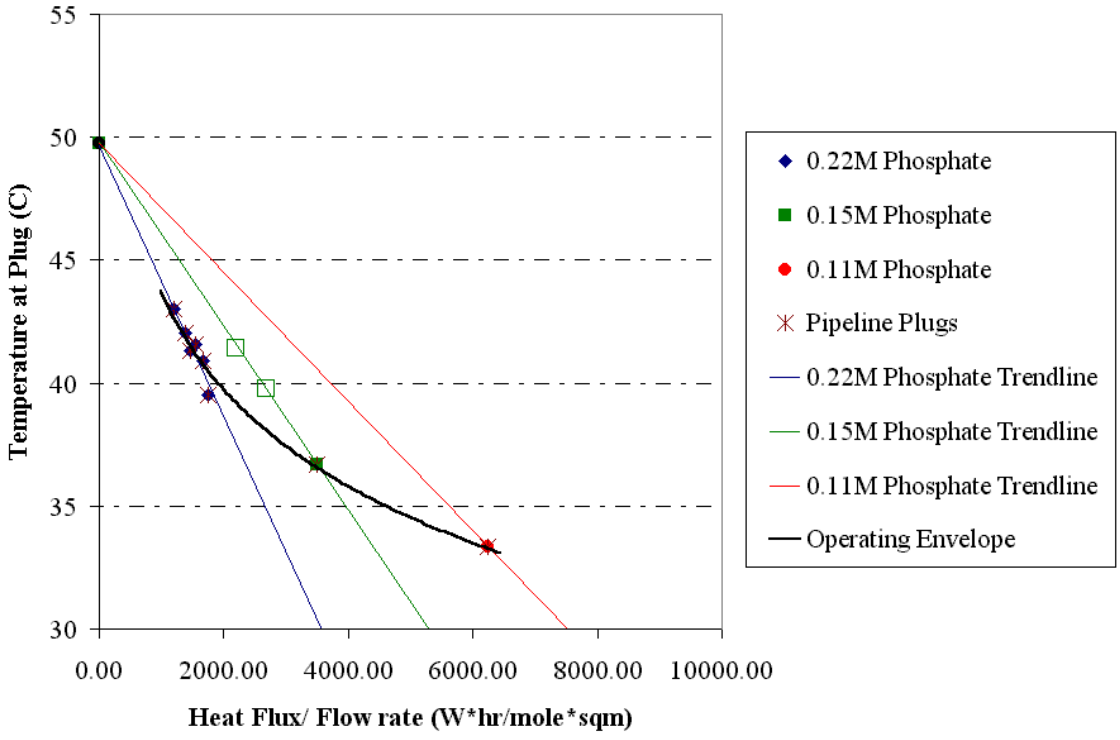

Figure 4.4: Operating envelope for saltwell pumping experiments. Solid symbols indicate experiments that resulted in plugs, while hollow symbols indicate experiments that did not end in plugs. Violet, green and red solid lines are obtained by regression of the data points at each concentration. Operating envelope (black solid line) is obtained by regression of plugging temperatures at different concentrations.

The plot shows that the temperature at plug decreases with decreasing phosphate concentration. At the same flow rate, greater heat flux or cooling rate is required to cause the surrogate to plug at lower phosphate concentrations. There is maximum probability of a plug occurring in the region below the operating envelope, while the chances are minimum for regions above the envelope. The phosphate concentrations in the recipe are plotted against plugging temperatures and are shown in Figure 4.5.

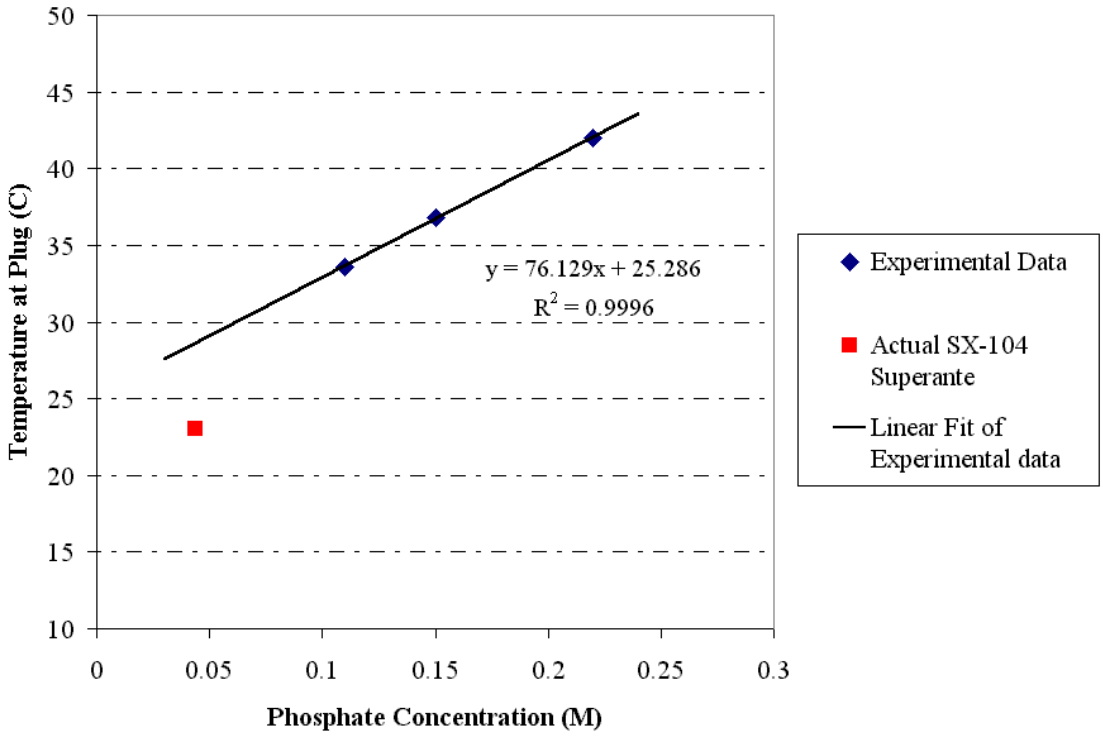

Figure 4.5: Pipeline plugging temperatures at different phosphate concentrations.

The experimental data points are fitted to a straight-line equation. The temperature at plug is best described by the straight-line equation y=m·x+c, where m is the slope of the line, obtained as 76.13^{o}C/M (temperature/ concentration) and c is its intercept, 25.29^{o}C. The data points show good agreement with the straight line fit. The straight line is extrapolated, to compare the experimental results with actual tank sample plugging

temperature obtained by Herting and Steen [6,7]. Regression of experimental data indicates that the tank sample would plug at 28.5^{o}C, while it actually plugged at 23^{o}C. The difference in the actual and regressed plugging temperatures can be mainly attributed to the variation in component concentrations and or temperature dependence of physical properties. The possible presence of additional solids (apart from the plug causing phosphate crystals) might vary the plugging mechanism and thus the plugging temperature. Future efforts are planned to establish these effects.

The saltwell pumping test loop experiments showed that the time to plug increased with increasing flow rate. This cannot be applied to the saltwell pumping at Hanford as the pumping rate is dependent on the rate of seepage of supernate into the central well. By maintaining the supernate at a high temperature or at low phosphate concentration, the plug formation can be prevented. Although the ideal phosphate concentration and temperature of supernate required to prevent plugging can be obtained from the operating region in Figure 4.4, certain operating difficulties persist. These arise due to the variation of phosphate concentration within the tank and lack of thermocouple probes inside the pipes to provide exact temperature measurements.

The average concentration of phosphate in the tank can be obtained. This can be plotted on the operating region plot (Figure 4.4) to obtain an estimate for the temperature at which the supernate should be maintained to prevent plugging. The thermocouple probes on the outside of the pipe can be used to calculate the temperature of supernate flowing inside the pipe, at a given outside ambient temperature. Based on this information, the dilution water temperature or flow rate required to prevent a plug can be determined.

CHAPTER V

CONCLUSION AND FUTURE CONSIDERATIONS

The main focus of the this research is the study of mechanisms underlying pipeline plugging during interim stabilization operations at Hanford by evaluating those parameters affecting plug development and formation. A test loop was developed in the laboratory to perform experiments that simulated actual pipeline plugs. The test loop contained pressure transducers, thermocouple probes and flow meters, which were used to monitor the process flow conditions. The instrumentation readings were monitored by a data acquisition system. An imaging system was used to view the process in detail. Images from the system were processed using imaging software, which helped in the identification of the critical parameters.

A recipe containing $Na_3PO_4 \cdot 0.25NaOH \cdot 12H_2O$ was developed, which was identified as the primary constituent of pipeline plugs at Hanford. The dependence of variables such as surrogate flow rate, cooling water flow rate and phosphate concentration on pipeline plugging were examined. An increase in surrogate flow rate increased the time to plug, which was attributed to the "induction time" and slower cooling of the surrogate. A decrease in the cooling water flow rate increased the time to plug due to the reasons mentioned above. The lowering of phosphate concentrations in the recipe reduced the plugging temperature because of the formation of $Na_3PO_4 \cdot 0.25NaOH \cdot 12H_2O$ crystals at lower temperatures. Plugging experiments were carried out at phosphate concentrations of 0.22M, 0.15M and 0.11M in the recipe, while

the actual Hanford supernate had a $Na_3PO_4 \cdot 0.25NaOH \cdot 12H_2O$ concentration of 0.07M. This enabled the study of pipeline plugs at higher temperatures and phosphate concentrations that could be used during interim stabilization operations.

Image analysis of the experiments showed that the events leading to plug formation. The cooling of the surrogate caused a reduction in its temperature, when single particles started to form in the channel. The particles grew to a critical size and deposited. The increasing number of single particles in the channel caused them to agglomerate and deposit. The single particles and agglomerates formed a bed and moved along with the flow at the bottom of the channel. The moving bed gradually grew and encompassed the entire channel. The frictional effects become predominant at this point and all movement ceased, resulting in a plug. Image analysis indicated that the single particle growth rate did not vary with the surrogate flow rate. The growth rate decreased with phosphate concentration and decreased with cooling water flow rate. The pressure and temperature profiles from the data acquisition system were coupled with the results from image analysis to show the effect of particle, agglomerate and bed formation on the pressure and temperature readings. The maximum size to which a single particle could grow without depositing and the corresponding critical velocity was calculated for experiments at different surrogate flow rates. Models available in the literature were adapted to explain the temperature drop of surrogate when heat exchangers were activated and pressure rise due to the single particles, agglomerates and bed movement.

The research was also directed towards the development of an operating regime, which would minimize the chances of plugging during the unit operations. The results from plugging experiments at different flow rates and surrogate concentrations were

combined to this effect. An operating region, which would not result in plug formation, was identified. The secondary focus of the work is on the unplugging of pipeline plugs. The mechanisms underlying unplugging have been investigated and the effect of pump head and residence time of plug in channel on unplugging rate was studied.

Future efforts should be directed towards extending the results of the present research to other plugging mechanisms, such as those involving entrained solids prior to plug formation. This would enhance the understanding of the formation of pipeline plugs and enable the development of better resources to prevent them from occurring. Focus can also be directed to the development of chemical/physical processes for unplugging by extending the current research. In conclusion, this research presents an understanding of plugging mechanisms underlying pipeline plugs at Hanford and develops an operating region, which would reduce the risk of pipeline plugs and result in significant cost savings.

REFERENCES

1. *2-Year Progress Report to Congress*, 2000, DOE/ORP-2000-27, prepared for Office of River Protection, Richland, Washington.

2. *Tank Farm Equipment Description*, Volume II, Tank Farm Information for TFA Workers.

3. Ross, W.E., Smith, R.D., Freeman, D.V., 1998, *Single-Shell Tank Interim Stabilization Project Plan*, HNF-2358, Rev. 0, prepared by Fluor Daniel Hanford, Inc. for U.S. Department of Energy, Richland, Washington.

4. *Single-Shell Tank Closure Work Plan*, 1996, DOE/RL-89-16, Rev. 1, prepared for U.S. Department of Energy, Richland, Washington.

5. S*ingle-Shell Tank Retrieval Program Mission Analysis Report,* 1998, HNF-2944, Rev. 0, prepared by Fluor Daniel Hanford, Inc. for U.S. Department of Energy, Richland, WA.

6. Herting, D.L., October 1999, *Personal Communication to J.S. Lindner*, Diagnostic Instrumentation and Analysis Laboratory, Mississippi State University, Starkville, MS

7. Steen, F.H., 1999, "*Analysis Results for the Final Report for Tank 241-SX-104*," Memo, WMH-9856353, Numatec Hanford Corporation, Richland, Washington.

8. Reynolds, D.A., May 2000, "*Status of Waste Transfers, Criteria and Plans*," Presented at the Saltcake Dissolution and Feed Stability Workshop, Richland, Washington.

9. Snell, F. D., 1930, "*Trisodium Phosphate-Its Manufacture and Use*," Ind. Eng. Chem., 23, 470-474.

10. Mason, C.W., and Ashcraft, E.B., 1939, "*Trisodium Phosphate-Sodium Fluoride: Phase Studies and Analytical Methods*," Ind. Eng. Chem., 31, 768-774.

11. Ghule, A., Murugan, R. and Chang, H., 2001, "*Thermo-Raman Studies on Dehydration of $Na_3PO_4 \cdot 12H_2O$*," Thermochim. Acta., 371(1-2), 127-135.

12. Bell, R.N., 1949, "*Hydrates of Trisodium Orthophosphate*," Ind. Eng. Chem., 41, 2901-2905.

13. Quimby, O.T., 1947, "*Trisodium Phosphate*", Chem. Rev., 40,141-144.

14. Tillmanns, E., and Baur, W.H., 1970, "*On the Stoichiometry of Trisodium Orthophosphate Dodecahydrate*," Inorganic Chemistry, 9, 1957-1958.

15. Li, H., Hsieh, C.K., and Goswami, D.Y., 1996, "*Conjugate Heat Transfer Analysis of Fluid Flow in a Phase-Change Energy Storage Unit*," Int. J. Num. Meth. Heat Fluid Flow, 6, 77-90.

16. Dancy, E.A., 1984, "*The Behaviour of Saturated Solutions of Trisodium Phosphate Dodecahydrate as Heat Storage Media*," Sol. Energy, 33, 41-48.

17. Ayazi, S.P., 1987, "*Hydraulic transport of particulate solids*," Chem. Eng. Commun, 62, 233-49.

18. Tchobanoglous, G., Burton, F.L., 1991, Wastewater Engineering: Treatment, Disposal and Reuse, 3rd Ed., McGraw-Hill Water Resources and Environmental Engineering Series.

19. McCabe, W. L., Smith, J.C., Harriott, P., 1993, "Unit Operations of Chemical Engineering," 5th ed., Mcgraw Hill Chemical Engineering Series.

20. Bird, R.B., Stewart, W.E., Lightfoot, E.N., 1994, Transport Phenomena, John Wiley & Sons.

21. Wasp, E.J., Kenny, J.P. and Gandhi, R.L., 1977, Solid-Liquid Flow Slurry Pipeline Transportation, Trans. Tech. Publications.

22. Oroskar, A.R., and Turian, R.M., 1980, "*The Critical Velocity in Pipeline Flow of Slurries*," AIChE J., 26, 550-557.

23. Lockhart, R.W., and Martinelli, R.C., 1949, "*Proposed Correlation of Data for Isothermal Two-Phase, Two-Component Flow in Pipes*," Chem. Eng. Progress, 45, 39-48.

24. Mao, F., Desir, F.K. and Ebadian, M.A., 1997, "*Pressure Drop Measurement and Correlation for Three-Phase Flow of Simulated Nuclear Waste in a Horizontal Pipe*," Int. J. Multiphase Flow, 23, 397-402.

25. Wilson, K.C., 1976, "*A Unified Physically-Based Analysis of Solid-Liquid Pipeline Flow*," 4th International Conference on the Hydraulic transport of Solids in Pipes, Hydrotransport4, Alberta, Canada.

26. P.Doron, D. Barnea, 1993, "*A Three-Layer Model for Solid-Liquid Flow in Horizontal Pipes*," Int. J. Multiphase Flow, 19, 1029-1043.

27. Mason, D.J., Levy, A., 2001, "*A Model for Non-Suspension Gas-Solids Flow of Fine Powders in Pipes*," Int. J. Multiphase Flow, 27, 415-435.
28. Seigel, R., 1963, "*Forced Convection in a Channel with Wall Heat Capacity and Wall heating Variable with Axial Position and Time*," Int. J. Heat Mass Transfer, 6, 607-620.

29. Tan, K.S., and Spinner, I.H., 1978, "*Dynamics of a Shell and Tube heat Exchanger with Finite Tube-Wall Heat Capacity and Finite Shell-Side Resistance*," Ind. Eng. Chem. Fundam., 17, 353-358.

30. Sucec, J., 1988, "*Analytical Solution for Unsteady heat Transfer in a Pipe*," Transactions of ASME, Journal of Heat Transfer, 110, 850-854.

31. Schutte, D.J., Rahman, M.M. and Faghiri, A., 1992, "*Transient Conjugate Heat Transfer in a Thick-Walled Pipe with Developing Laminar Flow*," Numerical Heat Transfer, Part A, 21, 163-186.

32. Yan, W.M., Tsay, Y.L., and Lin, T.F., 1989, "*Transient Conjugated Heat Transfer in Laminar Pipe Flows*," Int. J. Heat Mass Transfer, 32, 775-777.

33. Patankar, S.V., 1980, Numerical Heat Transfer and Fluid Flow, Chap. 6, Hemisphere/Mcgraw-Hill, New York.

34. Krishan, B., 1982, "*On Conjugated heat Transfer in Fully Developed Flow*," Int. J. Heat Mass Transfer, 25, 288-289.

35. *Saltwell Pumping from Tank SX-104*, Volume II, Tank Farm Information for TFA Workers.

36. Hunt, R., *Personal Communication to J.S. Lindner*, February 2000, Diagnostic Instrumentation and Analysis Laboratory, Mississippi State University, Starkville, MS.

37. Monts, D.L., Jang, P.R., Su, J.C., McCarthy, M.J., ArunKumar, R., Kirkland, R.L., and Cook, R.L., March 2000, "*Diagnostic Imaging Measurements for Process Optimization of an Industrial Electric Power Generating Facility*", Pittsburgh Conference and Exposition on Analytical Chemistry and Applied Spectroscopy (PittCon 2000) Poster, New Orleans, LA.

38. *Tank Farm Equipment Description*, Volume I, Tank Farm Information for TFA Workers.

39. CRC. 1975, CRC Handbook of Chemistry and Physics, 56th Edition, CRC Press,Inc., Cleveland, Ohio.

40. Perry, R.H., and Chilton, C.H., 1973, Chemical Engineers Handbook, 5th Ed.

McGraw-Hill Book Company, New York, New York.

41. Hodge, B.K., and Taylor, R.P., Analysis and Design of Energy Systems, 3rd Ed. Prentice Hall, Upper Saddle River, New Jersey.

42. Incropera, F.P. and Dewitt, D.P., Fundamentals of Heat and Mass Transfer, 3rd Ed. John Wiley, New York, New York.

43. Kays, W.M., and Crawford,M. 1980, Convective Heat and Mass Transfer, 2nd Ed. McGraw-Hill Book Company, New York, New York.

44. Benedict, R.P.1980, Fundamentals of Pipe Flow, John Wiley, New York, New York.

APPENDIX A

DILUTION OF RECIPE FOR IC ANALYSIS

Appendix A.1: Notes

The anionic concentrations obtained for the saltwell surrogate from ESP were compared to those obtained from the IC. The IC was capable of analyzing $(NO_3)^-$ and $(PO_4)^{3-}$. ESP simulations (Table 3.3) predicted a liquid phase $(NO_3)^-$ concentration in the range of 228,000-223,000ppm and $(PO_4)^{3-}$ concentration in the range of 2800-3000ppm. The surrogate samples were diluted below 100ppm for IC analysis. The liquid phase concentration of $(NO_3)^-$ was about 100 times that of the $(PO_4)^{3-}$ concentrations, so the surrogate samples were initially diluted 100 times for $(PO_4)^{3-}$ and then further diluted 100 times (total 10000 times) for $(NO_3)^-$ sampling. The dilutions were based on mass. The diluted solutions for $(NO_3)^-$ and $(PO_4)^{3-}$ were then analyzed in the IC.

APPENDIX B

EQUIPMENT, INSTRUMENTATION AND FITTINGS USED IN SALTWELL TEST LOOP

Appendix B.1 Equipment and Instrumentation Used

Equipment/ Instrumentation	Description	Number
Tank1-3	Stainless steel tanks with capacity of 7 gal	3
Pump1-2	Magnetic drive pump with 1/15 hp rating	2
Heater1-3	Screw plug immersion heater to maintain surrogate temperature in tank aroun 50^{o}C	3
Hex1-4	Heat exchangers used to reduce surrogate temperature	4
RMS	Rotameter for use with surrogate. Range 0-20gph	1
RMW	Rotameter for use with water. Range 0-5gpm	1
RM1-4	Rotameters for control of cooling water	4
RM3a-4a	Rotameters for control of cooling water	2
P0-3	Pressure Transducers used to monitor pressure in line	3
T0, T6, Tw	PFA coated thermocouple probes used to monitor temperature of surrogate in Tanks1-3	3
T1-5	PFA coated thermocouple probes used to monitor temperature of surrogate in test loop	5
Tw,Tw0-4	Thermocouple probes used to monitor cooling water inlet and outlet temperature in test loop	6

Appendix B.2: Various fittings and Corresponding Friction Factors Used

Fitting Used	Number	Friction Factor
Union	2	0.04
90^{o} Standard elbow	3	0.75
90^{o} Long radius elbow	3	0.45
Coupling	15	0.04
Tee	14	0.4
Ball valve	6	$3f_T$

f_T is defined as, $f_T = \dfrac{0.3086}{\log\left[\left(\dfrac{\varepsilon}{3.7 \cdot D_{ex}}\right)^{1.11}\right]^2}$ (B.1)

where ε(0.0015ft) is the roughness of the pipe, K_{ent}(0.78) is the entrance loss and K_{exit}(1) is the exit loss.Based on the $K^{'}$ values for individual fittings the total $K^{'}$ is defined as:

$$K^{'} = 2 \cdot K_{union} + 3 \cdot K_{stdelbow} + 3 \cdot K_{longelbow} + 15 \cdot K_{coupling} + 14 \cdot K_{tee} + 6 \cdot K_{valve} + K_{ent} + K_{exit} \quad \text{(B.2)}$$

APPENDIX C

ASSEMBLY OF THE SALTWELL PUMPING TEST LOOP

Appendix C.1: Notes

The surrogate was stored in Tank1 and maintained at a temperature around 50^{o}C using Heater1. Tank1 had an elongated nipple at the bottom that was fitted to an SS 304 ball valve, used to turn off the surrogate supply to the test loop. The ball valve (Valve1) was connected to a ½" SS 316 pipe, leading to Pump1, using a union coupling. The union coupling enabled the separation of the surrogate tank from the test loop for cleaning. Tank3 held water at a predetermined temperature for preheating, unplugging and cleaning. Tank3 had an elongated nipple that lead to a tee joint. One section from the tee joint was connected to a ½" copper pipe, through a ball valve (Valve3), that lead to Pump2. This section was used to flush the recycle line after each use. The other section of the tee joint was connected to a ½"copper pipe which lead to the water rotameter (RMW). The ½" copper pipe from outlet of RMW was connected to a ball valve (Valve2). The other end of Valve2 was connected to a ½" SS 316 pipe that was welded with the pipe from Tank1. This pipe was connected to the Pump1 through a union coupling. Pump1 was connected to a tee joint with a ½" SS 316 pipe. One section from the tee joint lead to surrogate rotameter (RMS) while the other was connected to a 1/8" SS 316 pipe that lead back to the Tank1 through a ball valve (Valve4). This arrangement was made, by opening Valve4, to constantly stir the contents of Tank1 when surrogate was being pumped and to maintain the entire surrogate at the same temperature.

The surrogate rotameter was connected to the heat exchanger, Hex1, through fittings (Table B.2). The ball valves were used to isolate individual sections in the event of a plug. The tee joints for thermocouples were fitted with ¼" caps, with 3/16" bore

through which thermocouples could be screwed into the line. The pressure transducers could be screwed directly into the tee joints. The ball valves were used to isolate sections of the test loop in the event of a plug. Initially, the arrangement of fittings was repeated for all the 4 heat exchangers (Hex1-4). Clear tubing was connected downstream of Hex2. The end of the clear tubing was fitted with tee joints for a pressure transducer and a thermocouple probe followed by a 3-way valve (Valve5). Cooling was not applied to the clear tubing. Sample ports were used in between heat exchangers to clear the line upstream of the plug and to collect surrogate test samples.

One section from Valve5 was directed to Tank2 while the other section was directed either to drain or Tank3, based on need, using flexible tubing. If the line was being unplugged then the section was directed to drain; if the line was being preheated it was directed to Tank3.

Preheating was a procedure followed before each of the saltwell pumping experiments in which water heated to around 50^{o}C in Tank3 was pumped through the salwell loop and returned back to Tank3 through flexible tubing connected to Valve5. The purpose of preheating was to maintain the saltwell test loop at or near a temperature of 50^{o}C before the surrogate was pumped, so that a temperature drop did not occur prior to the heat exchangers. The surrogate directed to Tank2 was maintained around 50^{o}C and was recycled back to Tank1 using Pump2. The Pump2 was connected to Tank1 by a ½" SS 316 pipe with the provision for draining the line using a tee joint fitted to a valve. The section from the tee joint of Tank3 discussed above was used to flush the line after each recycling operation. This was done to clear the line of any plug that might form in the recycle line from the surrogate left behind after recycling.

Cooling water for the heat exchangers was supplied from the tap. PVC tubing was used to connect the hose to the copper tubing, supplying the cooling water to heat exchangers. The rotameters (RM1-4 and RM3a, 4a) were used to regulate water supply. Thermocouples fitted at the inlet and outlet of each heat exchanger were used to monitor the cooling water temperatures. The water from each of the heat exchangers flowed back via copper tubes to a PVC tube that was sent to drain.

APPENDIX D

SAMPLE CALCULATIONS FOR TEMPERATURE DROP AND PRESSURE RISE MODELS

Appendix D.1: Heat Transfer Model

The temperature drop in the surrogate due to the use of heat exchangers is compared to a theoretical model developed by Krishan [34]. The theory and procedure to obtain solutions are discussed in Chapter 1.2.4. The Mathcad program used is given below:

Heat Transfer Model

$b_1 := 0.5 \cdot in$ ..... Outer dia of pipe

$a_1 := 0.25 \cdot in$ ..... Inner dia of pipe

$b := \frac{b_1}{a_1}$ ..... Ratio of inner and outer dia

$V := 16.2 \cdot \frac{cm}{sec}$ ..... Flow velocity

$C_{pl} := 3020 \cdot \frac{J}{kg \cdot K}$ ..... Specific heat of surrogate

$\Delta T := 7 \cdot K$ ..... Total temperature drop of surrogate

$k_1 := 0.615 \cdot \frac{W}{m \cdot K}$ ..... Thermal conductivity of surrogate

$\mu_1 := 4 \cdot cp$ ..... Viscosity of surrogate

$\rho_1 := 1390 \cdot \frac{kg}{m^3}$ ..... Density of surrogate

$Pr_1 := C_{pl} \cdot \frac{\mu_1}{k_1}$ ..... Prandtl number of surrogate

$E_1 := \frac{V^2}{C_{pl} \cdot \Delta T}$ ..... Eckert number of surrogate

$C_1 := 16 \cdot E_1 \cdot Pr_1$

$k_s := 15 \cdot \frac{W}{m \cdot K}$ ..... Thermal conductivity (TC) of steel

$K_r := \frac{k_s}{k_l}$ ..... Ratio of TC of steel and surrogate

$C_{ps} := 500 \cdot \frac{J}{kg \cdot K}$ ..... Specific heat of steel

$\rho_s := 8027 \cdot \frac{kg}{m^3}$ ..... Density of steel

$\alpha_s := \frac{k_s}{\rho_s \cdot C_{ps}}$ ..... Thermal diffusivity of steel

$\alpha_l := \frac{k_l}{\rho_l \cdot C_{pl}}$ ..... Thermal diffusivity of surrogate

$\alpha := \frac{\alpha_s}{\alpha_l}$ ..... Ratio of thermal diffusivites

$Z := \left(\frac{\alpha}{K_r}\right)^{0.5}$ ..... Conjugation parameter

$Z_1 := 1 + Z$

$Z_2 := \frac{(1 - Z)}{(1 + Z)}$

$t := 600 \cdot sec$ ..... Time elapsed

$r := 1$ ..... Dimensionless dia

$\tau := \alpha_l \cdot \frac{t}{a_1^2}$ ..... Fourier number

$u := 0$

$b_{nr}(n) := (2 \cdot n + 1) \cdot (b - 1) - (\alpha \cdot (r - 1))^{0.5}$

$b_{nru}(n) := 2 \cdot (n + u) \cdot (b - 1) - (\alpha \cdot (r - 1))^{0.5}$

$A_1(n) := (0 + i) \cdot erfc\left[\frac{b_{nr}(n)}{2 \cdot (\alpha \cdot \tau)^{0.5}}\right]$

To ..... Initial temperature

T ..... Final temperature

$\theta = \frac{(T_0 - T)}{T_0}$ ..... Dimensionless temperature

The temperature distibution of surrogate is obtained for constant heat flux by the formula:

$$\theta_1 = \left[\sum_{n=0}^{\infty}\left[\frac{(Z_2)^n}{Z_1 \cdot r^{0.5}}\right]\cdot\left[\begin{array}{l} 2\cdot S_1\cdot\left[b\cdot\alpha\cdot(4\cdot\tau)^{0.5}\cdot A_1(n)\right]^{0.5} - 2\cdot C_1\cdot Z\cdot(4\cdot\tau)^{\frac{3}{2}}\cdot A(n,3) \ldots \\ + \left(C_1\cdot 4\cdot\tau\right)\cdot(A(n,2) + 16\cdot\tau\cdot A(n,4)) \end{array}\right]\right] + \blacksquare \ldots$$
$$+ C_1\cdot r^2\cdot\tau + 2\cdot C_1\cdot\tau^2$$

$$\text{sum}(i) := \left|\begin{array}{l} \theta_1 \leftarrow 0 \\ \text{for } n \in 0..i \\ \quad \theta_1 \leftarrow \theta_1 + \left[\frac{(Z_2)^n}{Z_1\cdot r^{0.5}}\cdot\left[\begin{array}{l} 2\cdot S_1\cdot\left[b\cdot\alpha\cdot(4\cdot\tau)^{0.5}\cdot A_1(n)\right]^{0.5} \ldots \\ + 2\cdot\left(-C_1\right)\cdot Z\cdot(4\cdot\tau)^{\frac{3}{2}}\cdot A(n,3) \ldots \\ + C_1\cdot 4\cdot\tau\cdot(A(n,2) + 16\cdot\tau\cdot A(n,4)) \end{array}\right]\right] \end{array}\right.$$

$\text{sum}(1000) = 0.081 + 0.035i$

$p := \text{Re}(\text{sum}(10000)) + \left(C_1\cdot r^2\cdot\tau + 2\cdot C_1\cdot\tau^2\right)$

$T := 46.216\cdot(1 - p)$

$T = 42.264$

Appendix D.2: Pressure Rise Model

The pressure rise in the channel due to the formation of particles and bed growth is compared to a theoretical model developed by Wilson [27]. The model was developed assuming a two-layer flow (liquid on top and solids at bottom) where the fraction of

solids increases from 0 to 1 resulting in a plug. The fraction of solids can be directly obtained from the height of solids or bed width in the line. The theoretical model is programmed in Mathcad to obtain the solutions.

Pressure Rise Model

$h := 0.040 \cdot in$ ..... Height of bed in the pipe

$D := 0.25 \cdot in$ ..... Pipe internal diameter

$D_p := 0.4 \cdot mm$ ..... Particle diameter

$x := 6 \cdot ft$ ..... Length of pipe section

$V_l := 7.95 \cdot \frac{cm}{sec}$ ..... Stream velocity

$\rho_l := 1390 \cdot \frac{kg}{m^3}$ ..... Surrogate (stream) density

$\mu_l := 4 \cdot cp$ ..... Viscosity of surrogate

$V_s := 7.72 \cdot \frac{cm}{sec}$ Bed Velocity

$\rho_s := 1620 \cdot \frac{kg}{m^3}$ ..... B ed (solid) density

$x_s := \left(\frac{h}{D}\right)$ ..... Bed fraction

$x_l := \left(1 - x_s\right)$ ..... Stream fraction

$S_s := \left(D \cdot acos\left(1 - 2 \cdot \frac{h}{D}\right)\right)$ ..... Solid fraction wetted perimeter

$S_l := D \cdot \left(\pi - acos\left(1 - 2 \cdot \frac{h}{D}\right)\right)$ ..... Liquid fraction wetted perimenter

$A_s := \frac{\left[D \cdot S_s - 2 \cdot D^2 \cdot \left[\left(\frac{h}{D}\right) - \left(\frac{h}{D}\right)^2\right]^{0.5} \cdot \left(1 - 2 \cdot \frac{h}{D}\right)\right]}{4}$ ..... Solid fraction cross-sectional area

$$S_i := 2 \cdot D \cdot \left[\left(\frac{h}{D} \right) - \left(\frac{h}{D} \right)^2 \right]^{0.5}$$ ..... Dimensionless wetted perimeter

$$S_{ml} = \frac{\left(x_l \cdot \rho_l \cdot V_l \cdot S_i \cdot \frac{dh}{dx} \right)}{2}$$ ..... Mass transfer in liquid phase

$$S_{ms} = \frac{\left(x_s \cdot \rho_s \cdot V_s \cdot S_i \cdot \frac{dh}{dx} \right)}{2}$$ ..... Mass transfer in solid phase

$$Re := (D - h) \cdot V_l \cdot \frac{\rho_l}{\mu_l}$$ ..... Reynolds number (stream)

$$f_l := \frac{64}{Re}$$ ..... Friciton factor

$$\tau_l := \frac{\left(f_l \cdot \rho_l \cdot V_l^2 \right)}{2}$$ ..... Shear between wall and liquid

$$C_d := \frac{g \cdot \left(\rho_s - \rho_l \right) \cdot D_p}{\rho_s \cdot V_s^2}$$ ..... Drag coefficient

$$F_d := \frac{\left(3 \cdot x_s \cdot A_s \right)}{4 \cdot D_p} \cdot C_d \cdot \rho_l \cdot \left(V_l - V_s \right) \cdot \left| V_l - V_s \right|$$ ..... Drag force

The pressure drop in the pipe is thus given by:

$$\Delta P := - \left(\rho_l \cdot x_l \cdot A_l \cdot V_l^2 - x_l \cdot \rho_l \cdot V_l^2 \cdot S_i \cdot \frac{h}{2} - \tau_l \cdot x_l \cdot S_l \cdot x - F_d \cdot x \right) \cdot \frac{1}{x_l \cdot A_l}$$

$\Delta P = 0.261 \cdot psi$

$\Delta P_{act} := \Delta P + 0.6258 \cdot psi$ (where ΔP_{act}

observed using imaging system)

$\Delta P_{act} = 0.887 \cdot psi$

APPENDIX E

MOVIE CLIPS OF PLLUGGING AND UNPLUGGING PROCESSES

Appendix E.1: Movie clip of plugging process at surrogate flow rate of 3.5 gph.
Place mouse on image and right click to play movie.

Appendix E.2: Movie clip of unplugging process.
Place mouse on image and right click to play movie.